HEME CATABOLISM:
SIGNALING MASQUERADING AS METABOLISM

by
Chirag Vasavda

A dissertation submitted to Johns Hopkins University in conformity with the requirements for the degree of Doctor of Philosophy

Baltimore, Maryland
July 2019

ABSTRACT

Metabolism and signaling were classically viewed as unrelated cellular processes. Signaling was considered to be a dynamic process that involved transcription, translation, and protein-protein interactions, whereas metabolism was categorized as more passive processes involved in maintaining and sustaining the cell. Now, it is widely accepted that signal transduction often involves reprogramming metabolism. For example, insulin shifts the metabolism of glucose, glycogen, and triglycerides. Emerging evidence suggests that a reciprocal relationship between metabolism and signaling exists as well, where metabolites themselves mediate signaling. Diverse modifications such as glycosylation, succinylation, acetylation, and nitrosylation are all directly derived from metabolites. In this body of work, we report that three heme metabolites – carbon monoxide (CO), biliverdin, and bilirubin – play critical roles at the intersection of metabolism and signaling. First, we report that O_2-sensing by the carotid body is mediated by CO. O_2 is sensed by the enzyme heme oxygenase (HO) as a substrate, which produces CO as a product of heme oxidation. CO in turn stimulates protein kinase G to inhibit cystathionine-γ-lyase (CSE), an enzyme that produces the gaseous molecule hydrogen sulfide (H_2S). Less O_2 is available in hypoxia to produce CO, leading to increased CSE activity. CSE produces more H_2S as a result, which itself stimulates carotid body activity and breathing. Secondly, we report that bilirubin is a physiologic

antioxidant with distinct redox activity among endogenous small molecules. Whereas major antioxidants such as glutathione and cysteine exhibit little to no reactivity towards $O_2^{\bullet-}$, bilirubin readily scavenges $O_2^{\bullet-}$. We find that bilirubin's redox activity is particularly important in the brain, where it prevents excitotoxicity and neuronal death by scavenging $O_2^{\bullet-}$ during NMDA neurotransmission. Lastly, we report that pathophysiologic levels of bilirubin excite peripheral itch sensory neurons and elicit pruritus (itch) through Mrgprs, a family of G-protein coupled receptors expressed in primary sensory neurons. Various pathologic conditions result in jaundice, a yellowing of the skin due to a buildup of bilirubin. Patients with jaundice commonly report experiencing an intense non-histaminergic itch. Despite this association, the pruritogenic capacity of bilirubin itself has not been explored, and no bilirubin receptor has been identified.

Thesis Advisor:

Dr. Solomon H. Snyder, MD (Designated reader)

Thesis Committee Members:

Dr. Xinzhong Dong, PhD (Designated reader)

Dr. Seth Margolis

Dr. Michael Caterina, MD, PhD

PREFACE

Acknowledgements

When I reflect upon my years in the lab at Duke, UChicago, and Hopkins, I remember much more than data and experiments. My mind is flooded with memories of individuals working beside me, many of whom supported, taught, and guided me. One of them once told me that science is one of the most important group projects in the history of humankind. Because of them, I have had the privilege to make my own contributions to science. I hope to continue to contribute in the years to come, now a little more competently than before.

I am deeply grateful for the privilege to have studied under Dr. Solomon H. Snyder. I first met Sol when he interviewed me for the Hopkins MSTP back in 2013. Most of my Hopkins interviews were with similarly passionate individuals, and their collective energy is what drew me to Hopkins. But I immediately appreciated Sol's neuro-centric, stubbornly molecular approach to science. He also asked me very unusual questions, ones that probed at first principles from an orthogonal angle than others would. Soon after joining Sol's lab in 2014, I learned that my interview was a window into what underlies his outsized number of contributions to science. He challenges us to be methodical and clear, yet still creative and bold. From that interview to this day, Sol inspires me to be a better scientist and thinker, and I will forever be thankful to be a Snyder baby.

I am also thankful to my friend Jimmy Meixiong. Making a discovery is fun, but it is even more rewarding when it is alongside a friend. I remember the day Jimmy and I discovered that bilirubin activated MRGPRX4 very well, as I injured my hand after we jumped on each other in excitement. I value Jimmy not just for his friendship, but also for helping me to grow as a scientist through our projects together.

I could not have completed my PhD thesis without the generosity and support from members of the Snyder laboratory. From my earliest days, Dr. Bindu D. Paul served as another mentor, teaching me essential techniques and guiding me through the scientific process. I thank Adele Snowman for all the cloning, coffees, and workouts; Lynda Hester for all the beautiful neuronal primaries, memes, and emails; Roxanne Barrow for all the cloning and the crosswords; Lauren Albacarys for all the genotyping, behavior, and delicious taste in lunch food; and Ginny Miller for the liters of LB and puppy parenting help.

I also had the greatest pleasure to mentor two bright undergraduate students during my time in graduate school, Ruchita Kothari and Cristina Ricco. I am so proud and excited to see them mature into scientists and physicians, and am incredibly thankful for their friendship, patience, and laughter over the years.

I would also like to thank my thesis committee members, Dr. Xinzhong Dong, Dr. Seth Margolis, and Dr. Mike Caterina. Whether in

passing in the hallways or during formal meetings, they each offered unique insight that advanced both the work at hand and my scientific growth. I am especially thankful to Dr. Xinzhong Dong for serving as another scientific mentor and for his generous support in my collaborations with Jimmy.

I am also eternally grateful to Dr. Vann Bennett, Dr. Paul Jenkins, and Dr. Nanduri Prabhakar for taking me under the wings before my time at Hopkins. Without their mentorship, I would have never had a scientific foundation upon which to build.

I would like to thank my friends and family outside of the lab, whom I deeply appreciate for supporting me unconditionally: Samir Vasavda, Nealay Vasavda, Sneha Vasavda, Bina Trivedi, Jeffrey Tsui, Daniel Zhang, Brian Khoe, Ryan Dhindsa, Kara Li, Victor Shih, Karole D'Orazio, Joyce Lee, Kenneth Ho, and Dr. Susanna Chan.

Lastly, I want to thank my best friend and partner, Byron Ho. Whether Byron was in Chicago, Boston, or Baltimore, he somehow found a way to ground me, support me, and elevate me. Byron has accomplished so much over the years, and through his successes has taught the value of diligence, patience, and kindness. I thank him for believing in me and for pushing me to pursue what I love. Of all of my discoveries, he will always be the most important.

Funding

Thank you to the many sponsors and institutes who provided funding for this work: National Institutes of Health Medical Scientist Training Program Award T32 GM007309, National Institutes of Mental Health Grant MH18501, and the Johns Hopkins Neurosurgery Pain Research Institute Fellowship. Portions of this thesis have been published elsewhere and thus includes contributions from my mentor, Dr. Solomon H. Snyder.

TABLE OF CONTENTS

LIST OF TABLES

LIST OF FIGURES

Protein kinase G–regulated production of H_2S governs oxygen sensing

Summary

Reflexes initiated by the carotid body, the principal O_2-sensing organ, are critical for maintaining cardiorespiratory homeostasis during hypoxia. O_2 sensing by the carotid body requires carbon monoxide (CO) generation by heme oxygenase-2 (HO-2) and hydrogen sulfide (H_2S) synthesis by cystathionine-γ-lyase (CSE). We report that O_2 stimulated the generation of CO, but not that of H_2S, and required two cysteine residues in the heme regulatory motif (Cys^{265} and Cys^{282}) of HO-2. CO stimulated protein kinase G (PKG)–dependent phosphorylation of Ser^{377} of CSE, inhibiting the production of H_2S. Hypoxia decreased the inhibition of CSE by reducing CO generation resulting in increased H_2S, which stimulated carotid body neural activity. In carotid bodies from mice lacking HO-2, compensatory increased abundance of nNOS (neuronal nitric oxide synthase) mediated O_2 sensing through PKG-dependent regulation of H_2S by nitric oxide. These results provide a mechanism for how three gases work in concert in the carotid body to regulate breathing.

Introduction

Cellular communication is mediated through diverse signaling molecules, including proteins, lipids, amino acids, and gases. Gaseous messengers are distinctive among signaling molecules in that they cannot be stored in vesicles. This suggests that gaseous messenger signaling depends on tightly regulated in situ enzymatic synthesis instead of exocytotic machinery. Despite a growing recognition of the widespread importance of gaseous messengers in various biological processes (Mustafa et al., 2009), little is known about their regulation under physiological conditions.

The gaseous messenger carbon monoxide (CO) is important for oxygen (O_2) sensing (Morikawa et al., 2012; Peng et al., 2014; Prabhakar et al., 1995). In the carotid body, changes in blood O_2 concentrations are transduced into changes in CO production. CO signaling during normoxia inhibits the carotid body sensory nerve activity, whereas decreased CO generation during hypoxia increases the carotid body neural output (Peng et al., 2014; Prabhakar et al., 1995). CO acts similarly in the brain to alter cerebral blood flow (Morikawa et al., 2012). High CO concentrations during normoxia elicit vasoconstriction, whereas decreased CO signaling during hypoxia results in vasodilation. CO synthesis in the carotid body (Peng et al., 2014; Prabhakar et al., 1995) and in the brain (Morikawa et al., 2012) is catalyzed by the constitutively expressed enzyme heme oxygenase-2 (HO-2) (Maines, 2004). It is unclear how changes in O_2 concentrations affect CO synthesis by HO-2.

Whereas CO generation is sensitive to changes in O_2, CO by itself does not trigger responses to hypoxia. Instead, CO affects the generation of another gaseous messenger, hydrogen sulfide (H_2S) (Peng et al., 2014; 2010; Prabhakar et al., 1995; Shintani et al., 2009). H_2S mediates increased carotid body sensory nerve activity (Peng et al., 2010; Prabhakar et al., 1995) and cerebral vasodilation (Morikawa et al., 2012) during hypoxia. Emerging evidence suggests that CO suppresses H_2S signaling by inhibiting the H_2S-synthesizing enzymes cystathionine-γ-lyase (CSE) (Peng et al., 2010) and cystathionine β-synthase (CBS) (Peng et al., 2014; Shintani et al., 2009; Taoka and Banerjee, 2001; Taoka et al., 1999). CSE is the predominant source of H_2S in peripheral tissues such as the carotid body (Makarenko et al., 2012; Peng et al., 2010), whereas CBS is responsible for most of the H_2S production in the brain (Paul and Snyder, 2014; Yang et al., 2008). It is believed that CO directly inhibits CBS by binding to its heme moiety (Shintani et al., 2009; Taoka and Banerjee, 2001; Taoka et al., 1999). Unlike CBS, however, CSE is not a heme-containing protein, indicating that CO inhibits CSE by an alternative and unknown mechanism.

O_2 sensing by the carotid body is critical for regulation of vital functions including breathing, heart rate, and blood pressure under hypoxic conditions (Kumar and Prabhakar, 2011). Given the critical roles of CO and H_2S signaling for sensory function of the carotid body (Peng et al., 2010; Prabhakar et al., 1995), we sought to determine how changes in O_2 affect CO and H_2S generation by carotid body chemoreceptor cells. The limited availability of carotid body tissue (wet weight of the mouse carotid body is ~25 μg) necessitated first studying the

effects of O_2 on CO and H_2S generation in human embryonic kidney (HEK) 293 cells heterologously expressing HO-2 and CSE. The mechanisms identified in vitro were then validated in mouse carotid bodies.

Results

Cys^{265} and Cys^{282} are critical for O_2-sensitive CO generation by HO-2

We first examined the effect of changes in the partial pressure of O_2 (PO_2) on CO generation in HEK-293 cells heterologously expressing HO-2. Cells expressing HO-2 generated more CO under normoxia (PO_2 = 142 ± 3 mmHg) than did empty vector–transfected cells. Reducing the PO_2 from ~142 to ~90 mmHg had no significant effect, whereas further reductions in PO_2 resulted in a progressive decrease in CO generation in a stimulus-dependent manner as compared with normoxia (**Fig. 1a**). These findings demonstrated that CO generation by HO-2 was inherently responsive to changes in PO_2.

We next sought to delineate the mechanism underlying the inherent O_2 sensitivity of HO-2. HO-2 has three cysteine residues (Cys^{127}, Cys^{265}, and Cys^{282}; numbering of amino acid residues corresponds to the human protein unless otherwise stated) in the heme regulatory motif (**Fig. 1b**) (McCoubrey, 1997). We investigated whether these cysteine residues are required for the sensitivity of HO-2 to O_2. Substituting alanine for either Cys^{265} or Cys^{282} reduced the O_2 sensitivity of HO-2, whereas mutation of both Cys^{265} and Cys^{282} eliminated modulation of CO generation by hypoxia (PO_2 = 36 ± 4

mmHg; **Fig. 1b**). In contrast, substitution of alanine for Cys^{127} had no effect on CO production during hypoxia (**Fig. 1b**).

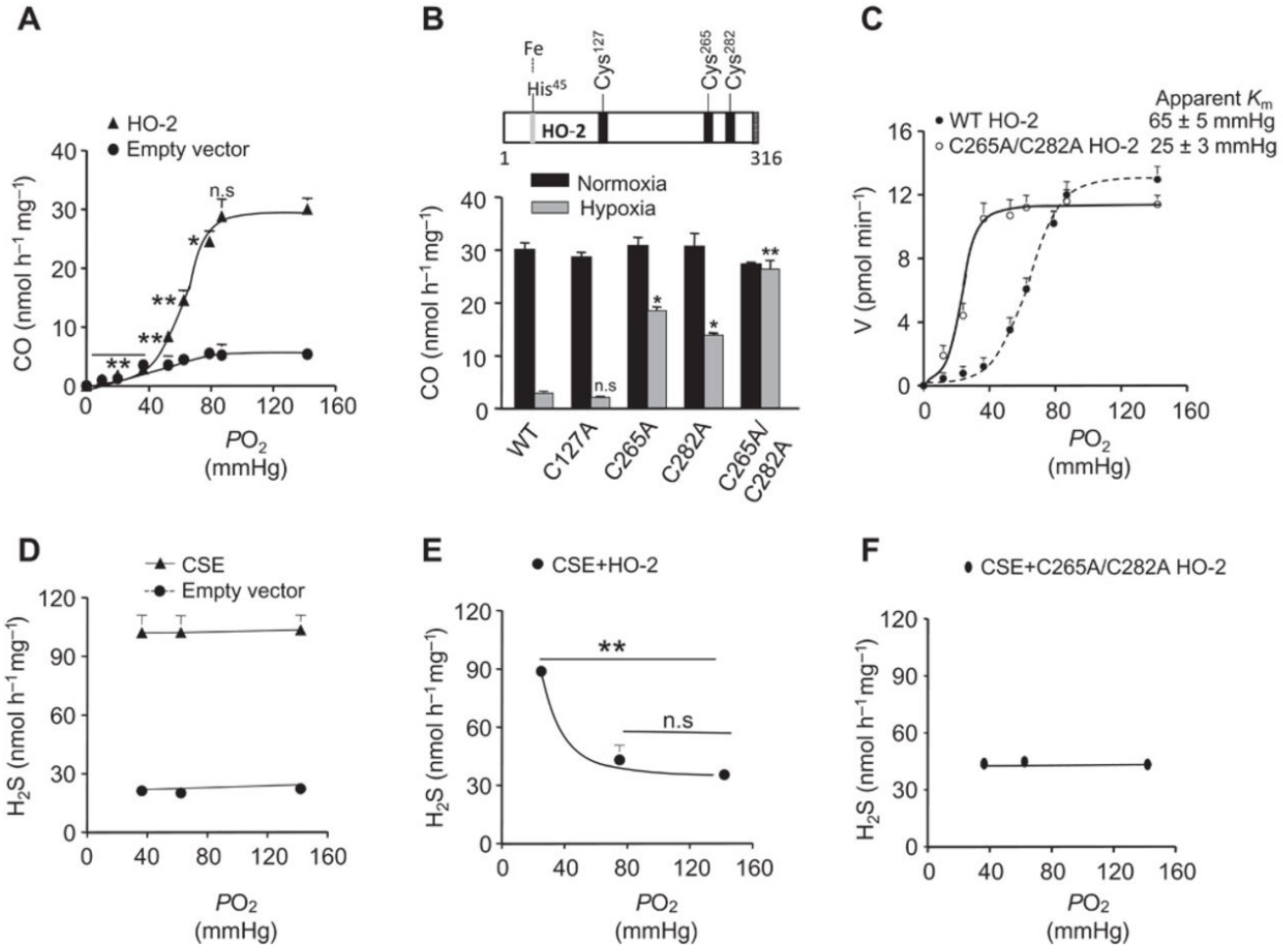

Figure 1. Effect of O_2 on CO and H_2S generation in HEK-293 cells expressing HO-2 and CSE alone or together.

a, CO generation as a function of PO_2 in the medium in cells transfected with the empty vector and HO-2 vector. **b**, Effect of mutating cysteine residues in HO-2 on CO generation. Top: Schematic representation of cysteine residues in the N-terminal and heme regulatory motif of HO-2. Bottom: CO production in cells expressing either wild-type (WT) or mutant (C127A, C265A, C282A, or C265A/C282A) HO-2 in response to normoxia and hypoxia. **c**, Rate of CO generation as a function of PO_2 in WT and mutant HO-2 (C265A/C282A)–expressing cells. Apparent K_m values are derived by iterative curve fitting. **d**-**f**, H_2S generation as a function of PO_2 in cells transfected with the empty vector or CSE vector (D) or vectors encoding CSE and HO-2 (*e*) or CSE and mutant HO-2 (C265A/C282A) (*f*). The graphs in (*a*-*f*) represent means ± SEM (n = 3 to 5 independent experiments). *P < 0.05; **P < 0.01; n.s., not significant (P > 0.05).

We then investigated whether changes in O_2 affinity accounted for the loss of O_2-sensitive CO generation in cells expressing double mutant (C265A/C282A) HO-2. We found that the apparent Michaelis constant (K_m) of wild-type HO-2 for O_2 was 65 ± 5 mmHg (~88 μM), a value close to that reported previously (Migita et al., 1998). In contrast, the K_m of HO-$2^{C265A/C282A}$ was 25 ± 3 mmHg (~34 μM; **Fig. 1c**). These findings suggest that Cys^{265} and Cys^{282} confer low O_2 affinity for HO-2, thereby rendering CO generation sensitive to changes in PO_2.

O_2-dependent HO-2 activity inhibits H_2S generation by CSE

In contrast to the intrinsic O_2 sensitivity of CO generation by HO-2, H_2S generation in CSE-expressing HEK-293 cells was unaffected by changes in PO_2 (**Fig. 1d**). To reconcile the observations that CSE is not directly sensitive to O_2, but H_2S generation from CSE increases during hypoxia in the carotid body (Peng et al., 2010), we hypothesized that CSE was regulated by O_2-sensitive CO generation. Whereas cells expressing only CSE displayed steady H_2S generation regardless of changes in PO_2, cells co-expressing HO-2 and CSE exhibited decreased H_2S concentrations during normoxia and increased concentrations during hypoxia (**Fig. 1e**), recapitulating the O_2-dependent H_2S generation in the carotid body (Peng et al., 2010). However, H_2S concentrations remained unchanged during hypoxia when CSE was co-expressed with the O_2-insensitive mutant HO-$2^{C265A/C282A}$ (**Fig. 1f**). These results demonstrate that CO is an inhibitor of CSE and that O_2-dependent CO generation contributes to increased H_2S generation by CSE in hypoxic cells.

CO inhibits CSE through cyclic guanosine monophosphate

To delineate the mechanism by which CO inhibits CSE, we first considered whether CO inhibits calmodulin, a calcium-dependent activator of CSE (Paul and Snyder, 2014). CO might inhibit CSE activity by reducing the pool of intracellular calcium available to stimulate calmodulin. However, the intracellular Ca^{2+}concentrations ($[Ca^{2+}]_i$) were similar in cells that co-expressed HO-2 and CSE and in cells that only expressed CSE (**Fig. 2-b**). The calmodulin inhibitor W7 [*N*-(6-aminohexyl)-5-chloro-1-naphthalenesulfonamide hydrochloride] did not affect H_2S generation (**Fig. 2c**), arguing against a mechanism in which CO inhibits H_2S by regulating calmodulin activity.

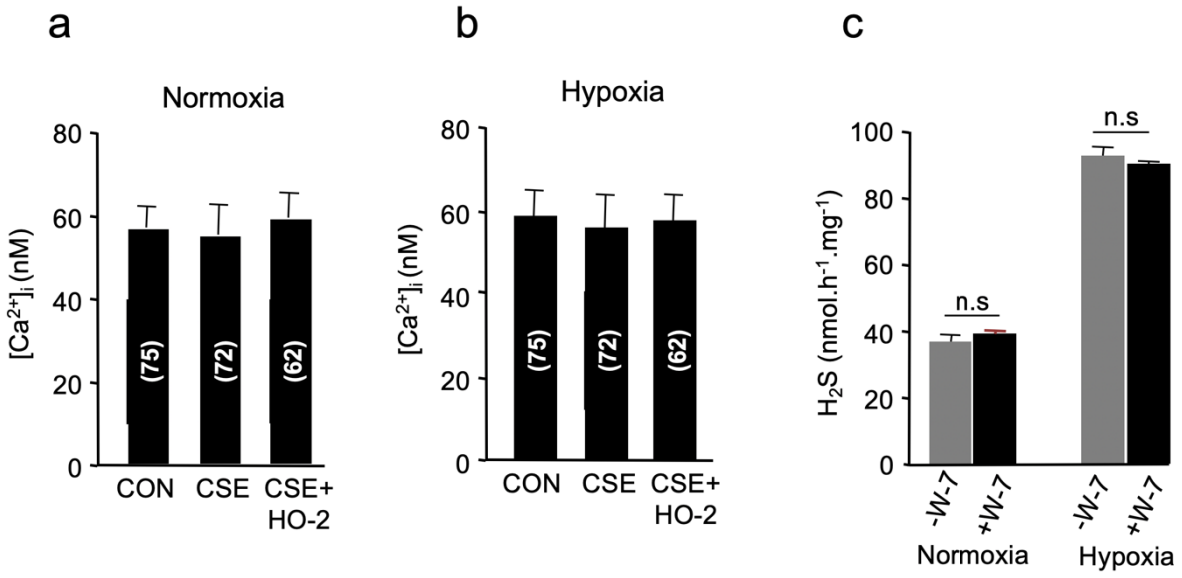

Figure 2. Calcium-dependent calmodulin activity is not required for inhibition of CSE by CO.

a-b, Intracellular calcium ($[Ca^{2+}]_i$) abundance in normoxia and hypoxia in HEK-293 cells expressing empty vector (CON) as compared to CSE or CSE+HO-2 expressing cells. n = 62-75 cells. **c**, Effect of W7, the calmodulin antagonist on H_2S generation in HO-2 + CSE-expressing cells. n = 3. Normoxia= PO_2 142 ± 3 mmHg and Hypoxia= PO_2 36±4 mmHg. Data represent mean ± SEM. n.s. = not significant, p >0.05.

CO binds to and activates soluble guanylyl cyclase (sGC) (Verma et al., 1993), which catalyzes the synthesis of the second messenger cyclic guanosine monophosphate (cGMP). To determine whether CO regulates H_2S generation through sGC/cGMP signaling, we challenged CSE-expressing cells with the CO donor $[Ru(CO)_3Cl_2]_2$ [tricarbonyldichlororuthenium (II) dimer] (CORM-2) (Motterlini, 2002). CORM-2 increased cGMP concentrations and reduced H_2S generation (**Fig. 3a-b**). Transfection of a small interfering RNA (siRNA) targeting the α1 subunit of sGC (**Fig. 4a**) prevented cGMP accumulation and preserved H_2S generation in CORM-2–treated cells (**Fig. 3a-b**).

To confirm that HO-2–derived CO stimulates sGC/cGMP signaling as does exogenous CO, we measured cGMP and H_2S concentrations in cells coexpressing HO-2 and CSE. Cells expressing HO-2 as well as CSE produced more cGMP under normoxia than did cells expressing only CSE (**Fig. 3c**). The increase in cGMP was associated with suppressed H_2S production (**Fig. 3d**). siRNA-mediated silencing of sGC reduced cGMP concentrations and prevented HO-2 from inhibiting H_2S generation under normoxia (**Fig. 3c-d**). Hypoxia, which inhibits HO-2 activity, reduced cGMP concentrations and increased H_2S generation. Hypoxia had no further effect on cGMP or H_2S concentrations in cells with sGC knockdown (**Fig. 4b-c**). Together, these results demonstrate that CO, through sGC/cGMP signaling, inhibited CSE-dependent H_2S production.

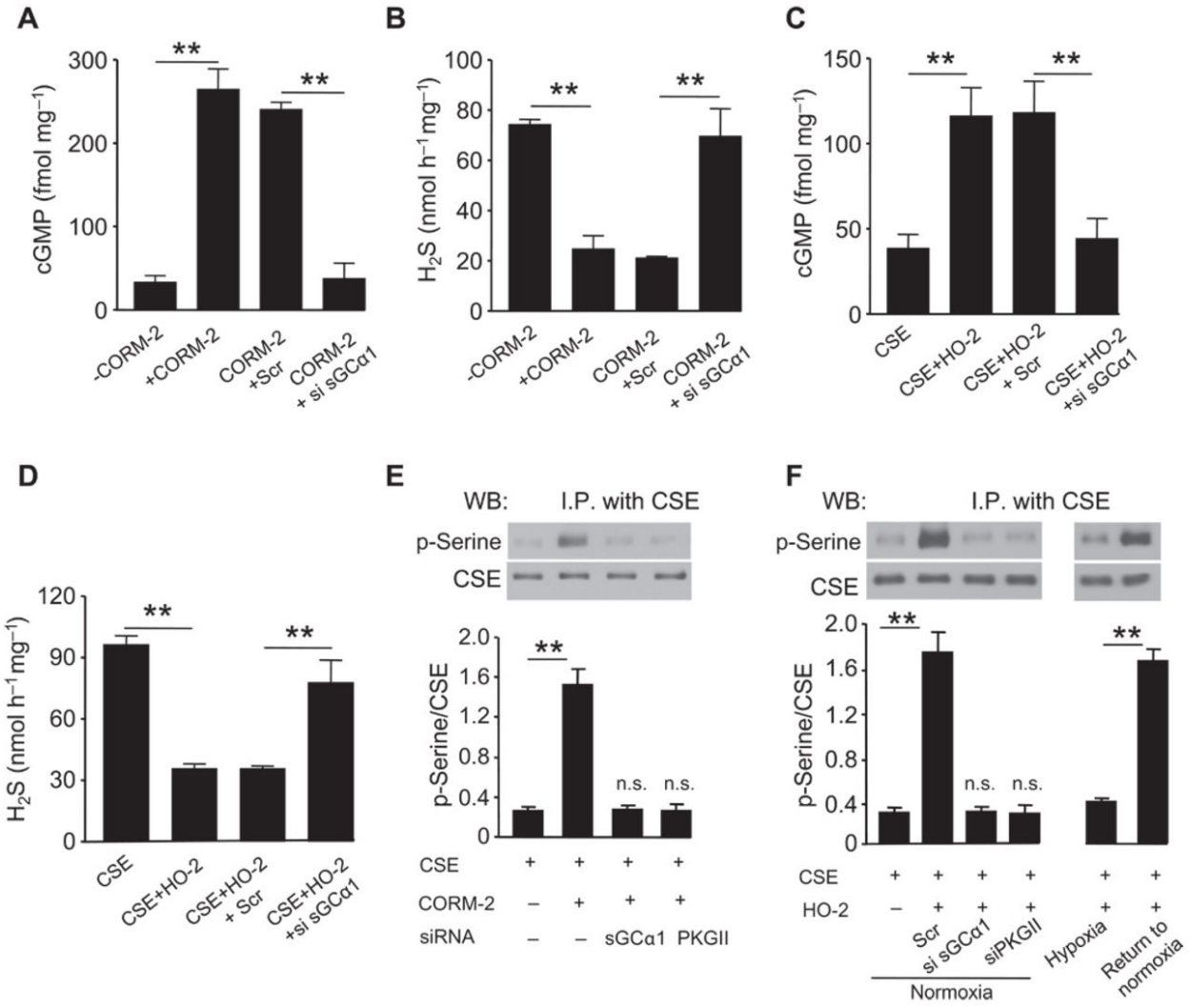

Figure 3. CO inhibits H_2S generation through sGC-dependent cGMP production.

a-d, Effects of siRNA silencing of sGCα1 on the generation of cGMP and H_2S in response to either the CO donor CORM-2 (*a* and *b*) or coexpression of HO-2 (*c* and *d*) in HEK-293 cells expressing CSE. Scr, scrambled RNA. **e-f**, Analysis of serine phosphorylation of CSE. Top: representative immunoblot; bottom: densitometric analysis. Effects of siRNA silencing of either sGCα1 or cGMP-dependent PKG II on serine phosphorylation in cells expressing CSE in response to CORM-2 (*e*) or in CSE/HO-2–coexpressing cells under normoxia or hypoxia or hypoxic cells returned to normoxia (*f*). The graphs in (*a-f*) represent means ± SEM (n = 4 to 5 independent experiments). $^{**}P < 0.01$.

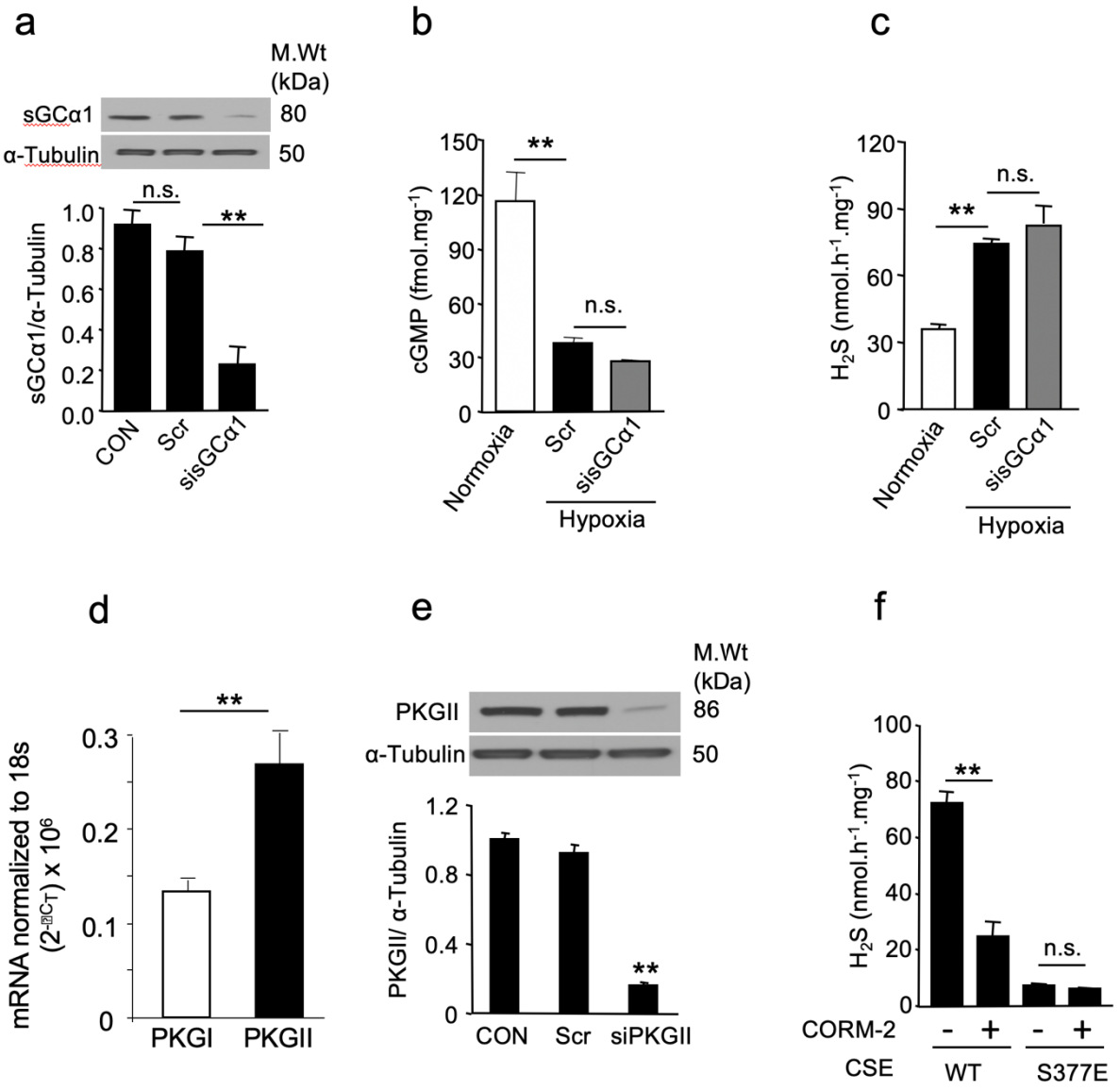

Figure 4. Effect of siRNA targeted to sGCα1 on hypoxia-evoked changes in cGMP and H_2S generation in HEK-293 cells.

a, sGCα1 protein expression in HEK-293 cells transfected with either scrambled (Scr) or sGCα1 siRNA. Representative immunoblots (*upper panel*) and densitometric analysis (*lower panel*). n= 3. **b-c**, Effect of hypoxia on cGMP abundance (*b*) and H_2S generation (*c*) in CSE+HO-2-expressing cells transfected with either scrambled (Scr) or sGCα1 siRNA. n =4. **d**, PKG I and II mRNA expressions in mouse carotid bodies was analyzed by reverse transcription and quantitative real-time PCR. n = 3 (2 carotid bodies/experiment). **e**, PKG II protein expression in HEK-293 cells transfected with either scrambled (Scr) or PKG II siRNA. Representative immunoblots (*upper panel*) and densitometric analysis (*lower panel*) are shown. n =3. **f**, Effect of CORM-2, a CO donor on H_2S generation in HEK-293 cells expressing either wild-type (WT) or S377E phospho-mimetic mutant CSE. n= 4. Data presented are mean ± SEM. $^{**}p < 0.01$, n.s. not significant, $p>0.05$.

CO induces protein kinase G–dependent phosphorylation of CSE

A major biological action of cGMP is the activation of cGMP-dependent protein kinase G (PKG) I and II, which phosphorylate serine and threonine residues in target proteins (Kennelly and Krebs, 1991). We explored whether activation of cGMP signaling by CO stimulates PKG to phosphorylate CSE. CSE immunoprecipitates from CSE-expressing HEK-293 cells were immunoblotted with antibodies recognizing phosphoserine. Treatment of CSE-expressing cells with CORM-2 induced an increase in the serine phosphorylation of CSE (**Fig. 3e**). Likewise, cells coexpressing HO-2 and CSE also exhibited a robust increase in serine phosphorylation of CSE under normoxia (**Fig. 3f**). siRNA-mediated silencing of either sGC or PKG II, which is more abundant in the mouse carotid body than PKG I (**Fig. 4d**), prevented phosphorylation of CSE evoked by CORM-2 in CSE/HO-2–coexpressing cells under normoxia (**Fig. 3e-f and Fig. 4e**). Exposure of HO-2/CSE–coexpressing cells to hypoxia markedly reduced phosphorylation of CSE, which completely recovered after being returned to normoxic conditions (**Fig. 3f**), demonstrating the reversible nature of O_2-dependent CSE phosphorylation.

We next sought to identify the serine residue in CSE that is phosphorylated by PKG. CSE belongs to a family of pyridoxal-5-phosphate–dependent enzymes {H:1982vb}. Sequence alignment of CSE across species revealed that Ser^{377} is located within a highly conserved putative PKG recognition sequence (**Fig. 6a**) (Kennelly and Krebs, 1991). Mutating Ser^{377} to alanine (S377A) abolished CORM-2– or HO-2–induced serine phosphorylation of CSE (**Fig. 6b-c**). Neither

CORM-2 nor HO-2 co-expression inhibited H_2S generation from cells expressing CSE^{S377A} (**Fig. 6d-e**). Cells expressing CSE with the phosphomimetic substitution S377E exhibited a >90% reduction in basal H_2S concentrations (**Fig. 4f**), suggesting that phosphorylation of Ser^{377} attenuated H_2S synthesis. Together, these results point to the reversible phosphorylation of Ser^{377} by PKG as a switch by which CO regulates H_2S generation by CSE.

PKG signaling inhibits H_2S generation and sensory nerve activity of the carotid body

We assessed the relevance of PKG regulation of CSE on carotid body function. Because carotid bodies produce high amounts of CO during normoxia (Peng et al., 2014), we hypothesized that activation of PKG by CO inhibits H_2S generation from CSE and maintains low sensory activity, whereas inhibiting PKG, similar to exposure to hypoxia, should increase H_2S concentrations and augment carotid body sensory nerve activity. Indeed, application of a PKG inhibitor, (Rp)-8-pCPT-cGMPS (8-pCPT), increased H_2S generation in a dose-dependent manner in wild-type carotid bodies with a concomitant increase in sensory nerve activity under normoxia (PO_2 = 142 ± 3 mmHg). However, the PKG inhibitor did not affect H_2S concentrations or sensory nerve activity in CSE-null carotid bodies (**Fig. 6a-d**).

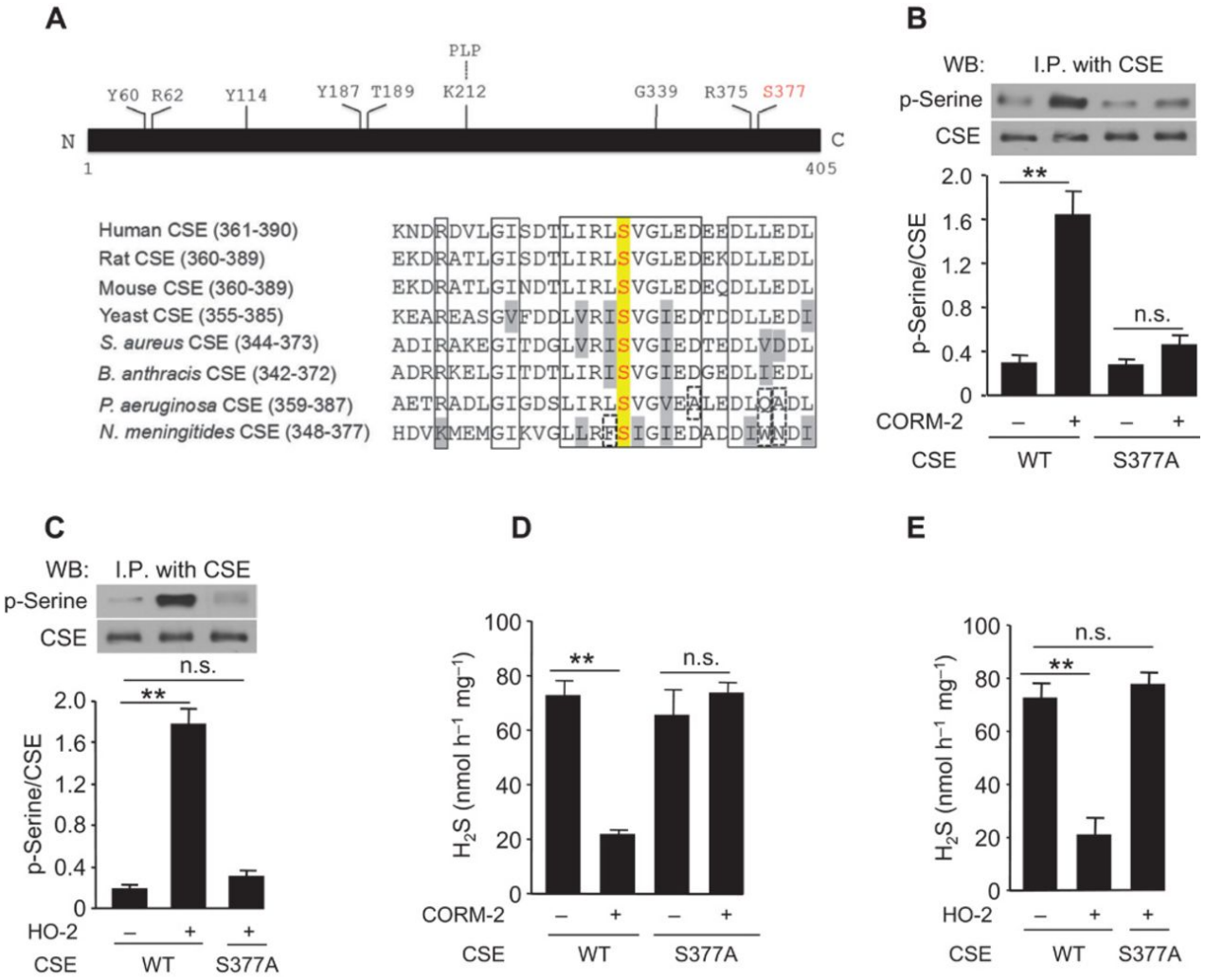

Figure 5. Inhibition of H_2S generation by CO requires phosphorylation of CSE at Ser^{377}.

a, Top: Amino acid residues in CSE required for H_2S generation. Bottom: Sequence alignment of CSE across species reveals that Ser^{377} is evolutionarily conserved (*red*). Conserved residues are outlined by a solid box. Conservative substitutions are shown in gray, and nonconservative substitutions are outlined by a dashed box. **b-c**, Comparison of the serine phosphorylation of exogenously expressed WT and mutant (S377A) CSE in cells treated with the CO donor CORM-2 (*b*) and in cells co-expressing HO-2 (*c*). Top: representative immunoblots; bottom: densitometric analysis. **d-e**, Effects of CORM-2 (*d*) and HO-2 expression (*e*) on H_2S generation in cells expressing WT or mutant CSE (S377A). The graphs in (*b-e*) represent means ± SEM (n = 3 to 4 independent experiments). $^{**}P < 0.01$.

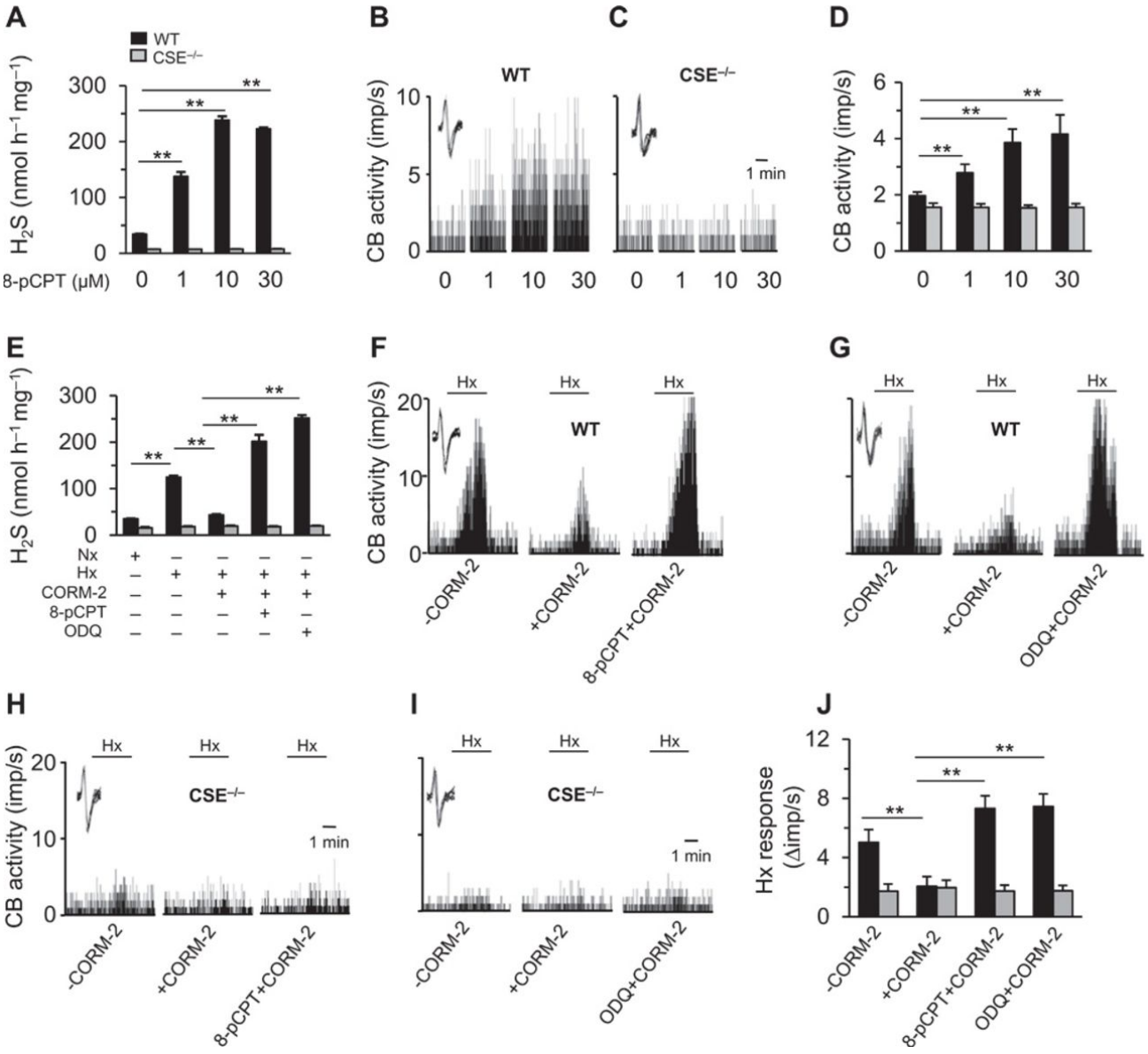

Figure 6. PKG-dependent cGMP signaling in the carotid body.

a-d, Effect of the PKG inhibitor 8-pCPT on (*a*) H_2S generation and (*b-d*) baseline sensory nerve activity of WT and $CSE^{-/-}$ mouse carotid bodies. **e-j,** Effect of CORM-2 on hypoxia-evoked (*e*) H_2S generation and (*f-j*) sensory nerve response of WT and $CSE^{-/-}$ mouse carotid bodies with or without 8-pCPT or the sGC inhibitor ODQ. The insets in the tracings of (*b*), (*c*), and (*f-i*) show superimposed action potentials of the sensory nerve fiber from which the integrated carotid body sensory nerve activity [CB activity; impulses per second (imp/s)] was derived. Black horizontal bars marked with "Hx" represent the duration of the hypoxic challenge (n = 3 independent experiments for H_2S measurements and n = 6 carotid bodies for each genotype and treatment for sensory nerve activity measurements). $^{**}P < 0.01$.

To further assess the role of CO-induced PKG signaling, we treated wild-type carotid bodies with the CO donor CORM-2 or the sGC activator YC-1 [3-(5′-hydroxymethyl-2′-furyl)-1-benzylindazole] (Friebe et al., 1996). Both CORM-2 and YC-1 blocked the increase in H_2S concentrations in response to hypoxia, and pretreating the carotid bodies with a PKG inhibitor or the sGC inhibitor ODQ (1*H*-[1,2,4]oxadiazolo[4,3-a]quinoxalin-1-one) prevented CORM-2 or YC-1 from inhibiting H_2S generation (**Fig. 6e and Fig. 7**), demonstrating that CO signals through the sGC/PKG pathway to inhibit H_2S generation. Neither activating nor inhibiting the sGC/PKG signaling pathway altered H_2S concentrations in CSE-null carotid bodies (**Fig. 6e and Fig. 7**), providing further evidence that CSE is the target of CO-induced sGC/PKG signaling. Likewise, both CORM-2 and YC-1 reduced carotid body sensory nerve excitation by hypoxia in wild-type but not in CSE-null carotid bodies, and these effects were reversed by either a PKG inhibitor or the sGC inhibitor ODQ (**Fig. 6f-j and Fig. 7**).

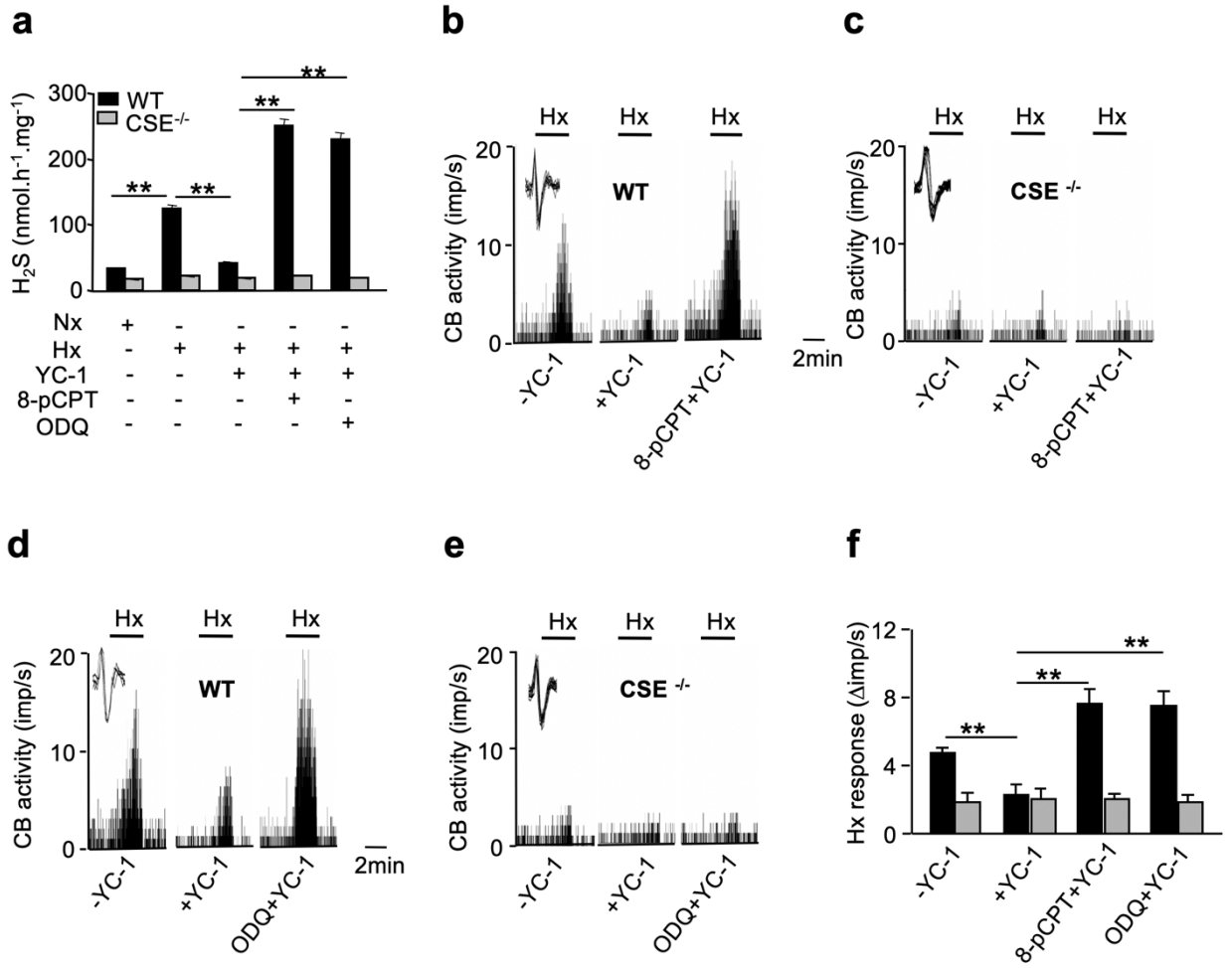

Figure 7. Inhibitory effects of YC-1, an activator of sGC on H_2S generation and the sensory nerve response of the carotid body.

a, Effect of YC-1 on hypoxia-evoked H_2S generation in carotid bodies of wild-type (WT) and CSE$^{-/-}$ mice without and with 8-pCPT, and ODQ, a PKG and sGC inhibitors, respectively. n= 3 for each genotype and treatment (6 carotid bodies/experiment). **b-f**, Effect of YC-1 on carotid body sensory nerve response to hypoxia in wild-type (WT) and CSE$^{-/-}$ mice without and with 8-pCPT or ODQ. Examples of the sensory nerve activity **b-e**, and average data of the hypoxic sensory nerve response (Hx response; **f**) are shown. n = 6 carotid bodies for each genotype. The duration of the hypoxic challenge in (*b-e*) is denoted by bars (Hx) and the insets represent superimposed action potentials of the sensory nerve fiber from which the data was derived. Normoxia (Nx) = pO_2 142 ± 3 mmHg, Hypoxia (Hx) = pO_2 36±4 mmHg. Data represent mean ± SEM. $^{**}p < 0.01$.

HO-2 governs O_2 sensing of the carotid body

The inherent O_2 sensitivity of HO-2 and its ability to regulate the generation of the effector molecule H_2S led us to investigate whether carotid body O_2 sensing is fundamentally governed by HO-2. In carotid bodies from wild-type

mice, HO-2 was present in glomus cells, which are the primary O_2-sensing cells of the carotid body (Kumar and Prabhakar, 2011), whereas HO-2 was absent in carotid bodies from HO-2–null mice (**Fig. 8a**), which exhibited a >90% reduction in CO production compared to wild-type carotid bodies (**Fig. 8b**). If HO-2–dependent CO generation is obligatory for carotid body O_2sensing, HO-2–null mice should exhibit augmented basal sensory nerve activity and H_2S concentrations in the carotid body. Indeed, H_2S generation and baseline sensory nerve activity were greater in HO-2–null carotid bodies than in wild-type (**Fig. 8c-e**). However, H_2S concentrations and sensory nerve activity still increased in hypoxia (**Fig. 8c-d and Fig. 8f**), suggesting the existence of a residual regulatory mechanism that does not involve HO-2. HO-2/CSE double-null carotid bodies did not exhibit a sensory nerve response to hypoxia, demonstrating that this residual O_2-sensing mechanism exploited H_2S generation by CSE to trigger sensory nerve excitation (**Fig. 8c-f**).

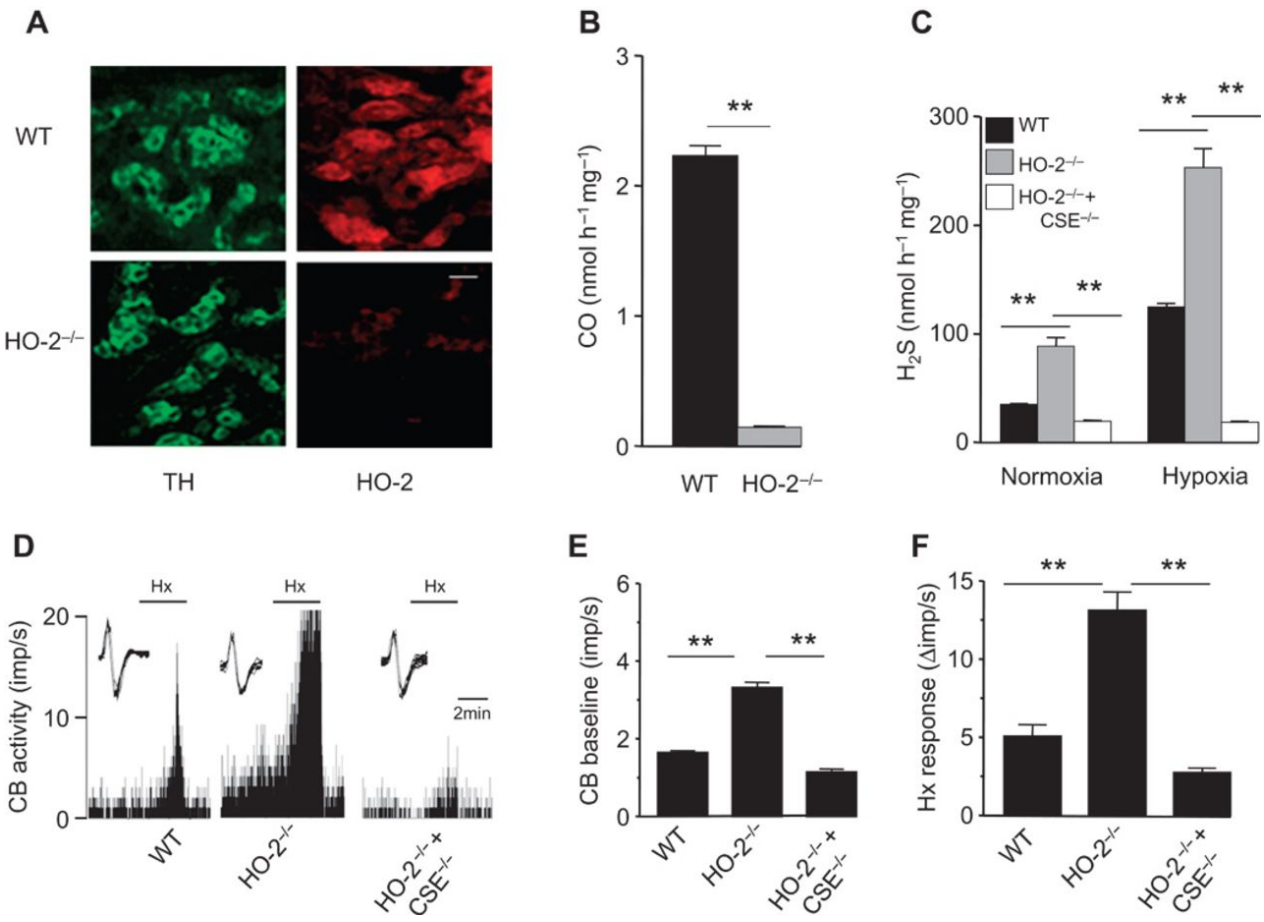

Figure 8. Gaseous messenger generation and sensory nerve activity in HO-2–null carotid bodies.

a, Adjacent carotid body sections immunostained for HO-2 and tyrosine hydroxylase (TH), a marker of glomus cells, in WT and HO-2$^{-/-}$ mice. Scale bar, 20 μm. **b**, CO generation in carotid bodies of WT and HO-2$^{-/-}$ mice. **c-f**, H_2S generation (*c*) and sensory nerve activity (*d-f*) of the carotid bodies of WT, HO-2$^{-/-}$, and HO-2$^{-/-}$ + CSE$^{-/-}$ mice. In tracings of (*d*), the insets present superimposed action potentials of the sensory nerve fiber from which the integrated carotid body sensory nerve activity (CB activity; imp/s) was derived, and black bars marked with "Hx" represent the duration of the hypoxic challenge. Images in (*a*) are representative of three mice per genotype. The graphs in (*b*), (*c*), (*e*), and (*f*) represent means ± SEM (n = 3 independent experiments for CO and H_2S measurements and n = 6 carotid bodies for each genotype for sensory nerve activity measurements). $^{**}P < 0.01$.

Neuronal nitric oxide synthase abundance is increased in HO-2–null glomus cells

Immunocytochemistry of HO-2–null carotid bodies revealed neuronal nitric oxide synthase (nNOS) staining in glomus cells (**Fig. 9a**). In contrast, nNOS staining was not detectable either in glomus cells or in nerve fibers of wild-type

carotid bodies (**Fig. 9a**). nNOS generates nitric oxide (NO) in an O_2-dependent manner (Prabhakar et al., 1993), and similar to CO, NO inhibits carotid body sensory nerve activity (Prabhakar and Semenza, 2012). Treatment of HO-2–null carotid bodies with the nNOS inhibitor 7-nitroindazole (7-NI) (Babbedge et al., 1993; Moore et al., 1993) increased baseline H_2S concentrations and sensory nerve activity, suggesting that NO could also be a physiological inhibitor of H_2S generation. 7-NI also eliminated the O_2 sensitivity of HO-2–null carotid bodies (**Fig. 9b-e**). 7-NI did not affect H_2S concentrations or sensory nerve activity in HO-2/CSE double-null carotid bodies (**Fig. 9b-e**).

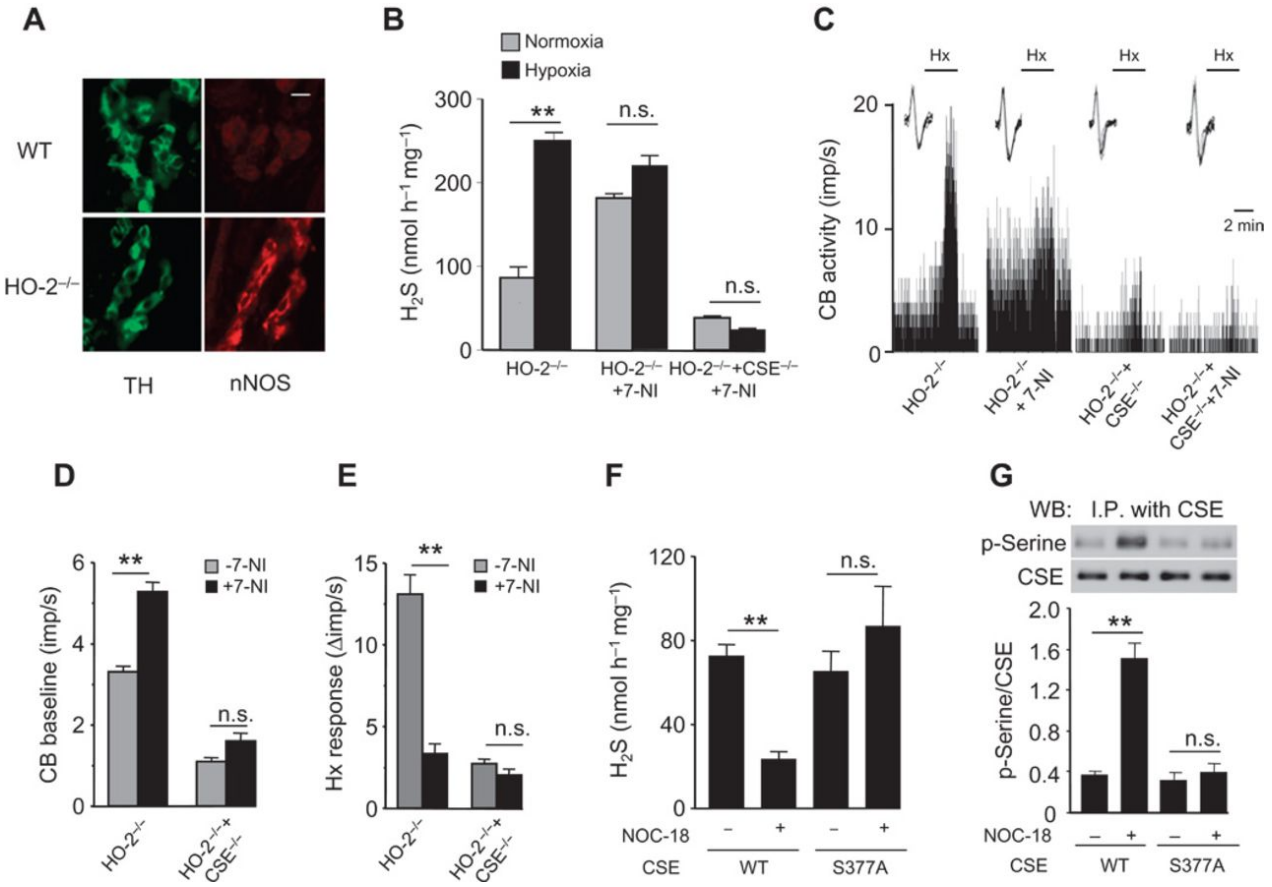

Figure 9. NO signaling in HO-2–null carotid body.

a, Adjacent carotid body sections immunostained for nNOS and tyrosine hydroxylase (TH), a marker of glomus cells, in WT and HO-2$^{-/-}$ mice. Scale bar, 20 μm. **b-e**, Effect of the nNOS inhibitor 7-NI on H_2S generation (*b*) and sensory nerve activity (*c-e*) of carotid bodies from HO-2$^{-/-}$ and HO-2$^{-/-}$ + CSE$^{-/-}$ mice. In tracings in (*c*), the insets present superimposed action potentials of the sensory nerve fiber from which the integrated carotid body sensory nerve activity (CB activity; imp/s) was derived, and black bars marked with "Hx" represent the duration of the hypoxic challenge. **f-g**, Effect of the NO donor NOC-18 on H_2S generation (*f*) and CSE serine phosphorylation (*g*) in HEK-293 cells expressing WT or mutant CSE (S377A). Images in (*a*) are representative of three mice per genotype. The graphs in (*b*) and (*d-g*) represent means ± SEM (n = 3 for each genotype and treatment for H_2S measurements, n = 6 to 8 carotid bodies for each genotype and treatment for sensory nerve activity measurements, and n = 3 independent experiments for H_2S measurements and CSE phosphorylation in HEK-293 cells). $^{**}P < 0.01$.

NO activates sGC (Arnold et al., 1977) and can thus substitute for CO in the same sGC/PKG signaling pathway to inhibit H_2S generation by CSE. To determine whether NO also inhibits H_2S generation by inducing the phosphorylation of CSE at Ser^{377}, we treated cells expressing CSE with the NO

donor NOC-18 [3,3-bis(aminoethyl)-1-hydroxy-2-oxo-1-triazene] (Shibuta et al., 1996). Similar to the CO donor, the NO donor decreased H_2S generation and increased serine phosphorylation of CSE in cells expressing wild-type CSE, but not in those expressing CSE^{S377A} (**Fig. 9f-g**). These results demonstrate that NO and CO regulate H_2S generation in a similar manner, through phosphorylation of CSE at Ser^{377}.

Discussion

Emerging evidence suggests that CO and H_2S are critical for O_2 sensing by the carotid body (Makarenko et al., 2012; Peng et al., 2010; 2014); however, the molecular mechanisms by which O_2 affect the generation of these gaseous messengers have been elusive. Our results establish that HO-2 is sensitive to changes in O_2availability, even in a heterologous system, such that CO generation is high under normoxia and low during hypoxia. This unique O_2 sensitivity requires Cys^{265} and Cys^{282}, which lower the O_2affinity of HO-2 and enable the enzyme to transduce changes in O_2 into changes in CO generation. The carotid body sensory nerve activity begins to increase only when the arterial blood PO_2 drops to anywhere between 60 and 80 mmHg [see (Kumar and Prabhakar, 2011) for references], which coincides with the apparent K_m of HO-2 for O_2 of ~65 mmHg. Thus, the low affinity of HO-2 for O_2 is physiologically critical to O_2 sensing by the carotid body.

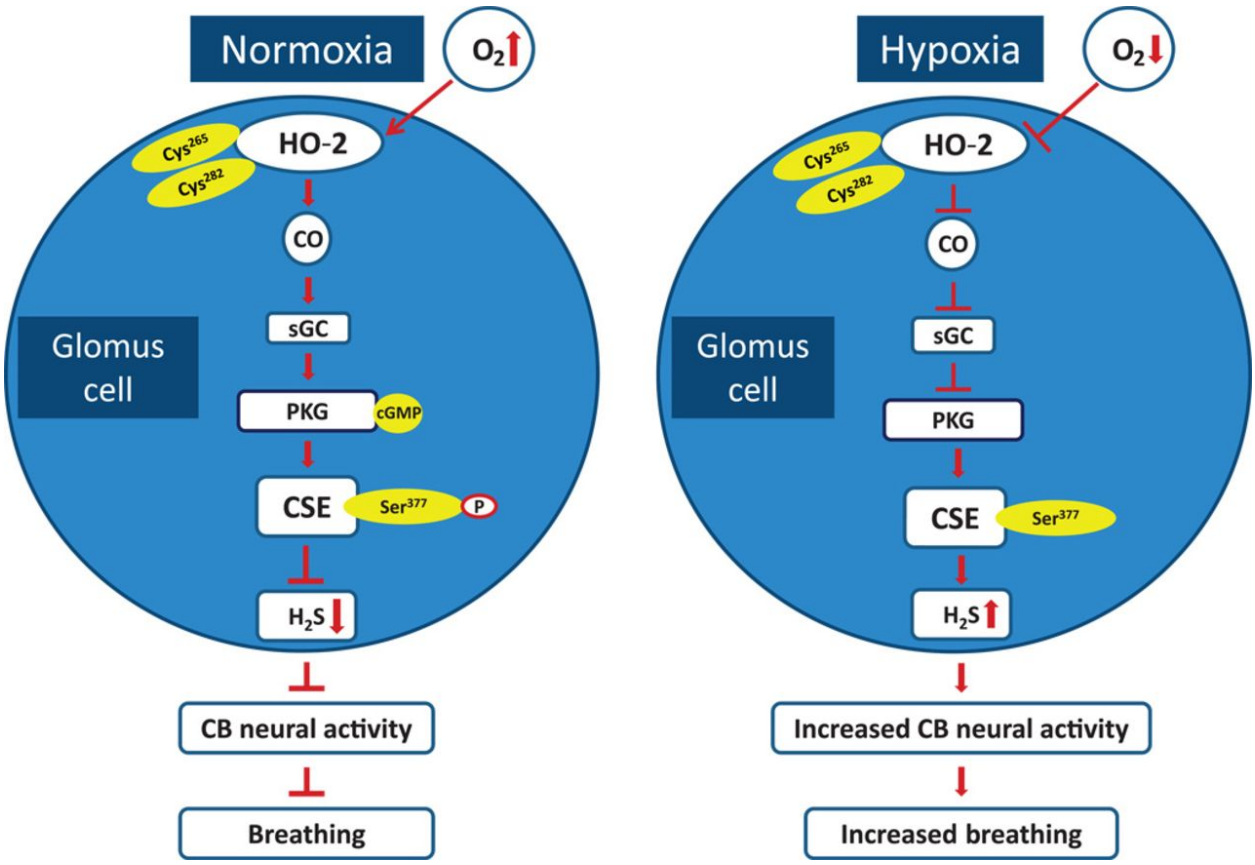

Figure 10. O_2 sensing in the carotid body.

Schematic presentation of the signaling pathways associated with the interplay between three gases—O_2, CO, and H_2S—in glomus cells of the carotid body (CB) and their impact on CB neural activity and breathing. Cys^{265} and Cys^{282} are located in the heme regulatory motif of HO-2. Ser^{377} is the target residue in the putative PKG recognition sequence in CSE.

In contrast, H_2S generation by CSE is not directly sensitive to changes in PO_2. CO is a physiological inhibitor of H_2S generation by CSE (Peng et al., 2010). Increased H_2S generation during hypoxia is due to decreased CO generation, resulting in reduced inhibition of CSE. CO inhibits CSE by stimulating sGC/PKG signaling, in contrast to the heme-dependent inhibition of CBS by CO (Morikawa et al., 2012; Shintani et al., 2009; Taoka and Banerjee, 2001; Taoka et al., 1999). PKG phosphorylates CSE at Ser^{377}, rendering it inactive. CSE phosphorylation is O_2-dependent and reversible, further

suggesting that this phosphorylation event functions in a signaling capacity. The complex interplay between three gases—O_2, CO, and H_2S—and its impact on carotid body sensory nerve activity and breathing is summarized in **Fig. 10**. The tight posttranslational regulation of CSE activity by PKG-dependent phosphorylation suggests a possible role for protein phosphatases and/or cGMP-dependent phosphodiesterases, which remain to be studied.

Alternative mechanisms for H_2S generation during hypoxia have been proposed in trout gill chemoreceptors (Olson et al., 2008a), in cyclostome blood vessels (Olson et al., 2008b), and in *Caenorhabditis elegans* neurons (Ma et al., 2012). Increased H_2S concentrations during hypoxia in lower vertebrates have been attributed to decreased oxidative degradation of H_2S (Olson et al., 2012). While such a mechanism may operate in lower vertebrates, our results indicate that in the mammalian carotid body, H_2S generation by CSE is not directly sensitive to changes in O_2; instead, it is regulated through O_2-dependent CO generation by HO-2.

A role for HO-2 in O_2 sensing by the carotid body has been previously proposed (Prabhakar et al., 1995; Williams, 2004). Consistent with this possibility, genetic knockout of HO-2, like hypoxia, increased the baseline sensory nerve activity and H_2S generation of the carotid body. However, we did find that HO-2–null carotid bodies still responded to hypoxia as previously reported (Ortega-Saenz, 2006). Further investigation revealed that loss of HO-2 in glomus cells prompts an unanticipated compensatory increase of another O_2-sensitive gaseous messenger–generating enzyme, nNOS, which catalyzes the

generation of NO. Although the mechanisms underlying the compensatory increase of nNOS in glomus cells of HO-2–null mice remain to be investigated, inhibition of nNOS eliminated sensory nerve excitation and H_2S generation in response to hypoxia in HO-2–null carotid bodies. The O_2 affinity of nNOS is much lower (apparent K_m = 350 μM or ~250 mmHg) (Prabhakar et al., 1993; Prabhakar and Semenza, 2012) than that of HO-2 (apparent K_m = 88 μM or ~65 mmHg), suggesting that even a modest reduction in PO_2 will lead to decreased NO production by nNOS. Similar to CO, NO also inhibits carotid body sensory nerve activity (Prabhakar et al., 1993; Prabhakar and Semenza, 2012) and inhibits CSE by inducing the phosphorylation of Ser^{377}. Collectively, these findings suggest that HO-2 governs carotid body O_2 sensing by affecting H_2S generation through PKG-dependent phosphorylation of CSE. In the absence of HO-2 activity, nNOS provides an alternative mechanism by which H_2S generation can be regulated according to O_2 availability, thereby providing an important fail-safe redundancy for a vital homeostatic process.

How might regulation of H_2S by either CO or NO contribute to O_2 sensing by the carotid body? The prevailing model of O_2 sensing by the carotid body suggests that hypoxia increases the sensory nerve activity by inhibiting O_2-sensitive K^+ channels in glomus cells, leading to depolarization-induced voltage-gated Ca^{2+} influx and release of neurotransmitter(s) to excite sensory nerve endings [see (Kumar and Prabhakar, 2011) for references]. Similar to hypoxia, H_2S increases carotid body sensory nerve activity by inhibiting O_2-sensitive K^+ channels in glomus cells, resulting in voltage-gated Ca^{2+} influx [see

(Prabhakar, 2013) for references]. Furthermore, hypoxia is ineffective in causing voltage-gated Ca^{2+} influx and neurotransmitter secretion in CSE-null glomus cells (Makarenko et al., 2012). Together, these findings suggest that H_2S transduces the hypoxic stimulus to changes in ion channel function and neurotransmitter release from glomus cells to elicit sensory nerve excitation.

Dysregulation of CO and H_2S production in the carotid body can give rise to an abnormal chemosensory reflex, resulting in pathological consequences such as hypertension, pulmonary edema, and poor ventilatory adaptation to hypoxia (Dempsey and Forster, 1982; Hackett et al., 1988; Peng et al., 2014; Tan et al., 2010; Trzebski, 1992). Solely by correcting abnormal CO or H_2S concentrations, it has been possible to successfully control hypertension in spontaneous hypertensive rats and prevent pulmonary edema in rats exposed to hypobaric hypoxia (Peng et al., 2014). Given the explosion of interest in surgically transecting carotid bodies as a therapeutic strategy in patients with essential hypertension and heart failure (Marcus et al., 2014; Paton et al., 2013), we believe that pharmacologically perturbing components of the sGC/PKG signaling pathway identified in this study is a more viable and safer approach for treating carotid body–related morbidities. Moreover, whereas gaseous messengers are important for O_2 sensing, their biological functions are by no means confined to it. It is becoming increasingly recognized that dysregulated gaseous signaling contributes to diverse diseases, including hypertension (Peng et al., 2014; Yang et al., 2008) and Parkinson's disease (Vandiver et al., 2013). Given that HO-2, NOS, and CSE are all present in the vasculature as well as in neurons (Kajimura

et al., 2010; Paul and Snyder, 2012; Paul et al., 2014), dysregulated crosstalk between CO, NO, and H_2S may contribute to the pathophysiology of these disorders. Accordingly, this newfound understanding of gaseous messenger signaling likely has substantial implications in a diverse set of physiological and pathophysiological conditions.

Materials and methods

Experimental Model and Subject Details

Mice

Animal care and use

All experiments were performed in accordance with protocols approved by the Animal Care and Use Committee at the University of Chicago and the Johns Hopkins University School of Medicine.

HO-2$^{-/-}$, CSE$^{-/-}$, and HO-2$^{-/-}$CSE$^{-/-}$ mice

Experiments were performed on age-matched, male C57BL/6J, HO-2$^{-/-}$ and CSE$^{-/-}$ mice (from S. H. Snyder and R. Wang) unless otherwise noted. Double HO-2 and CSE knockout mice were created by crossing HO-2$^{-/-}$ females with CSE$^{-/-}$ males. Animals were euthanized by intracardiac injection (0.1 ml) of euthanasia solution (Beuthanasia-D Special, Schering-Plough).

Cell culture

Human embryonic kidney 293 (HEK293) cells were cultured in DMEM (Gibco) supplemented with 10% FBS, 100 U/mL penicillin and streptomycin, and 2 mM glutamine at 37°C with 5% CO_2.

Method Details

Materials and preparation

Solvents and compounds were obtained as follows:

CORM-2 (Sigma-Aldrich, #288144), ODQ (Tocris Bioscience, #0880), YC-1 (Sigma-Aldrich, #Y102), 8-pCPT (Enzo Life Sciences, #BML-CN206-001), 7-NI (Tocris Bioscience, #0602), W7 (Tocris Bioscience, #0369), NOC-18 (Sigma-Aldrich, #A5581), and IBMX (Sigma-Aldrich, #I5879)

Material preparation:

All drugs were freshly prepared during the experiment. The following concentrations of drugs were used: CORM-2, 10 μM; 8-pCPT, 10 μM; ODQ, 15 μM; YC-1, 30 μM; W7, 100 μM; and NOC-18, 250 μM. In experiments involving HEK-293 cells, cells were treated with desired concentration of drugs 30 min before the experiment. In the studies with ex vivo carotid bodies, the chemoreceptor tissue was continuously superfused with desired concentration of drugs added to the reservoirs. In the experiments with 7-NI, mice were treated with 7-NI (10 mg/kg intraperitoneally) 1 hour before harvesting carotid bodies for recording sensory nerve activity.

Plasmids/cDNA

HO-2 (rat) was cloned into pcDNA3.1 with N-terminal myc tag. Mouse CSE was cloned into pCMV-myc. Mutations of HO-2 and CSE were performed using the QuikChange II XL mutagenesis kit (Agilent Technologies, #200521) according to the manufacturer's instructions. Mutations were verified by Sanger sequencing at the University of Chicago Core sequencing facility. HEK-293 cells were cultured in Dulbecco's modified Eagle's medium (Life Technologies, #11995-065), 10% fetal bovine serum, penicillin (100 U/ml), and streptomycin (100 U/ml) in 5% CO_2 atmosphere at 37°C. Cells were plated on 60-mm plates and transfected with 0.5 μg of plasmid pcDNA encoding either wild-type or mutant HO-2 and/or 2 μg of plasmid DNA encoding either wild-type or mutant CSE using Lipofectamine (Invitrogen, #18324-012) according to the manufacturer's protocol.

Immunoblot and immunoprecipitation assays

Immunoblot assays (HO-2, CSE, sGCα1, PKG II, and phosphoserine) and immunoprecipitation of CSE in HEK-293 cell lysates were performed as described (Yuan et al., 2013). The following primary antibodies were used: anti–HO-2 (1:1000; Abcam, #ab90492), anti-CSE (1:1000; Novus Biologicals, #NBP1-52849), anti-sGCα1 (1:1000; Abcam, #ab50358), anti-CGK2 (PKG II; 1:1000; Abcam, #ab110124), anti-phosphoserine (1:1000; Chemicon International, #AB1603), and anti–α-tubulin (1:1000; Sigma-Aldrich, #T6199).

Measurements of H_2S and CO

H_2S and CO generation in HEK-293 cells and carotid bodies was determined as previously described (Peng et al., 2010). In the experiments involving carotid

bodies, six tissues from three mice were pooled in a given experiment. In experiments assessing the effect of PO_2 on H_2S and CO generation, sealed tubes containing the reaction medium along with the center well were flushed with either 21% O_2 or varying proportions of O_2-N_2 gas mixtures for 15 min. PO_2 in the reaction medium was determined by a blood gas analyzer (ABL5, Radiometer). H_2S concentrations were calculated from a standard curve relating Na_2S concentration to absorption at 620-nm light. CO concentrations were calculated from a standard curve relating CORM-2 ($[Ru(CO)_3Cl_2]_2$; 1 mol of CORM-2 is equivalent to 0.7 mol of CO) to absorption at 590-nm light. The generation of H_2S and CO was expressed as nanomoles per hour per milligram of protein.

Measurements of cGMP

cGMP concentrations were determined by a chemiluminescent enzyme-linked immunosorbent assay (Cell Biolabs, # STA-506) according to the manufacturer's instructions. Before the experiment, cells were treated with 1 mM IBMX (3-isobutyl-1-methylxanthine) to inhibit degradation of cGMP by phosphodiesterases. cGMP concentrations were normalized to protein concentration as determined by bicinchoninic acid assay.

Measurements of intracellular calcium concentrations

Intracellular calcium concentrations ($[Ca^{2+}]_i$) in HEK-293 cells were measured using Fura-2AM as previously described (Makarenko et al., 2012). Background fluorescence was subtracted from signals. Image intensity at 340 nm was divided by 380-nm image intensity to obtain the ratiometric image. Ratios were

converted to free $[Ca^{2+}]_i$ using calibration curves constructed in vitro by adding Fura-2 (50 μM, free acid) to solutions containing known concentrations of Ca^{2+} (0 to 2000 nM). The recording chamber was continually superfused with solution from gravity-fed reservoirs.

Immunocytochemistry

Carotid bodies were harvested from anesthetized mice and perfused with heparinized saline followed by 4% paraformaldehyde for 30 min. Adjacent carotid body sections (8 μm thick) were immunostained with either rabbit anti–tyrosine hydroxylase antibody (1:4000; Pel-Freez, #P40101), rabbit anti–HO-2 antibody (1:200 dilution; Abcam, #ab90492), or rabbit anti-nNOS antibody (1:200; Cell Signaling, #4231) as previously described (Peng et al., 2010; 2014).

Carotid body sensory nerve activity

Sensory nerve activity was recorded from ex vivo carotid bodies harvested from anesthetized mice as previously described (Peng et al., 2010; 2014). Briefly, the carotid sinus nerve was treated with collagenase, and a few nerve bundles were isolated. Action potentials from one of the nerve bundles were recorded using a suction electrode (~20-μm-diameter tip). In general, two to three action potentials of varying size and amplitude were seen in a given nerve bundle. Action potentials of similar height, duration, and shape ("single" unit) were selected using Spike histogram software (LabChart 7 Pro) for analysis of the sensory nerve activity. To obtain a stable baseline sensory nerve activity, carotid bodies were first superfused for 1 hour with normoxia-equilibrated medium. Subsequently, baseline sensory nerve activity under normoxia was

recorded for 5 min. Sensory nerve responses to hypoxia were monitored for 3 min. The PO_2 in the medium was determined by a blood gas analyzer (ABL 5). Hypoxic response was measured as the difference between the sensory nerve activity under baseline and during hypoxia (Δimp/s).

Quantitation of PKG isoform mRNA

The mRNA expression of PKG I and PKG II was analyzed in the carotid bodies by quantitative real-time polymerase chain reaction (Bio-Rad), and the data were normalized with 18*S* mRNA as previously described (Nanduri et al., 2012). Two carotid bodies were pooled in a given experiment. The primers used for PKG I (Prkg1), PKG II (Prkg2), and 18*S* ribosomal RNA (rRNA) were as follows: Prkg1, CCTTGCAGGGGGAGGATGTAA (forward), TTGGCGAAGAAGGCAGCTTC (reverse); Prkg2, CTGCGGAGCAAAGTGGCAGA (forward), CCTGCAGCTTGTTCAGCTGGAT (reverse); 18*S* rRNA, GTAACCCGTTGAACCCCATT (forward), CCATCCAATCGGTAGTAGCG (reverse).

Quantification and Statistical Analysis

All data were reported as means ± SEM derived from three independent biological experiments, unless otherwise stated in the figure legends. Statistical analysis was performed with either one-way or two-way analysis of variance (ANOVA) with repeated measures followed by post hoc Tukey's test. For the analysis of normalized data, the Mann-Whitney test was used. *P* values <0.05 were considered significant.

Bilirubin links heme metabolism to neuroprotection by scavenging superoxide

Summary

Bilirubin is one of the most frequently measured metabolites in medicine, and yet its physiologic roles remain unclear. Bilirubin can act as an antioxidant *in vitro*, but whether its redox activity is physiologically-relevant is unclear because many other antioxidants are far more abundant *in vivo*. Here, we report that depleting endogenous bilirubin renders mice hypersensitive to oxidative stress. We find that mice lacking bilirubin are particularly vulnerable to superoxide ($O_2^{\bullet-}$) over other reactive oxidants and electrophiles. Whereas major antioxidants such as glutathione and cysteine exhibit little to no reactivity towards $O_2^{\bullet-}$, bilirubin readily scavenges $O_2^{\bullet-}$. We find that bilirubin's redox activity is particularly important in the brain, where it prevents excitotoxicity and neuronal death by scavenging $O_2^{\bullet-}$ during NMDA neurotransmission. Bilirubin's unique redox activity towards $O_2^{\bullet-}$ may underlie a prominent physiologic role despite being significantly less abundant than other endogenous and exogenous antioxidants.

Introduction

Bilirubin is one of the most frequently measured metabolites in clinical medicine, used to diagnose conditions such as hepatobiliary disorders (Osborn et al., 1959), hemolytic anemia (GIBLETT et al., 1956), and dyserythropoiesis (BERENDSOHN et al., 1964). It is the terminal product of mammalian heme metabolism, in which heme oxygenase (HO) oxidizes heme to biliverdin, which biliverdin reductase (BVR) then reduces to bilirubin (Kutty and Maines, 1981) (**Fig. 11a**). Despite being widely and regularly measured in patients, bilirubin is still largely considered a surrogate biomarker with little function, and its physiologic roles remain unclear. Bilirubin is also neurotoxic at high micromolar concentrations (CLAIREAUX et al., 1953). As bilirubin exhibits toxicity and has no obvious function, it has remained puzzling why diverse organisms evolved and retained the ability to produce it. However, bilirubin synthesis is dynamic, inducible, and tightly regulated, suggesting it may serve important physiologic functions. For example, bilirubin synthesis exhibits circadian periodicity (Kaasik and Lee, 2004) and is both temporally and spatially controlled during development (Falchuk et al., 2002). Bilirubin synthesis also rapidly increases during oxidative stress (Applegate et al., 1991), but why heme metabolism responds in this way is not completely clear.

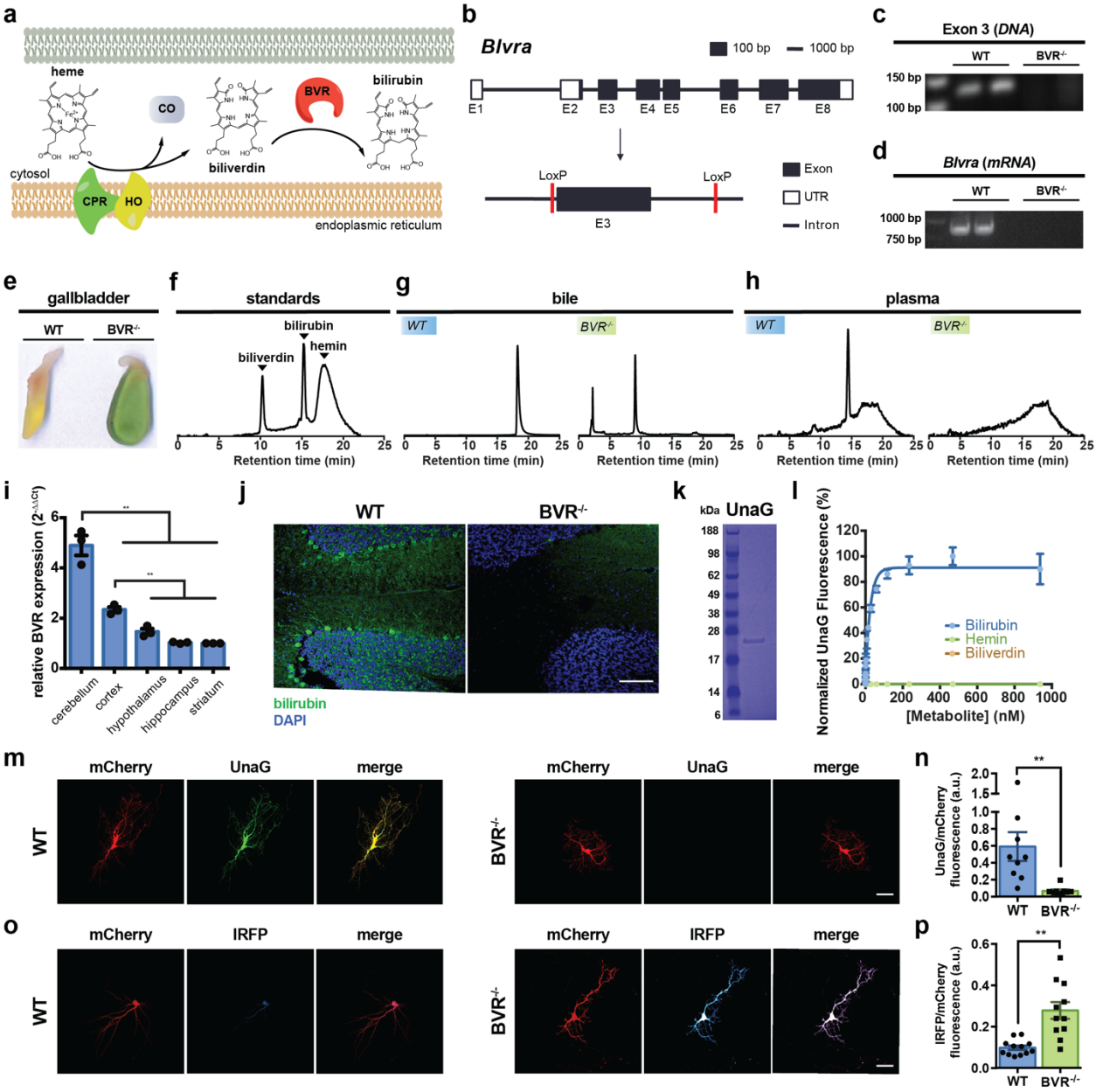

Figure 11. BVR$^{-/-}$ mice lack bilirubin and accumulate biliverdin.

a, Schematic diagram of heme catabolism, in which heme is oxidized by heme oxygenase (HO) and cytochrome P450 (CPR) to biliverdin. Biliverdin is subsequently reduced to bilirubin by biliverdin reductase (BVR). **b**, The *mus musculus Blvra* gene. **c-d**, PCR from somatic DNA for exon 3 (*c*) and RNA for full-length *Blvra* (*d*) from WT and BVR$^{-/-}$ mice. **e**, Representative photographs of gallbladders of WT and BVR$^{-/-}$ mice. **f**, Representative 405 nm HPLC chromatogram of 10 µM biliverdin, bilirubin, and hemin. **g**, Representative 405 nm HPLC chromatogram of bile pooled from 6 WT and BVR$^{-/-}$ mice. **h,** Representative 450 nm HPLC chromatogram of plasma from one WT and BVR$^{-/-}$ mice. **i,** *Blvra* RNA levels in different regions of the brain measured by quantitative PCR. Points represent individual mice. Mean ± SEM depicted. ** = $P < 0.01$ by two-way ANOVA followed by a *post hoc* Tukey test. **j**, Confocal images of bilirubin immunostaining in cerebellar sections from WT and BVR$^{-/-}$ mice. Scale bar = 100 µm. **k,** Coomassie blue gel of recombinantly purified UnaG. **l**, Ligand specificity for UnaG. Normalized fluorescence intensities of 1 µM

apoUnaG incubated with various concentrations of bilirubin, hemin, and biliverdin. Mean ± SEM depicted. **m-p**, Live-cell images of neurons co-expressing UnaG and mCherry (*m*) or IRFP and mCherry (*o*). (*m*) *left column*, mCherry; *middle column*, UnaG; *right column*, merged image. (*o*) *left column*, mCherry; *middle column*, IRFP; *right column*, merged image. *left row*, WT*; right row*, BVR$^{-/-}$. Scale bar = 50 μm. Mean UnaG fluorescence (*n*) and IRFP fluorescence (*p*) from WT and BVR$^{-/-}$ neurons transfected with UnaG (*n*) or IRFP (*p*) normalized to mCherry fluorescence as a transfection control. Points represent independent data points. Mean ± SEM depicted. n = 9-12 neurons per genotype per co-transfection. ** = $P < 0.01$ by two-tailed unpaired Student's t-test.

Some evidence suggests that bilirubin has antioxidant activity. However, whether bilirubin is a physiologic antioxidant is still a point of contention. Earlier conclusions were based on *in vitro* data (Stocker et al., 1987), experiments with exogenous bilirubin (Baranano et al., 2002; Doré and Snyder, 1999), and correlative findings from hyperbilirubinemic rats (Dennery et al., 1995). Moreover, these studies have not identified physiologically meaningful differences between bilirubin's and biliverdin's antioxidant activities despite being evolutionarily and chemically distinct metabolites (Jansen et al., 2010; Stocker et al., 1987), leaving bilirubin's specific biology obscure. Whether bilirubin is a physiologically-relevant antioxidant is also unclear because bilirubin is dwarfed by many more abundant antioxidants, some present at 10,000-fold higher concentrations (Maghzal et al., 2009; McDonagh, 2010). Despite this, several epidemiological studies suggest that mildly elevated serum bilirubin lowers the risk for ischemic stroke and coronary artery disease (Djousse et al., 2001; Perlstein et al., 2008; SCHWERTNER et al., 1994). The incidence of coronary artery disease in individuals with Gilbert's Syndrome, a genetic

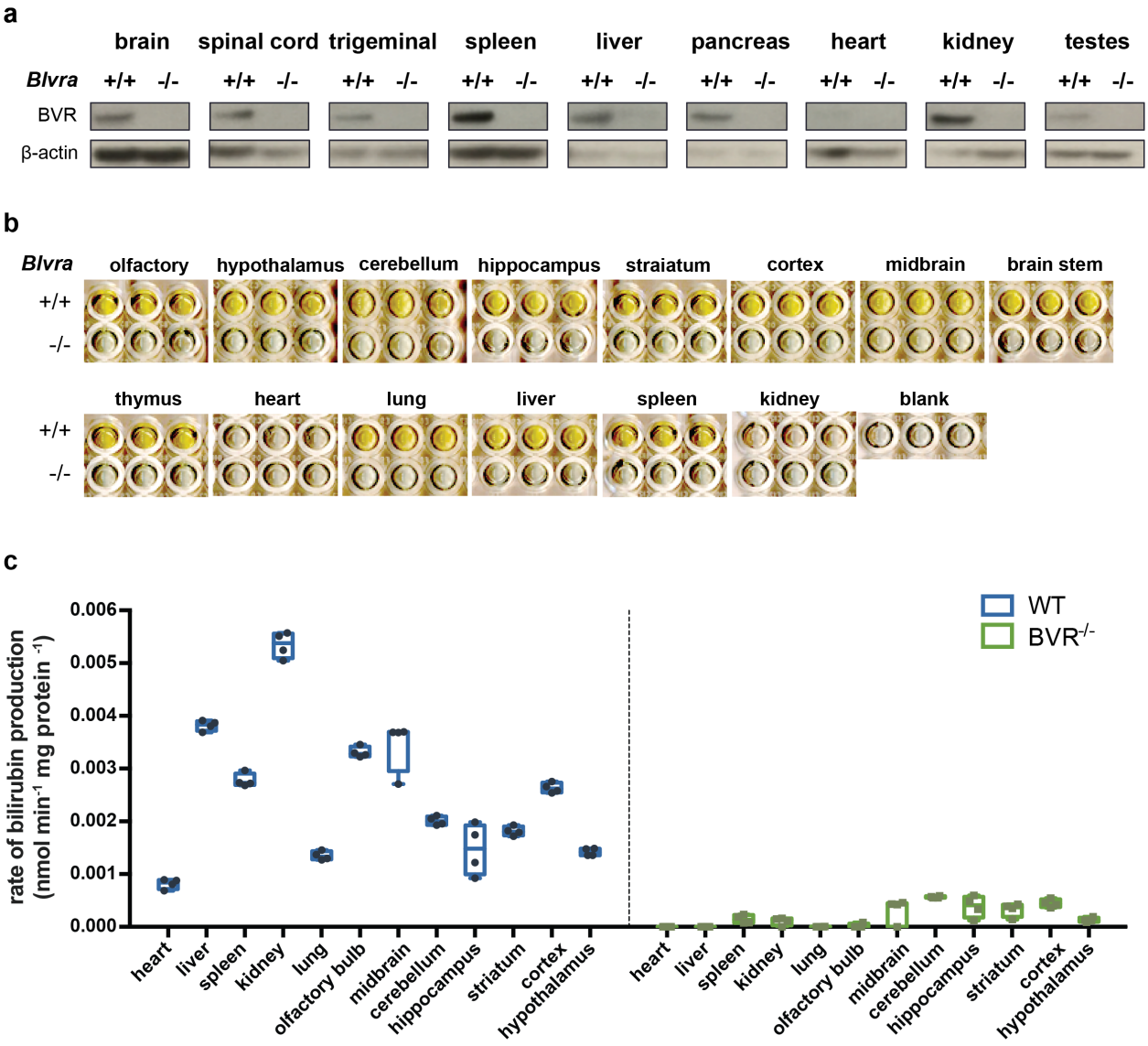

Figure 12. BVR$^{-/-}$ mice cannot synthesize bilirubin and accumulate biliverdin.

a, Western blots for BVR and β-actin from brains, spinal cords, trigeminal ganglia, spleens, livers, pancreases, hearts, kidneys, and testes of WT and BVR$^{-/-}$ mice. **b**, photographs of bilirubin produced from lysates of various tissues from WT and BVR$^{-/-}$ mice. The green pigment is biliverdin, whereas the yellow pigment is bilirubin. **c**, rates of bilirubin production in different tissues from WT and BVR$^{-/-}$ mice. Box and whisker plots depict the median and the 25th–75th percentiles with whiskers extending to data at the most extreme ends (i.e., below the 25th percentile or above the 75th percentile position). Points represent independent data points.

hyperbilirubinemia, is 5-fold lower than the general population (Vitek et al., 2002). While these studies hint at a physiologic role for bilirubin, they are

correlative and do not concretely identify bilirubin's physiologic functions. To directly evaluate whether bilirubin is a physiologic antioxidant, we generated a genetic mutant mouse model that selectively and globally lacks endogenous bilirubin.

Results

Depleting endogenous bilirubin renders cells vulnerable to oxidative death

Early work approached studying bilirubin by deleting the enzyme HO-2 (HO-2$^{-/-}$) (Doré et al., 2000; 1999), one of the two HO isoenzymes (Maines et al., 1986). However, HO-2$^{-/-}$ mice are confounded models for studying the redox biology of bilirubin, because they also accumulate heme and free iron (Dennery et al., 1998), both oxidants (TAPPEL, 1955). Here, we have generated a genetic mouse model that selectively lacks endogenous bilirubin without perturbing heme levels. To eliminate bilirubin, we targeted exon 3 of *Blvra*, thereby deleting BVR's obligate NAD(P)H-binding domain (Kikuchi et al., 2001) and ensuring that any splice variant cannot produce bilirubin (**Fig. 11b**). Compared with WT mice, BVR$^{-/-}$ mice appear grossly normal. We confirmed loss of *Blvra* DNA and mRNA by PCR (**Fig. 11c-d**) and BVR protein by western blot analyses of various tissues (**Fig. 12a**). BVR$^{-/-}$ tissues do not produce bilirubin even when supplemented with biliverdin, demonstrating a general inability to generate bilirubin (**Fig. 12b-c**). HPLC analyses of bile from WT and BVR$^{-/-}$ gallbladders (**Fig. 11e-g**) indicate a loss of endogenous bilirubin and an accumulation of biliverdin in BVR$^{-/-}$ mice. Similarly, HPLC analyses of plasma (**Fig. 11f and 1h**

and Fig. 13a-c) indicate loss of endogenous bilirubin. Biliverdin levels are below the limit of detection in both WT and BVR$^{-/-}$ plasma. Feces from BVR$^{-/-}$ mice are still pigmented despite lacking bilirubin, presumably because biliverdin is still readily excreted in bile (Gåfvels et al., 2009; Nytofte et al., 2011). Unlike HO-2$^{-/-}$ mice, BVR$^{-/-}$ mice exhibit unaltered plasma heme (**Fig. 11f and Fig. 13b and 13d**) and HO-2 expression (**Fig. 13e-j**), establishing BVR$^{-/-}$ mice as useful tools

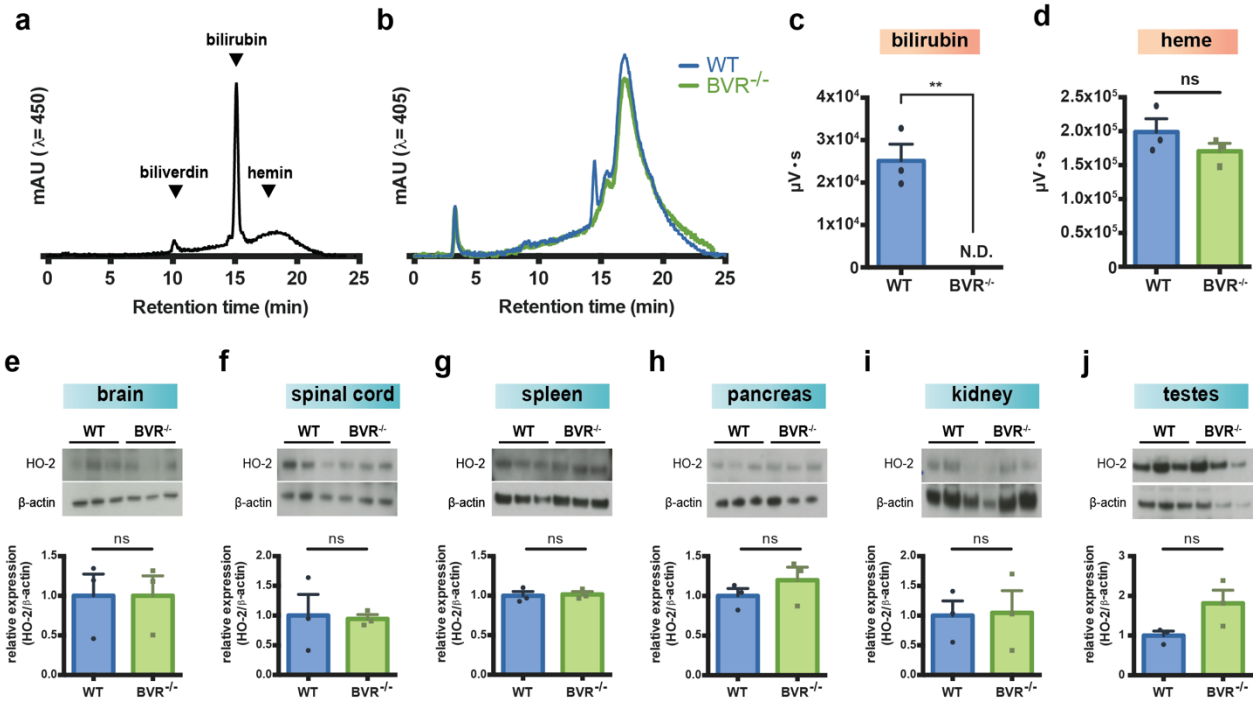

Figure 13. Epistatic heme catabolism is unaltered in BVR$^{-/-}$ mice.

a, Representative HPLC chromatogram of 10 μM biliverdin, bilirubin, and hemin standards. Absorbance was measured at 450 nm. **b**, Representative HPLC chromatogram of plasma from WT and BVR$^{-/-}$ mice. Absorbance was measured at 405 nm. **c**, Relative quantification of plasma bilirubin in WT and BVR$^{-/-}$ mice via HPLC as detected by absorbance at 450 nm. Points represent individual mice. N.D. = not detected. Mean ± SEM depicted. ** = $P < 0.01$ by two-tailed unpaired Student's t-test. **d**, Relative quantification of plasma heme in WT and BVR$^{-/-}$ mice via HPLC as detected by absorbance at 405 nm. Points represent individual mice. Mean ± SEM depicted. ns = $P > 0.05$ by two-tailed unpaired Student's t-test. **e-j**, *above*, western blots for HO-2 and β-actin from brains, spinal cords, spleens, pancreases, kidneys, and testes of WT and BVR$^{-/-}$ mice. *below*, relative quantification of HO-2 expression in each tissue. Points represent individual mice. Mean ± SEM depicted. ns = $P > 0.05$ by two-tailed unpaired Student's t-test.

to specifically assess the redox biology of bilirubin without confounding effects from heme and iron.

To assess bilirubin function *in vivo*, we first examined BVR expression in WT mice (**Fig. 14a-b**). BVR protein is variably expressed, with lowest expression in the heart and highest expression in the brain, spinal cord, spleen, and kidney. Within the brain, BVR mRNA is enriched in the cerebellum, double that of the cerebral cortex and almost five times higher than the corpus striatum (**Fig. 11i**). To determine where bilirubin might function in the brain, we assessed its localization immunohistochemically. Bilirubin exhibits discrete enrichment in neurons, with striking localization to Purkinje and some granule cells in the cerebellum (**Fig. 11j**). We also assessed the neuronal distribution of bilirubin with UnaG (**Fig. 11k**), a protein that fluoresces upon binding bilirubin (Kumagai et al., 2013). UnaG is highly specific for bilirubin with an EC_{50} of 15 ± 1 nM and does not fluoresce with heme or biliverdin (**Fig. 11l**). UnaG fluoresces in isolated cultures of WT but not $BVR^{-/-}$ neurons (**Fig. 11m-n**), suggesting that WT neurons autonomously produce bilirubin. In an analogous approach, we also expressed a phytochrome-based near-infrared fluorescent protein (IRFP) that fluoresces upon binding biliverdin (Filonov et al., 2011). $BVR^{-/-}$ neurons exhibit over 3 times greater IRFP fluorescence than WT neurons, consistent with an accumulation of biliverdin due to loss of BVR (**Fig. 11o-p**).

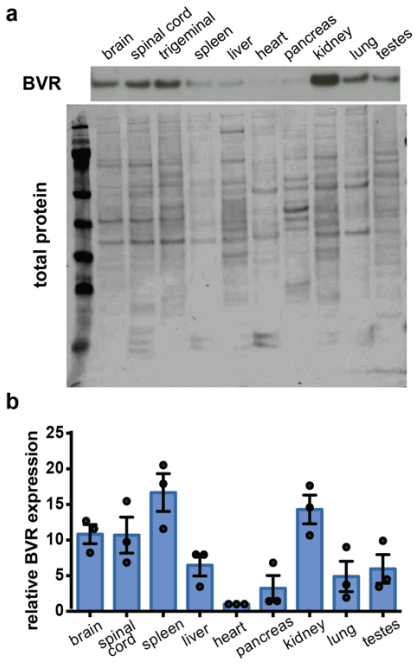

Figure 14. BVR expression across tissues.

a, Representative western blots for BVR and total protein from brains, spinal cords, trigeminal ganglia, spleens, livers, hearts. pancreases, kidneys, lungs, and testes of male WT mice. **b**, BVR expression across various tissues by western blot normalized to tissue expressing the least BVR. Points represent individual mice. Mean ± SEM depicted.

$BVR^{-/-}$ cells are specifically hypersensitive to $O_2^{\bullet-}$

To assess whether removing endogenous bilirubin renders cells sensitive to oxidative stress, we challenged fibroblasts (MEFs) from WT and $BVR^{-/-}$ littermate mice with various oxidants and electrophiles. $BVR^{-/-}$ MEFs are highly vulnerable to oxidative death (**Fig. 15a**) and are particularly sensitive to the superoxide ($O_2^{\bullet-}$) donors pyrogallol, paraquat, and menadione. $BVR^{-/-}$ MEFs are comparatively mildly sensitive to the oxidant hydrogen peroxide (H_2O_2) and the electrophile 4-hydroxynonenal (4-HNE). $BVR^{-/-}$ MEFs are also unable to clear reactive oxygen species (ROS) as efficiently as WT MEFs after exposure to menadione, as measured by the fluorescent redox probe dihydroethidium (DHE)

(**Fig. 15b**). Virally reintroducing *BLVRA* into the genome of $BVR^{-/-}$ MEFs restores their vulnerability to pyrogallol (**Fig. 16**), indicating that $BVR^{-/-}$ cells are prone to oxidative death specifically due to loss of BVR. Because $BVR^{-/-}$ cells lack bilirubin but also accumulate biliverdin, we treated MEFs with biliverdin to test whether excess biliverdin sensitizes cells to oxidative stress. However, biliverdin does not alter WT cells' baseline viability or susceptibility to oxidative stress (**Fig. 17**), suggesting that biliverdin itself is not toxic.

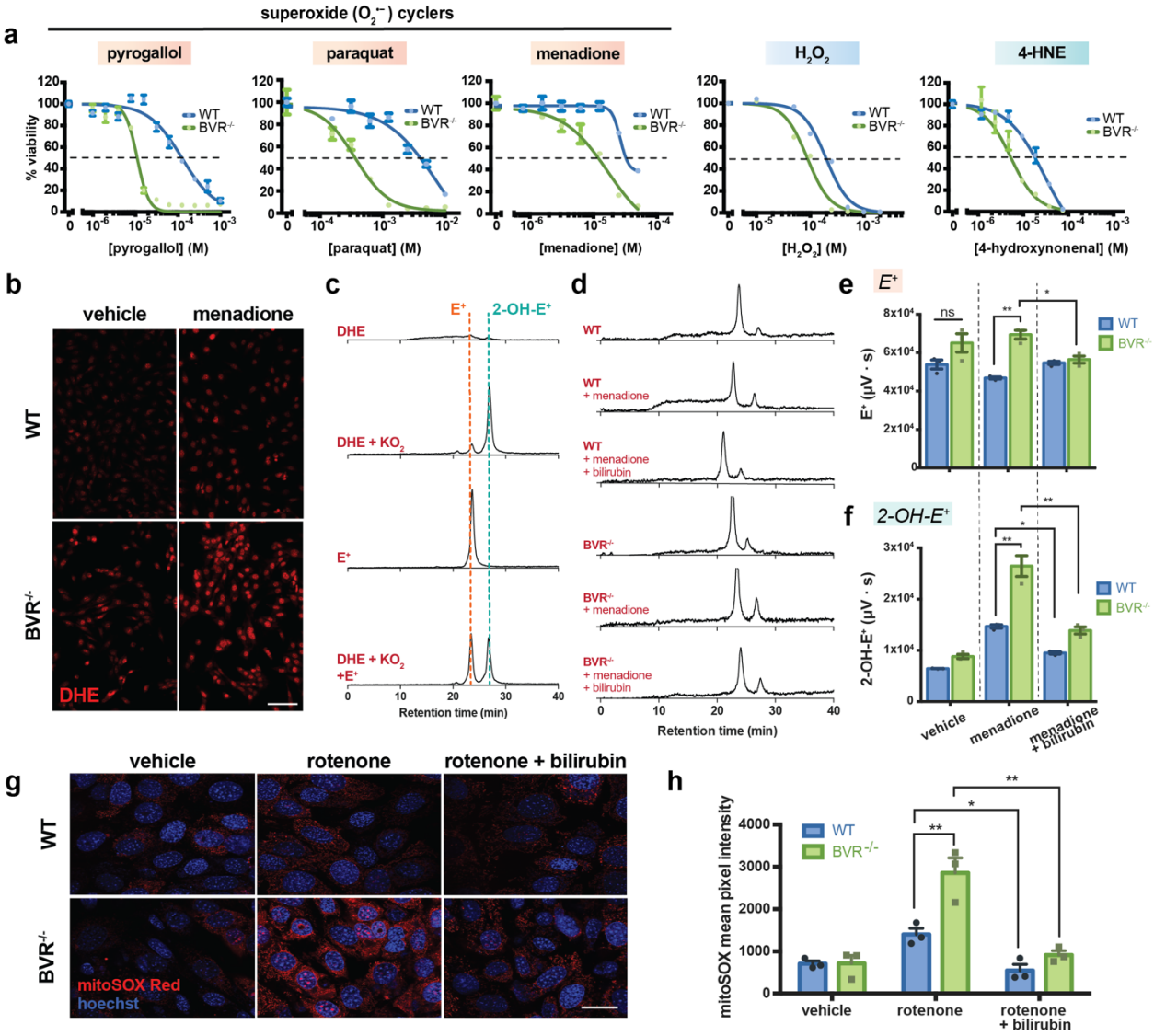

Figure 15. BVR$^{-/-}$ cells are hypersensitive to exogenous and endogenous $O_2^{\bullet-}$ over other ROS and electrophiles.

a, WT and BVR$^{-/-}$ MEF viability after 8 h exposure to varying concentrations of pyrogallol, paraquat ,menadione, H_2O_2, or 4-hydroxynonenal (4-HNE). Mean ± SEM depicted. *n* = 2-4 in triplicate. **b**, Live-cell images of dihydroethidium (DHE) fluorescence from WT and BVR$^{-/-}$ MEFs after exposure to 25 μM menadione for 1 h. Scale bar = 100 μm. **c**, Representative HPLC chromatograms of DHE alone, DHE + KO_2, authentic ethidium (E^+), and DHE + KO_2 spiked with authentic E^+. **d-f**, (*d*) Representative normalized HPLC chromatograms of organic extracts from WT and BVR$^{-/-}$ MEFs loaded with DHE at baseline or after treatment with 25 μM menadione for 1 h. Cells treated with bilirubin were pre-treated with 500 nM bilirubin for 30 min just prior to menadione. (*e-f*) Relative quantification of E^+ and 2-OH-E^+ extracted from WT and BVR$^{-/-}$ MEFs. Points represent independent data points. Mean ± SEM depicted. * = P < 0.05 and ** = P < 0.01 by two-way ANOVA followed by a *post hoc* Tukey test. **g-h,** Live-cell images (*g*) and quantification (*h*) of MitoSOX Red fluorescence WT and BVR$^{-/-}$ MEFs after exposure to 25 μM rotenone for 4 h. Cells treated with bilirubin were pre-treated with 500 nM bilirubin for 30 min just prior to rotenone. Scale bar = 25 μm. Points represent independent data points. Mean ± SEM depicted. * = *P* < 0.05 and ** = *P* < 0.01 by two-way ANOVA followed by a *post hoc* Tukey test.

BVR is a remarkably pleiotropic protein. Apart from reducing biliverdin to bilirubin, BVR functions as an enzyme-linked receptor at the plasma membrane (Wegiel et al., 2009) and as a kinase (Lerner-Marmarosh et al., 2008; 2005). These alternative functions lead to elevated AKT and MAPK signaling (Hinds et al., 2016; Lerner-Marmarosh et al., 2008; Wegiel et al., 2009), both of which promote cell survival during oxidative stress. However, we observe no difference in the expression, phosphorylation, or nuclear translocation of AKT or ERK1/2 between WT and BVR$^{-/-}$ MEFs (**Fig. 18a-b**), leading us to focus on BVR's canonical enzymatic activity instead.

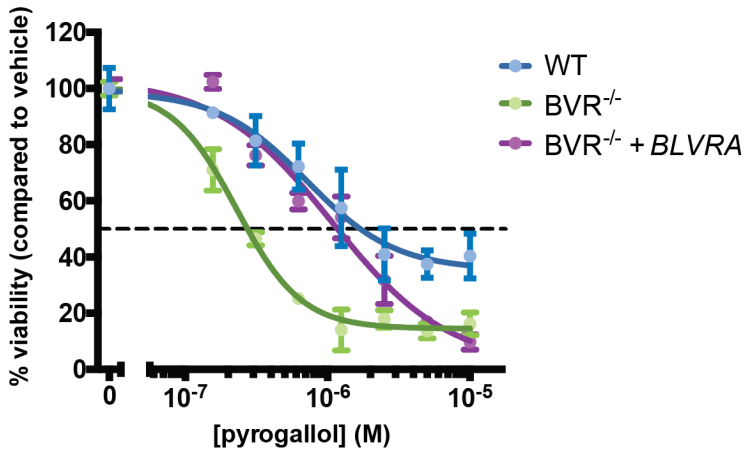

Figure 16. Reintroducing *BLVRA* back into the genome of BVR$^{-/-}$ MEFs mitigates their sensitivity to pyrogallol.

Viability of WT MEFs, BVR$^{-/-}$ MEFs, or BVR$^{-/-}$ MEFs expressing virally-reintroduced *BLVRA* after 8 h exposure to varying concentrations of pyrogallol. Mean ± SEM depicted. n = 2 in triplicate.

BVR$^{-/-}$ cells are markedly more sensitive to the three different $O_2^{\bullet-}$ cyclers over other oxidants and electrophiles (**Fig. 15a**), suggesting that bilirubin may physiologically interact with $O_2^{\bullet-}$. Regulating $O_2^{\bullet-}$ is critical, because it is the immediate product of reduced O_2 and is the precursor to several other ROS.

Despite its name, $O_2^{\bullet-}$ is not particularly "super" in its reactivity, because its doublet electronic configuration results in a kinetic spin barrier, while its anionic character limits reactivity with other electron-rich centers (Bielski and Richter, 1977; Bielski et al., 1985; FEE, 1982; Sawyer and Valentine, 2002). Accordingly, $O_2^{\bullet-}$ is not readily scavenged by the major endogenous small molecule antioxidants in humans (such as glutathione, cysteine, uric acid, melatonin, and lipoic acid) at physiologically-relevant rates (Jones et al., 2002; Kuzkaya et al., 2005; Winterbourn and Metodiewa, 1999). Superoxide dismutase enzymes (SODs) scavenge $O_2^{\bullet-}$ (MCCORD and I, 1969), but are restricted to soluble cellular compartments. However, $O_2^{\bullet-}$ is often produced within aprotic intramembranous compartments, which are more accessible to lipophilic molecules like bilirubin than to SODs. SODs are also imperfect antioxidants because they also convert $O_2^{\bullet-}$ to H_2O_2, another oxidant.

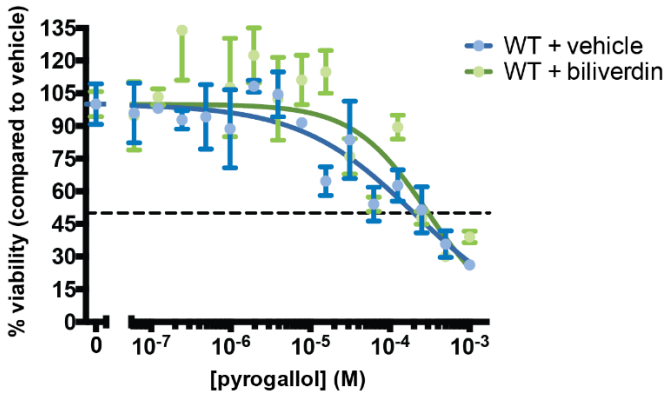

Figure 17. Excess biliverdin does not render MEFs hypersensitive to oxidative stress.

Viability of WT MEFs treated after 24 h exposure to varying concentrations of pyrogallol. Cells were treated with vehicle or 10 μM biliverdin for 1 h just prior to pyrogallol. Mean ± SEM depicted. n = 2 in triplicate.

We leveraged DHE to measure whether BVR$^{-/-}$ cells accumulate $O_2^{\bullet-}$, as DHE reacts with $O_2^{\bullet-}$ to form the specific fluorescent product 2-hydroxyethidium (2-OH-E$^+$). However, DHE also reacts with other oxidants to form ethidium (E$^+$). Both 2-OH-E$^+$ and E$^+$ exhibit similar fluorescence spectra and thus must be separated by HPLC in order to specifically quantify intracellular $O_2^{\bullet-}$ (Zhao et al., 2005; 2003). Using the method established by Zhao and colleagues to resolve 2-OH-E$^+$ and E$^+$ (**Fig. 15c**), we measured formation of 2-OH-E$^+$ and E$^+$ within WT and BVR$^{-/-}$ cells at baseline and after exposure to menadione (**Fig. 15d-f and Fig. 19a-c**). BVR$^{-/-}$ cells produce slightly more 2-OH-E$^+$ at baseline than WT cells, although the difference is statistically insignificant. As expected, treating both WT and BVR$^{-/-}$ cells with menadione results in more 2-OH-E$^+$. However, BVR$^{-/-}$ extracts have almost two-fold more 2-OH-E$^+$ than WT extracts, suggesting that removing endogenous bilirubin leads to an accumulation of $O_2^{\bullet-}$. Conversely, loading WT and BVR$^{-/-}$ cells with extracellular bilirubin reduces 2-OH-E$^+$ formation by approximately one-third. To confirm that extracellular bilirubin can enter cells, we applied bilirubin to cells expressing UnaG and measured changes in intracellular fluorescence. Because BVR$^{-/-}$ neurons do not exhibit basal fluorescence when transfected with UnaG (**Fig. 11m**), we expressed UnaG in BVR$^{-/-}$ neurons in order to directly correlate changes in UnaG fluorescence with extracellular bilirubin entering the cell. UnaG fluorescence increases within seconds of applying bilirubin (**Fig. 20a-b**), evidence that extracellular bilirubin can enter cells.

$O_2^{\bullet-}$ is generated by various processes *in vivo*, but most commonly forms in mitochondria when electrons leak from Complexes I – III of the electron transport chain to O_2 (Miwa et al., 2003; Murphy, 2009). $O_2^{\bullet-}$ is often retained in the matrix or intramembranous spaces because its negative charge prevents passive diffusion outward. We examined whether bilirubin localizes to mitochondria by heterologously expressing mitochondrial-targeted UnaG (mitoUnaG) (Kumagai et al., 2013; Park et al., 2016). MitoUnaG fluoresces and localizes with mitochondrial-targeted blue fluorescent protein (mitoBFP) (**Fig. 21a**), indicating that endogenous bilirubin localizes to mitochondria. To determine if bilirubin must be produced within mitochondria or if extracellular/cytoplasmic bilirubin can diffuse in, we applied exogenous bilirubin and monitored mitoUnaG fluorescence as performed previously (Park et al., 2016). MitoUnaG fluorescence increases within seconds (**Fig. 21a**), implying that bilirubin can rapidly diffuse across mitochondrial membranes.

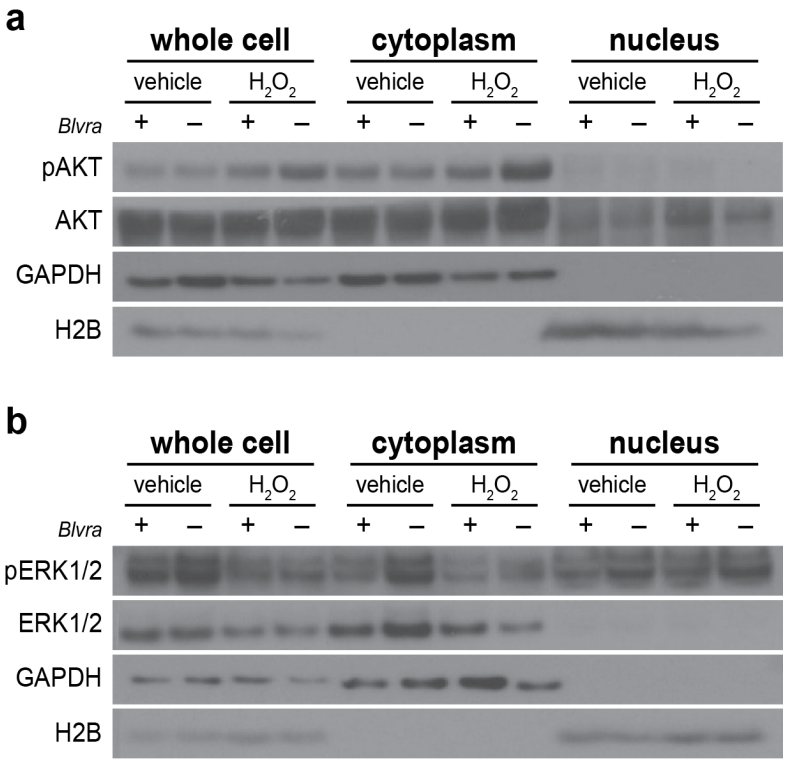

Figure 18. BVR$^{-/-}$ cells do not exhibit loss of AKT or MAPK signaling under oxidative stress.

a, Representative western blots for phosphoserine-473 AKT, total AKT, GAPDH, and Histone 2B of subcellular compartments of WT and BVR$^{-/-}$ MEFs treated with 200 μM H_2O_2 for 4 h. **b**, Representative western blots for phosphothreonine-202/phosphotyrosine-204 ERK1/2, total ERK1/2, GAPDH, and Histone 2B of subcellular compartments of WT and BVR$^{-/-}$ MEFs treated with 200 μM H_2O_2 for 4 h.

Although pyrogallol, menadione, and paraquat auto-oxidize to produce $O_2^{\bullet-}$, they are only crude stereotypes of pathologic or physiologic $O_2^{\bullet-}$. To determine if bilirubin scavenges $O_2^{\bullet-}$ *in vivo*, we treated WT and BVR$^{-/-}$ MEFs with rotenone and measured $O_2^{\bullet-}$ with the mitochondrial $O_2^{\bullet-}$ probe MitoSOX Red. Rotenone inhibits Complex I of the electron transport chain, thereby driving electron transfer to O_2 to form $O_2^{\bullet-}$ (OBERG, 1961).

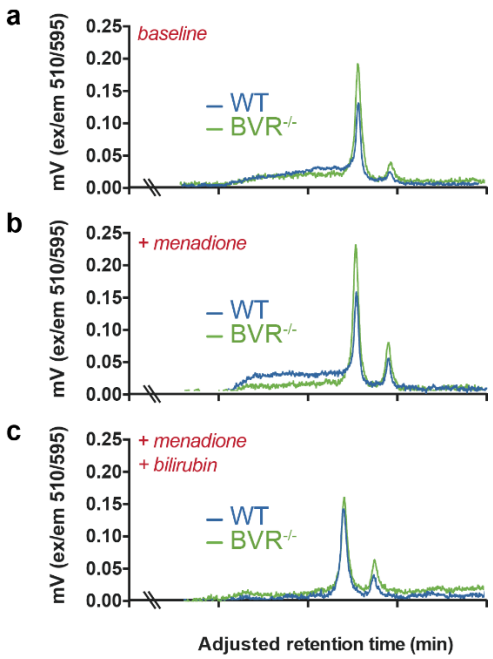

Figure 19. Superimposed time-adjusted DHE HPLC chromatograms from WT and BVR$^{-/-}$ MEFs.

a-c, Superimposed HPLC chromatograms of organic extracts from WT and BVR$^{-/-}$ MEFs loaded with DHE (*a*) at baseline or after treatment with (*b-c*) 25 μM menadione for 1 h. Cells treated with bilirubin in (*c*) were pre-treated with 500 nM bilirubin for 30 min just prior to menadione. Because elution times shifted over the time, samples traces were adjusted with respect to time in order to standardize elution of E+ and 2-OH-E+ between samples.

BVR$^{-/-}$ MEFs exhibit more than double the MitoSOX Red fluorescence of WT MEFs after exposure to rotenone (**Fig. 15g-h**) despite expressing similar levels of *Sod1, Sod2, Sod3* and respiratory chain complex proteins (**Fig. 22a-c**). These findings suggest that even if SODs are sufficient for scavenging basal $O_2^{\bullet-}$, bilirubin may be necessary during heavy mitochondrial activity or stress. Pre-treating both WT and BVR$^{-/-}$ MEFs with bilirubin reduces MitoSOX Red fluorescence (**Fig. 15g-h**), suggesting that even exogenous bilirubin can reach mitochondria to scavenge ROS. In the brain, mitochondrial $O_2^{\bullet-}$ is a major driver of neuronal death in instances like ischemic stroke (Chouchani et al., 2014;

Kontos et al., 1992). To determine whether bilirubin prevents mitochondrial stress and neuronal death in the brain, we stereotactically injected rotenone into the cerebellum of WT and BVR$^{-/-}$ mice. We injected vehicle into the contralateral hemisphere to control for surgical injury. BVR$^{-/-}$ mice exhibit substantially larger lesions after exposure to rotenone, suggesting that bilirubin may protect against mitochondrial oxidative stress in the brain (**Fig. 21b-d**).

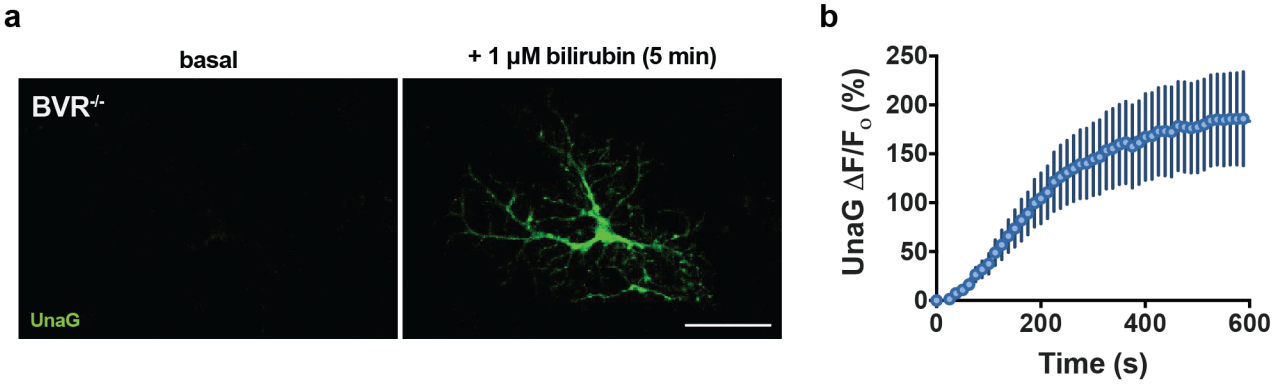

Figure 20. Treating cells with bilirubin extracellularly increases intracellular bilirubin.

a, Live-cell images of BVR$^{-/-}$ neurons co-expressing UnaG. *left*, baseline fluorescence of UnaG. *right*, UnaG fluorescence 5 min after application of 1 μM bilirubin. Scale bar = 50 μm. **b**, Average normalized UnaG fluorescence from individual DIV 14-18 primary cortical neurons over 5 min after treatment with extracellular bilirubin. After establishing baseline fluorescence for 10 s, neurons were treated with 1 μM bilirubin. n = 6 neurons.

Bilirubin scavenges $O_2^{\bullet-}$

To determine whether bilirubin directly scavenges $O_2^{\bullet-}$, we added one equivalent of bilirubin to $O_2^{\bullet-}$ in an aprotic solvent and monitored the spectroscopic signal of the unpaired electron on $O_2^{\bullet-}$ by electron paramagnetic resonance (EPR). At 100 K, $O_2^{\bullet-}$ alone exhibits its characteristic anisotropic EPR spectrum (Bagchi et al., 1989). Adding bilirubin immediately results in loss of EPR signal (**Fig. 23a**), suggesting that bilirubin scavenges the unpaired electron

on $O_2^{\bullet-}$. We assessed whether other endogenous heme metabolites, biliverdin and conjugated bilirubin (ditaurated bilirubin), can scavenge $O_2^{\bullet-}$. Using the spin trap 5,5-dimethyl-1-pyrroline N-oxide (DMPO) at 298 K, we observe that ditaurated bilirubin is almost as effective as bilirubin in scavenging $O_2^{\bullet-}$ (**Fig. 23b**). Biliverdin also scavenges $O_2^{\bullet-}$, but more slowly than bilirubin. In contrast, glutathione exhibits no effect even at 100-fold excess.

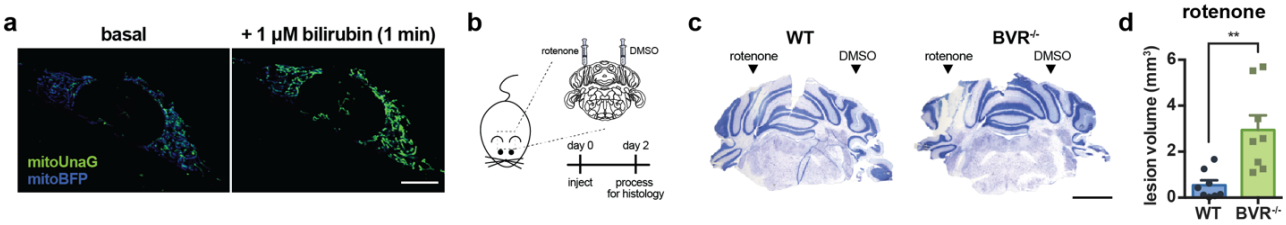

Figure 21. Bilirubin localizes to mitochondria and prevents mitochondrial stress.

a, Live-cell images of MEFs co-expressing mitochondrial-targeted UnaG (mitoUnaG) and mitochondrial-targeted blue fluorescent protein (mitoBFP). *left*, baseline fluorescence of mitoUnaG and mitoBFP. *right*, fluorescence 1 min after application of 1 μM bilirubin. Scale bar = 10 μm. **b**, Schematic illustrating localized *in vivo* rotenone cerebellar microinjections. **c**, Nissl stains of cerebellar sections from WT and BVR$^{-/-}$ mice 48 h after stereotactic injection of vehicle or 1 μg of rotenone. Lesions are outlined in orange. Scale bar = 2 mm. **d**, Lesion volumes in WT and BVR$^{-/-}$ mice from rotenone microinjections. Points represent individual mice. Mean ± SEM depicted. ** = $P < 0.01$ by two-tailed unpaired Student's t-test.

Mitochondrial Complexes II and III produce $O_2^{\bullet-}$ at membranous sites (Guo and Lemire, 2003; Husen and Solov'yov, 2016), compartments more accessible to bilirubin than SODs. Bilirubin's reactivity towards $O_2^{\bullet-}$ in aprotic solvents suggests that it may function as an important membranous $O_2^{\bullet-}$ scavenger. To test whether bilirubin can scavenge $O_2^{\bullet-}$ in cytosolic compartments as well, we assessed whether bilirubin can scavenge $O_2^{\bullet-}$ produced by xanthine oxidase in aqueous buffer. Bilirubin rapidly degrades when incubated with xanthine oxidase (**Fig. 23c**), but may be reacting with either $O_2^{\bullet-}$ or H_2O_2 since $O_2^{\bullet-}$ rapidly disproportionates to H_2O_2 in aqueous solvents. However, adding catalase to

remove H_2O_2 does not prevent bilirubin from degrading (**Fig. 23c**). Unlike catalase, excess SOD (which coverts $O_2^{\bullet-}$ into H_2O_2) prevents bilirubin from degrading, suggesting that bilirubin is not reacting secondarily with H_2O_2 but instead with $O_2^{\bullet-}$ directly. Similarly, incubating UnaG-bilirubin complexes with pyrogallol quenches UnaG fluorescence, whereas H_2O_2 has no effect (**Fig. 23d**). This again suggests that bilirubin reacts with $O_2^{\bullet-}$ but is inert towards H_2O_2, consistent with BVR$^{-/-}$ cells heightened vulnerability to $O_2^{\bullet-}$ over H_2O_2.

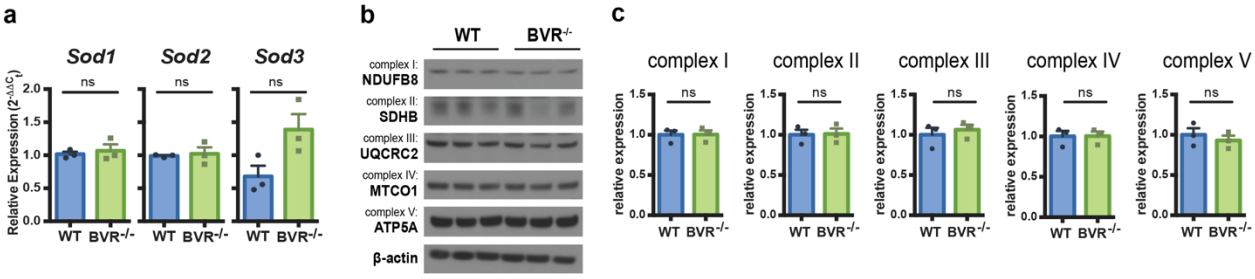

Figure 22. WT and BVR$^{-/-}$ mice exhibit similar expression of *Sod* enzymes and respiratory chain complex proteins.

a, Quantitative PCR analysis of *Sod1*, *Sod2*, and *Sod3* mRNA from WT and BVR$^{-/-}$ brains, normalized to β-actin. Points represent individual mice. Mean ± SEM depicted. ns = $P > 0.05$ by two-tailed unpaired Student's t-test. **b**, western blots for components of Complexes I-V of the mitochondrial electron transport chain and β-actin from WT and BVR$^{-/-}$ brains. **c**, Relative quantification of Complex I-V proteins in WT and BVR$^{-/-}$ brains. Points represent individual mice. Mean ± SEM depicted. ns = $P > 0.05$ by two-tailed unpaired Student's t-test.

To more fully understand how bilirubin reacts with $O_2^{\bullet-}$, we sought to better characterize the product and mechanism of the reaction. We find that the product elutes earlier than bilirubin on a reverse-phase column, indicating that it is likely more polar than bilirubin (**Fig. 23e**). The product also exhibits a red-shifted UV-visible spectrum with a local λ_{max} at 545 nm (**Fig. 23f**), which suggests expansion of bilirubin's conjugate π network. Formation of a red-shifted

electronic network could proceed through several mechanisms, the simplest being a single electron transfer (SET) from $O_2^{\bullet-}$ to bilirubin. SET reactions between $O_2^{\bullet-}$ and heterocyclic compounds, such as lucigenin (Legg and Hercules, 1969) and *N*-methylacridone (Rosenthal and Bercovici, 1973), often result in weak chemiluminescence. As with these heterocyclics, incubating $O_2^{\bullet-}$ with bilirubin results in chemiluminescence (**Fig. 23g**), suggesting that the two may react via a SET. However, the exact molecular identity of the product remains unclear and would require additional electrochemical and spectroscopic data.

While bilirubin appears to scavenge $O_2^{\bullet-}$, we wondered whether the reaction is rapid enough to be physiologically relevant. To determine the rate of the reaction, we employed a steady-state competitive kinetic analysis against *p*-nitro blue tetrazolium (**Fig. 23h**), an established $O_2^{\bullet-}$ scavenger (Bielski and Richter, 1977). We determined that bilirubin scavenges $O_2^{\bullet-}$ with a second-order rate constant of $(4.6 \pm 0.8) \times 10^5\ M^{-1}\ s^{-1}$, a rate similar to other physiologic rate constants like those of urease ($4.0 \times 10^5\ M^{-1}\ s^{-1}$) and chymotrypsin ($2.9 \times 10^5\ M^{-1}\ s^{-1}$) (Voet et al., 2016). Two abundant antioxidants in humans, glutathione and cysteine, exhibit little to no reactivity towards $O_2^{\bullet-}$ (**Table 1**). Bilirubin scavenges $O_2^{\bullet-}$ faster than biliverdin, highlighting an important evolutionary and functional distinction between the two metabolites (**Fig. 23h**). Although the second-order rate constant for the reaction between bilirubin and $O_2^{\bullet-}$ is larger than the other antioxidants we evaluated, $O_2^{\bullet-}$ also reacts with nitric oxide and tyrosine radicals at near-diffusion controlled rates ($k > 10^9\ M^{-1}\ s^{-1}$) (d'Alessandro et al., 2000; Huie and Padmaja, 1993). $O_2^{\bullet-}$ reacts with nitric oxide and tyrosine radicals to form

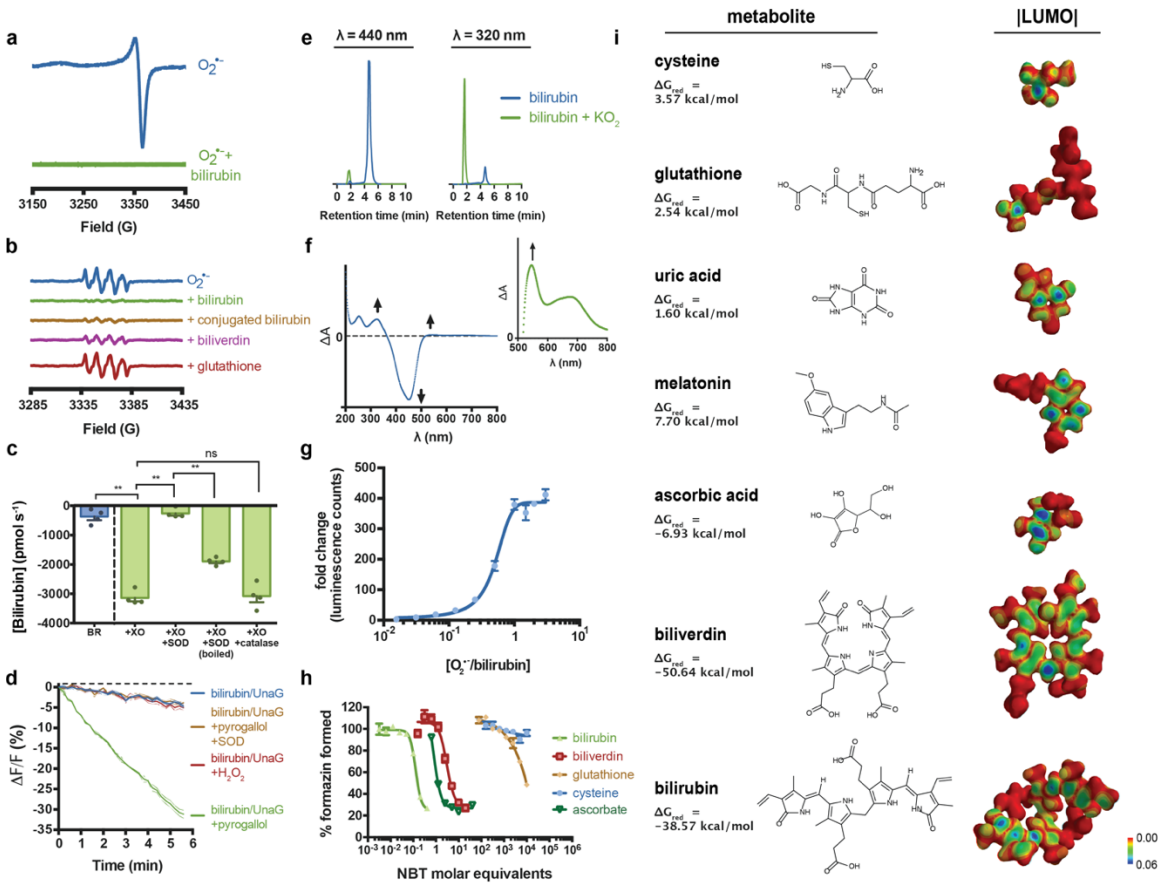

Figure 23. Bilirubin selectively scavenges $O_2^{\bullet-}$ at physiologically-relevant rates.

a, EPR spectrum of radicals generated by dissolution of KO_2 without (*blue*) and with (*green*) equimolar bilirubin in 0.2 M 18-crown-6 in DMSO at 100 K. **b**, EPR spectra of DMPO-spin adducts of radicals from solutions of KO_2 with or without 1 equivalent of bilirubin, bilirubin ditaurate, or biliverdin or 100 equivalents of glutathione at 298 K. **c**, Rate of change in bilirubin absorbance with xanthine/xanthine oxidase (XO) with or without excess 100 nM MnSOD or 1 μM catalase. Mean ± SEM depicted. n = 2 in triplicate. ** = $P < 0.01$ and ns = $P > 0.05$ by two-way ANOVA followed by a *post hoc* Tukey test. **d**, Normalized change in UnaG fluorescence from 1 μM bilirubin and 1 μM apoUnaG with either 1 mM H_2O_2 (*red*), 100 μM pyrogallol (*green*), or 100 μM pyrogallol and 100 nM MnSOD (*orange*). **e**, Representative HPLC chromatograms of bilirubin or bilirubin + KO_2 with the detector set to (*left*) 440 nm or (*right*) 320 nm. **f**, UV-visible difference spectrum of bilirubin subtracted from bilirubin + KO_2. **g**, Average fold change in chemiluminescence upon mixing 5 μM bilirubin with varying equivalents of KO_2. **h**, Average competitive kinetic inhibition curves for bilirubin, glutathione, cysteine, and ascorbic acid against *p*-nitro blue tetrazolium (NBT) and xanthine/xanthine oxidase-derived $O_2^{\bullet-}$. **i**, LUMO densities (|LUMO|) and change in Gibbs free energy (ΔG) for reducing cysteine, glutathione, uric acid, melatonin, ascorbic acid, biliverdin, and bilirubin, as calculated by the B3LYP functional and 6-31+G* diffuse basis set. Blue illustrates greater LUMO density, whereas red indicates lower density.

peroxynitrite and tyrosine hydroperoxides, respectively, both of which contribute to $O_2^{\bullet-}$ toxicity (Nagy et al., 2009; Winterbourn et al., 2004). It is unlikely that bilirubin outcompetes nitric oxide or tyrosine radicals for $O_2^{\bullet-}$, which suggests that bilirubin instead prevents other modes of $O_2^{\bullet-}$ toxicity.

molecule	$k_{O2\cdot-}$ (M^{-1} s^{-1}) *experimental*	$k_{O2\cdot-}$ (M^{-1} s^{-1}) *literature*
bilirubin	$(4.6 \pm 0.84) \cdot 10^5$	
biliverdin	$(2.0 \pm 0.47) \cdot 10^4$	
glutathione	15.0 ± 0.14	220 ± 10 [a]
cysteine	n.d.	15 ± 2.0 [b]
ascorbate	$(8.2 \pm 0.15) \cdot 10^4$	$(2.8 \pm 0.3) \cdot 10^4$ [d]

Table 1. Second order rate constants between $O_2^{\bullet-}$ and various small molecules.

Experimental and literature rate constants for the reaction between $O_2^{\bullet-}$ and bilirubin, glutathione, cysteine, and ascorbate. n.d. = not determined. [a] Jones, C. M., *et al. Free Radic. Biol. Med* **32,** 982–990 (2002); [b] Bielski, B. H. & Shiue, G. G. *Ciba Found. Symp.* 43–56 (1978); [c] Sawyer, D. T., *et al. J. Am. Chem. Soc.* **104,** 6273–6278 (1982)

To identify kinetic and thermodynamic factors that influence bilirubin reactivity towards $O_2^{\bullet-}$, we calculated and compared the electronic structures of bilirubin, biliverdin, cysteine, glutathione, uric acid, melatonin, and ascorbic acid by density functional theory (DFT) (Becke, 1993; Hohenberg and Kohn, 1964; Kohn and Sham, 1965; Stephens et al., 1994). DFT calculations predict that bilirubin's lowest unoccupied orbital (LUMO) is extensively delocalized through

several bonds across the metabolite, which may impart unusual electron-accepting properties and kinetic reactivity towards $O_2^{\bullet-}$ (**Fig. 23i**). Biliverdin also exhibits a delocalized LUMO similar to bilirubin, but one that is more densely concentrated at a single carbon (the α-meso carbon bridge). A more localized electron density could slow SET reactions, and may explain the different reactivities of biliverdin and bilirubin to towards $O_2^{\bullet-}$. In contrast to the heme metabolites, cysteine, glutathione, uric acid, melatonin, and ascorbic acid exhibit much more densely localized LUMOs, rendering them less effective electron-acceptors. DFT calculations also predict that reducing bilirubin and biliverdin is exergonic. In clear contrast, the Gibbs free energy requirements for reducing cysteine, glutathione, uric acid, and melatonin are thermodynamically unfavorable. Reducing ascorbic acid is approximately 32 kcal/mol less thermodynamically favorable than reducing bilirubin.

NMDA receptors signal via $O_2^{\bullet-}$, and bilirubin prevents NMDA excitotoxicity by scavenging $O_2^{\bullet-}$

Although bilirubin is neurotoxic at high micromolar concentrations, BVR is highly expressed in the brain compared to other tissues (**Fig. 14a-b**) and bilirubin is enriched in neurons (**Fig. 11m-n**). As with MEFs, loss of endogenous bilirubin renders neurons vulnerable to oxidative death. $BVR^{-/-}$ neurons are also hypersensitive to $O_2^{\bullet-}$ over H_2O_2 (**Fig. 24a**). *Ex vivo*, DHE fluorescence suggests that $BVR^{-/-}$ neurons similarly cannot clear ROS as efficiently as WT when challenged with pyrogallol (**Fig. 24b-d**).

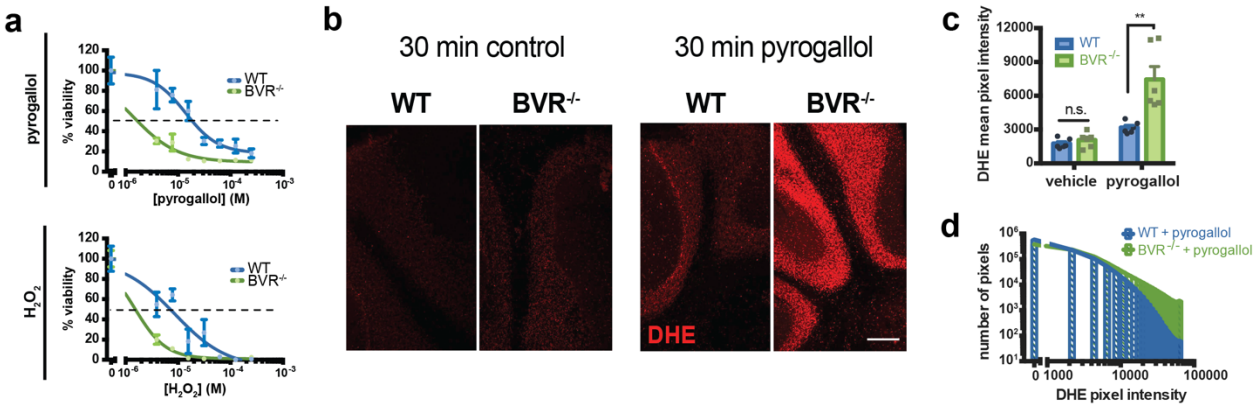

Figure 24. BVR$^{-/-}$ neurons are hypersensitive to oxidative stress.

a, WT and BVR$^{-/-}$ neuronal viability after 8 h exposure to varying concentrations of (*above*) pyrogallol and (*below*) H_2O_2. Mean ± SEM depicted. $n = 2$ (pyrogallol) and $n = 4$ (H_2O_2) in triplicate. **b**, Confocal images of WT and BVR$^{-/-}$ brains that were treated *ex vivo* with 100 μM pyrogallol for 30 min, after which total ROS was visualized by loading cells with 10 μM dihydroethidium (DHE) for 45 min. Scale bar = 200 μm. **c-d**, Quantification and histograms of DHE pixel intensity from WT and BVR$^{-/-}$ *ex vivo* brain slices treated with pyrogallol. Points represent independent cerebellar slices. Mean ± SEM depicted. ** = $P < 0.01$ by two-way ANOVA followed by a *post hoc* Tukey test.

In the brain, $O_2^{\bullet-}$ is an important neuromodulator. Activated glutamatergic NMDA receptors (NMDARs) stimulate NADPH oxidase to generate $O_2^{\bullet-}$ (Brennan et al., 2009; Lafon-Cazal et al., 1993), which functions as a second messenger in long-term potentiation and neuronal redox processes (Gao et al., 2007; Heusler and Boehmer, 2004; Klann, 1998; Wang et al., 1996). BVR$^{-/-}$ mice exhibit exaggerated locomotor activity when injected with NMDA or MK-801 (an NMDAR agonist and antagonist, respectively) (**Fig. 25a-c**), indicating that BVR$^{-/-}$ mice exhibit aberrant NMDAR function. Accordingly, we explored whether bilirubin influences NMDAR redox signaling.

Gauged by real-time DHE fluorescence, we observe that treating neurons with NMDA stimulates $O_2^{\bullet-}$ signaling, consistent with previous reports (**Fig. 25d**) (Bindokas et al., 1996; Brennan et al., 2009; Lafon-Cazal et al., 1993). Notably,

activating glutamatergic AMPA or kainate receptors does not lead to $O_2^{\bullet-}$ signaling in the presence of excess Mg^{2+} or APV, both of which inhibit NMDARs. To determine whether endogenous bilirubin scavenges NMDAR-associated $O_2^{\bullet-}$, we treated WT neurons expressing UnaG with NMDA and monitored changes in UnaG fluorescence. As with pyrogallol *in vitro* (**Fig. 23e**), neuronal UnaG fluorescence decays after treatment with NMDA on the same time scale that DHE fluorescence increases (**Fig. 25e-f**). Applying the spin trap DMPO to the bath beforehand preserves UnaG fluorescence, suggesting that changes in UnaG are due to NMDAR-evoked $O_2^{\bullet-}$. Treating neurons with (*S*)-AMPA or kainate with excess Mg^{2+} or APV also does not alter UnaG fluorescence, presumably because AMPA and kainate receptors do not trigger $O_2^{\bullet-}$ production.

Previous studies of whether NMDARs initiate $O_2^{\bullet-}$ signaling relied on experiments that measured DHE fluorescence rather than formation of 2-OH-E^+ (Bindokas et al., 1996; Brennan et al., 2009; Reyes et al., 2012), but DHE can non-specifically react with diverse oxidants to form different products with similar fluorescence spectra (Zhao et al., 2003; 2005). To establish whether NMDARs drive $O_2^{\bullet-}$ signaling, we measured neural 2-OH-E^+ by HPLC before and after treating brain slices *ex vivo* with NMDA. Treating WT slices with NMDA leads to significant 2-OH-E^+ formation, indicating that NMDARs indeed signal in part through $O_2^{\bullet-}$ (**Fig. 25g-i**). By contrast, $BVR^{-/-}$ slices accumulate almost two times more 2-OH-E^+ than WT slices, suggesting that neural bilirubin scavenges NMDAR-associated $O_2^{\bullet-}$ (**Fig. 25g-i**).

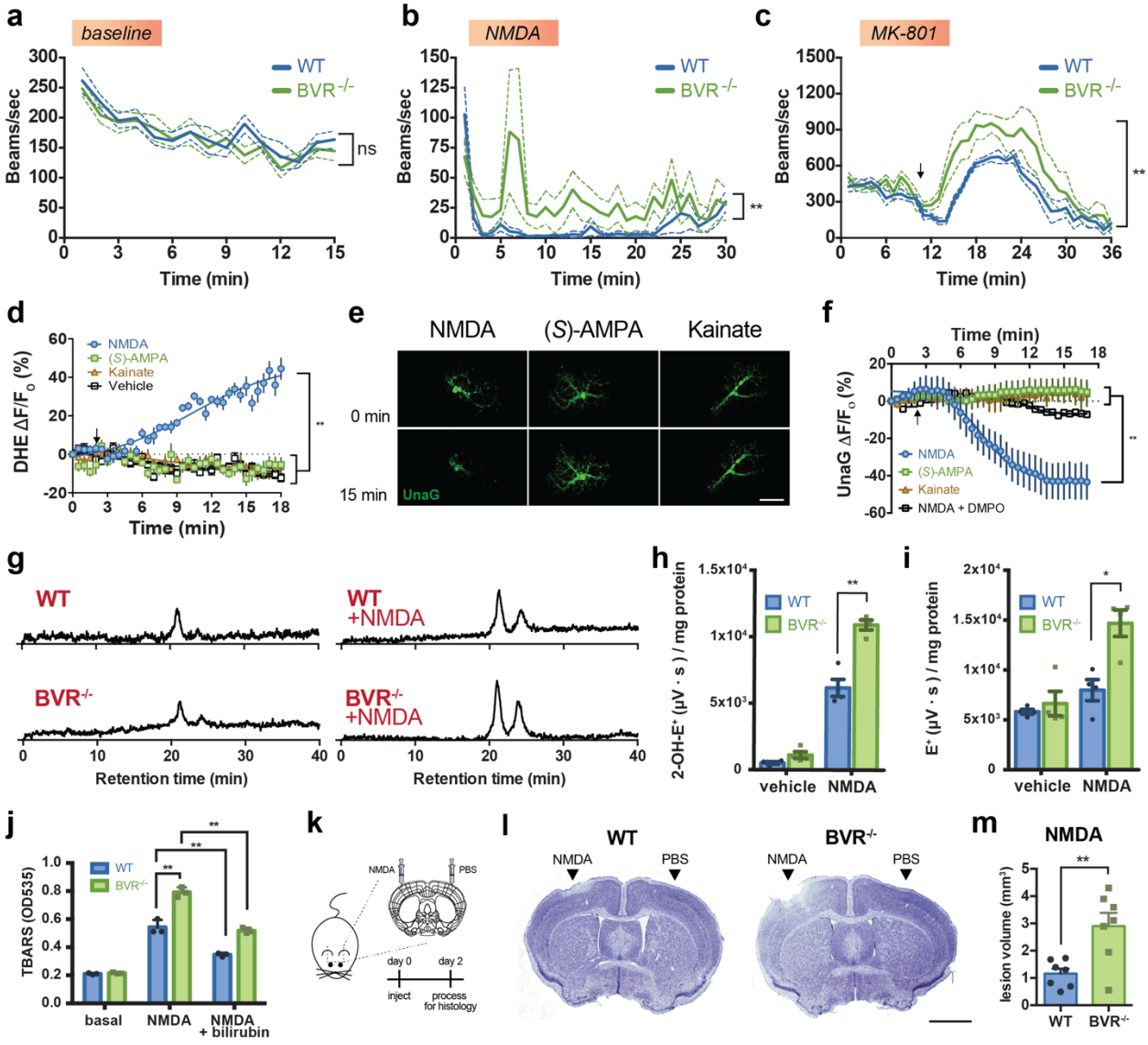

Figure 25. NMDA receptors signal via $O_2^{\bullet-}$, and bilirubin prevents NMDA excitotoxicity by scavenging $O_2^{\bullet-}$.

a-c, WT and BVR$^{-/-}$ male mouse open field locomotor activity over time at (*a*) baseline or after treatment with either (*b*) NMDA (100 mg/kg, i.p.) at 0 min or (*c*) MK-801 (0.3 mg/kg, i.p.). at 10 min (arrow). Mean ± SEM depicted. n = 5 WT and 6 BVR$^{-/-}$ mice (baseline and NMDA) and 9 WT and 5 BVR$^{-/-}$ mice (MK-801). ** = $P < 0.01$ and ns = $P > 0.05$ by two-tailed unpaired Student's t-test. **d**, Normalized DHE fluorescence from individual DIV 14-18 primary cortical neurons over time. Neurons were treated (arrow) with 100 μM NMDA + 10 μM glycine, 100 μM (*S*)-AMPA, or 100 μM kainate. Neurons treated with (*S*)-AMPA or kainate were pre-equilibrated with 2 mM $MgCl_2$ or 50 μM APV. Points are means ± SEM of n = 6 neurons. Mean ± SEM depicted. ** = $P <$ 0.01 by one-way ANOVA followed by a *post hoc* Tukey test. **e-f**, Live images (*e*) and traces (*f*) of DIV 14-18 primary cortical neurons expressing UnaG over 15 min after treatment with 100 μM NMDA + 10 μM glycine, 50 μM (*S*)-AMPA, or 50 μM kainate. Scale bar = 25 μm. Neurons treated with (*S*)-AMPA or kainate were pre-equilibrated with 2 mM $MgCl_2$ or 50 μM APV. Neurons treated with DMPO were pre-equilibrated with 10 mM DMPO 15 min prior to imaging. Points are means ± SEM of n = 5 (NMDA), 3 (*S*-AMPA), and 3 (kainate) neurons. ** = $P < 0.01$ by one-way ANOVA

followed by a *post hoc* Tukey test. **g**, Representative normalized HPLC chromatograms of organic extracts from WT and $BVR^{-/-}$ *ex vivo* brain slices loaded with DHE at baseline or after treatment with 100 μM NMDA + 10 μM glycine for 30 min. **h-i,** Relative quantification of E^+ and 2-OH-E^+ extracted from WT and $BVR^{-/-}$ brain slices by HPLC at baseline or after treatment with NMDA/glycine. Points represent average of slices from individual mice. Mean ± SEM depicted. * = P < 0.05 and ** = P < 0.01 by two-way ANOVA followed by a *post hoc* Tukey test. **j**, Average thiobarbituric acid-reactive substances (TBARS) in WT and $BVR^{-/-}$ neurons 24 h after treatment with vehicle or 100 μM NMDA + 10 μM glycine for 20 min. Neurons treated with bilirubin were pre-treated with 50 nM bilirubin for 1 h prior to glycine/NMDA. Points represent independent data points. Mean ± SEM depicted. * = $P < 0.05$ and ** = $P < 0.01$ by two-way ANOVA followed by a *post hoc* Tukey test. **k**, Schematic illustrating localized *in vivo* NMDA cortical microinjections. **l**, Nissl stains of coronal sections from WT and $BVR^{-/-}$ mice 48 h after stereotactic injection of vehicle or 20 nmoles of NMDA. Scale bar = 2 mm. **m**, Lesion volumes in WT and $BVR^{-/-}$ mice from NMDA microinjections. Points represent individual mice. Mean ± SEM depicted. ** = $P < 0.01$ by two-tailed unpaired Student's t-test.

Because NMDARs signal in part through $O_2^{\bullet-}$, pathologic NMDAR activity can also lead to uncontrolled lipid peroxidation and neuronal death (Reyes et al., 2012). Persistent NMDAR activity, or excitotoxicity, is thought to mediate several neurodegenerative diseases, including Alzheimer's, Parkinson's, and Huntington's diseases (DEXTER et al., 1994; Ferrante et al., 1997; Kellogg and Fridovich, 1975; Subbarao et al., 1990). As expected, treating WT and $BVR^{-/-}$ neurons with high concentrations of NMDA results in accumulation of malondialdehyde, indicative of lipid peroxidation (**Fig. 25j**). However, $BVR^{-/-}$ neurons exhibit greater lipid peroxidation than WT neurons, suggesting that endogenous bilirubin protects neurons from excitotoxic death. Pre-treating both WT and $BVR^{-/-}$ neurons with bilirubin reduces peroxidation (**Fig. 25j**). To establish whether bilirubin prevents NMDA-driven excitotoxicity in the brain, we stereotactically injected NMDA into the cortex of WT and $BVR^{-/-}$ mice. As with rotenone, we injected saline into the contralateral hemisphere to control for surgical injury (**Fig. 25k**). $BVR^{-/-}$ mice exhibit substantially larger lesions after

exposure to NMDA, suggesting that endogenous bilirubin exerts neuroprotection in part by preventing excitotoxicity (**Fig. 25l-m**).

Discussion

$O_2^{\bullet-}$ is a key messenger in mammals, but its redox activity involves chemical specificity. The present study establishes a prominent role for endogenous bilirubin as a physiologic $O_2^{\bullet-}$ scavenger and establishes an activity specific to bilirubin over other major antioxidants. We also find that bilirubin is substantially more reactive towards $O_2^{\bullet-}$ than biliverdin. Bilirubin's unique antioxidant profile may also explain why it is a major physiologic antioxidant despite being 10,000-fold lower in concentration than other antioxidants. Intriguingly, bilirubin levels inversely correlate with disease severity in several disorders in which $O_2^{\bullet-}$ scavenging is compromised, including Parkinson's (Hatano et al., 2016; Moccia et al., 2015; Scigliano et al., 1997) and coronary artery diseases (BREIMER et al., 1995; Levinson, 1997).

Bilirubin's distinct redox activity may mediate unique redox signaling that underlies larger cellular processes. BVR appears to influence innate immunity and liver physiology (Bisht et al., 2019; Hinds et al., 2016). By selectively ablating *Blvra* in myeloid cells, Bisht and colleagues recently discovered that BVR modulates C5aR1 expression, thereby regulating macrophage chemotaxis. Just prior, Hinds and colleagues reported that eliminating BVR in hepatocytes leads to hepatic steatosis. Bilirubin could signal in both processes by scavenging $O_2^{\bullet-}$, which regulates both macrophage chemotaxis and hepatic steatosis (Browning

and Horton, 2004; PETRONE et al., 1980). Recently, Chen and colleagues independently generated a mouse that also globally lacks BVR (Chen et al., 2018). By rigorously examining plasma lipids and peroxiredoxin-2, Chen et al. observed that deleting BVR leads to endogenous oxidative stress even in naïve mice. Both of our studies conclude that bilirubin physiologically exerts potent redox activity despite being significantly less abundant than other antioxidants. Together with the redox mechanisms identified in the present study, these studies may inform future work that discovers redox mechanisms specific to bilirubin.

Previous studies that explored a physiologic connection between bilirubin and $O_2^{\bullet-}$ proposed that bilirubin and related tetrapyrroles attenuate $O_2^{\bullet-}$ signaling, but act indirectly by inhibiting NADPH oxidase (IWANAGA et al., 1987; Kwak et al., 1991; NAKAMURA et al., 1987). Other studies have observed that moderately hyperbilirubinemic mice exhibit less nitrositive/oxidative stress, suggesting that bilirubin acts by inhibiting NADPH oxidase (Stec et al., 2013; Vera et al., 2009). These studies support our findings that bilirubin is a physiologic antioxidant, but also provide intriguing evidence that bilirubin functions indirectly. However, these studies monitored the effect of bilirubin on NADPH oxidase activity by measuring $O_2^{\bullet-}$ and therefore do not disambiguate whether bilirubin acts by inhibiting NADPH oxidase, directly scavenging $O_2^{\bullet-}$ as identified here, or a mix of both.

Our findings also suggest that diverse metabolic pathways are linked to neural activity. Although neural activity triggers changes in oxidative metabolism and glycolysis to adapt to energy demands, less is known about the influence of

neural activity on metabolic processes outside of cellular respiration. We propose that heme metabolism influences NMDAR redox signaling, and speculate that other metabolites may also shape neural function in yet unidentified ways.

Materials and methods

Experimental Model and Subject Details

Mice

Animal care and use

All experiments were performed in accordance with protocols approved by the Animal Care and Use Committee at the Johns Hopkins University School of Medicine.

Generation of BVR knock-out ($BVR^{-/-}$) mice

$BVR^{-/-}$ mice were generated at Ozgene (Australia) on a C57BL/6J background. To ensure loss of bilirubin biosynthesis, exon 3 of *Blvra* was flanked by two LoxP sequences for deletion via the *Cre* recombinase. $BVR^{-/-}$ mice were then backcrossed to wild-type C57BL/6J mice for four or more generations before these studies. Age-matched wild-type C57BL/6J mice were used as controls.

Cell culture

MEFs

To isolate WT and $BVR^{-/-}$ MEFs, embryonic day 14.5 (E14.5) embryos were obtained from timed $BVR^{+/-}$ matings. The pups were decapitated and eviscerated,

after which the remaining portion was trypsinized and sheared. Isolated MEFs were plated in 2 wells of a 6-well plate and cultured overnight in DMEM (Gibco) supplemented with 10% FBS, 100 U/mL penicillin and streptomycin, and 2 mM glutamine at 37°C with 5% CO_2. MEFs were then expanded to 6-well plates and transiently transfected with SV40T antigen (Addgene) and maintained until stably proliferative. DNA was isolated from the heads of the pups and genotyped to confirm the genotype of the corresponding MEF cell line. Data for WT and $BVR^{-/-}$ cells were drawn from experiments on at least two independent cell lines of each genotype.

Primary neurons

To isolate WT and $BVR^{-/-}$ neurons, cortices of embryonic day 14.5 (E14.5) embryos were isolated and washed with HBSS. Tissue was then incubated with 0.25% trypsin in HBSS for 18 min at 37°C in a conical tube, after which trypsin was inactivated with the addition of FBS. Tissue were then pelleted at 2000*g* for 5 min at 25°C, after which the supernatant trypsin/FBS was aspirated off. Tissue were then rinsed twice with HBSS, resuspended in HBSS, and then gently triturated through a fire-polished glass pipette to promote additional dissociation. Tissue was then filtered through a 70 µm nylon cell strainer to remove debris. The dissociated cells were pelleted at 2000*g* for 5 min at 25°C and then resuspended in neuronal culture media (composed of Neurobasal (Gibco) supplemented with 2% B-27 supplement and 2 mM glutamine). Cells were filtered once more through a 70 µm nylon cell strainer. Dissociated cells were

then plated onto rinsed, poly-D-lysine-coated dishes. Four days later, the conditioned media was supplemented with fresh neuronal culture media. The day before dissections, plates were prepared and coated in 0.25 mg/mL poly-D-lysine overnight at 37°C. Just prior to plating, plates were rinsed three times with sterile water and once with neuronal culture media.

Method Details

Materials and preparation

Solvents and compounds were obtained as follows:

potassium superoxide (KO_2) (Sigma), dimethyl sulfoxide (DMSO) (Sigma), 18-crown-6 (Sigma), bilirubin IXα (Frontier Scientific), biliverdin IXα (Sigma), bilirubin ditaurate (Lee Biosciences), hemin (Frontier Scientific), pyrogallol (Sigma), paraquat (Santa Cruz Biotech), menadione (Sigma), hydrogen peroxide (H_2O_2) (Sigma), 4-hydroxynonenal (4-HNE) (Cayman Chemical), methylthiazoletetrazolium (MTT) (Sigma), rotenone (Sigma), dihydroethidium (DHE) (Thermo Fisher Scientific), MitoSOX Red (Thermo Fisher Scientific), Hoechst 33258 (Abcam), *p*-nitro blue tetrazolium (Sigma), 5,5-dimethyl-1-pyrroline N-oxide (DMPO) (Cayman Chemical), L-glutathione (Sigma), L-cysteine (Sigma), L-ascorbate (Sigma), (*S*)-α-amino-3-hydroxy-5-methyl-4-isoxazolepropionic acid (*S*-AMPA) (Tocris Bioscience), kainic acid (Tocris Bioscience), N-Methyl-D-aspartic acid (NMDA) (Sigma), (+)-MK-801 (Sigma), and glycine (Sigma)

Material preparation:

Bilirubin is highly susceptible to oxidation and photolysis. Accordingly, bilirubin was freshly prepared in DMSO immediately prior to each experiment and then maintained in the dark. $O_2^{\bullet-}$ was freshly prepared by dissolving finely ground KO_2 in new 0.2 M 18-crown-6 in DMSO. KO_2 was prepared and maintained in a glove-bag under N_2. Glutathione, cysteine, and ascorbate were all prepared freshly before experimentation. Both bilirubin and KO_2 stock solutions were calibrated by UV-light spectroscopy. All other compounds were prepared as 100 µl – 1,000 µl aliquots and stored at -20°C before thawing at 4°C. Freeze/thaw cycles were avoided whenever possible.

Plasmids/cDNA, cloning, and lentivirus

Plasmids/cDNA

cDNA encoding UnaG was a gift from Atsushi Miyawaki, PhD (RIKEN, Japan). cDNA encoding mitochondrial-targeted UnaG was a gift from Jong-Seok Park, PhD and Hyun-Woo Rhee, PhD (Ulsan National Institute of Science and Technology, South Korea). cDNA encoding IRFP was a gift from Vladislav Verkhusha (Addgene plasmid #31857). psPAX2 and pMD2.G were gifts from Didier Trono (Addgene plasmids #12260 and #12259, respectively).

Lentivirus

Lentiviruses were generated as previously described with a few modifications (Jenkins et al., 2013). Briefly, cDNA encoding BVR and GFP separated by a self-

cleaving 2A peptide was cloned into pLenti6 and transfected HEK293 cells with psPAX2 and pMD2.G. Virus was harvested from the media and collected by centrifugation at 100,000*g* for 2 h. $BVR^{-/-}$ MEFs were infected with lentivirus in the presence of 8 μg/ml Polybrene overnight. After 48 h, cells were sorted by GFP fluorescence using fluorescence-activated cell sorting (FACS).

Spectroscopic analyses

Electron paramagnetic resonance (EPR) spectroscopy

EPR spectra were recorded with a Bruker EMXmicro spectrometer equipped with a ER4119HS resonator, and ER4141VT temperature control unit (Bruker Biospin, Billerica, MA). For analysis of naked radicals, the spectrophotometer was set at the following parameters unless otherwise stated: temperature, 100 K; sweep width, 300 G; modulation amplitude, 1 G; modulation frequency, 100 KHz; microwave power, 10 mW. For analysis of spin-trapped radicals (100 μM DMPO), the spectrophotometer was set at the following parameters unless otherwise stated: temperature, 298 K; sweep width, 150 G; modulation amplitude, 1 G; modulation frequency, 100 KHz; microwave power, 10 mW.

UV-visible spectroscopy

UV-visible spectra were recorded from 300 to 750 nm in quartz cuvettes with a Beckman Coulter DU 600 spectrophotometer.

Chemiluminescence spectroscopy

Chemiluminescence measurements were obtained with a Turner Designs 20/20 luminometer without filters. Reactions were initiated by adding various equivalents of KO_2 to a fixed quantity of bilirubin. Chemiluminescence was quantified by integrating total counts over 10 seconds. Any chemiluminescence from dilution of KO_2 or bilirubin was subtracted as background.

Kinetic analyses

To determine second order rate constants of reactions with $O_2^{\bullet-}$, each reactant was individually mixed with 50 µM *p*-nitro blue tetrazolium (NBT), an established $O_2^{\bullet-}$ scavenger with a second order rate constant of k_{NBT} = (5.94 ± 0.5) x 10^4 M^{-1} s^{-1} (Bielski and Richter, 1977). The reactions were initiated by adding xanthine/xanthine oxidase as a source of $O_2^{\bullet-}$. The ultimate reactions conditions were as follows: 0.1 M $Na_4P_2O_7$, 100 nM deferoxamine (Sigma), 100 µM xanthine (Sigma), 10 mU xanthine oxidase (Sigma) at pH 8.3. The reaction between $O_2^{\bullet-}$ and NBT was monitored spectrophotometrically at 560 nm. The second order rate constants of each reactant was determined as a steady-state approximation by evaluating the reaction when $r_{NBT} = r_{reactant} \equiv k_{NBT}[NBT][O_2^{\bullet-}] = k_{reacant}[reactant][O_2^{\bullet-}]$. Therefore, $k_{reacant} = k_{NBT}[NBT]/[reactant]$.

Xanthine/xanthine oxidase-derived $O_2^{\bullet-}$

To determine rate at which bilirubin reacts with xanthine/xanthine oxidase-derived $O_2^{\bullet-}$, 5 µM bilirubin was incubated with 100 µM xanthine and 100 nM desferrioxamine and various amounts of xanthine oxidase in 0.1 M sodium

pyrophosphate at pH 8.5 at 25°C. Reactions were sometimes incubated with 100 nM MnSOD, 100 nM boiled MnSOD, or 1 μM catalase. Reaction was monitored and measured as a change in absorbance at 442 nm.

Quantum mechanical calculations

Density Field Theory calculations were performed and modeled with Spartan 16 (Wavefunction). Full geometry optimizations and frequency calculations were carried out with DFT-Hartree Fock hybrid B3LYP theory with the 6-31+G* basis set. Energies were calculated at ground state in the gas phase at 298 K.

Western blotting

For western blot analysis, tissues were dounce homogenized at 4°C in lysis buffer (pH 7.4 solution of 50 mM Tris-HCl, 150 mM NaCl, 0.1% SDS, 0.5% sodium deoxycholate, and 1% Triton X-100) supplemented with protease inhibitors (Sigma). Lysates were then pulse sonicated and centrifuged at 16,000*g* for 15 min at 4°C. Fifteen micrograms of cleared lysate were run on a 4-12% polyacrylamide Bis-Tris gradient gel in running buffer (pH 7.3 solution of 50 mM MES, 50 mM Tris Base, 0.1% SDS, 1 mM EDTA) and then transferred to a PVDF membrane. Membranes were blocked with 5% milk in TBS-T (pH 7.6 solution of 16 mM Tris-HCl, 140 mM NaCl, 0.1% Tween-20) and incubated with primary antibodies in 3% bovine serum albumin (BSA) (w/v) overnight at 4°C. The following day, membranes were washed with TBS-T, and then incubated with secondary antibodies in 3% BSA for 1 h at 25°C. The following primary antibodies

were used: rabbit anti-BVR (Abcam ab180208; 1:1,000), rabbit anti-HO-2 (generated as previously described (Zakhary et al., 1996); 1:1,000), mouse anti-total OXPHOS cocktail (Abcam ab110413; 1:5,000), mouse anti-pS473 AKT (Cell Signaling 587F11; 1:1000), rabbit anti-AKT (Cell Signaling 11E7; 1:1000), rabbit anti-pERK (Cell Signaling 9101; 1:1000), rabbit anti-tERK (Cell Signaling 9102; 1:1000), and mouse anti-β-actin (Santa Cruz Biotech sc-47778 HRP; 1:10,000). The following secondary antibodies were used: sheep anti-mouse IgG (GE Healthcare NA931; 1:10,000), and donkey anti-rabbit IgG (GE Healthcare NA934; 1:10,000)

RNA isolation, reverse transcriptase PCR (RT-PCR), and quantitative-PCR (q-PCR)

RNA isolation and qPCR were performed as previously described (Paul et al., 2014). In brief, total cellular or tissue RNA was extracted using the RNeasy Plus Universal Kit (Qiagen) per the manufacturer's instructions. RT-PCR was performed with the SuperScript III One-Step RT-PCR System (Invitrogen), whereas q-PCR was performed with the TaqMan RNA-to-C_t 1-Step Kit (Life Technologies).

Brain slice preparations

Ex vivo slices were prepared as described (Wang and Kass, 1997). In brief, brains from WT and $BVR^{-/-}$ mice were sectioned in 300 µm intervals with a vibratome in the sagittal plane. Slices were cut in ice-cold *sectioning* artificial cerebrospinal fluid (S-aCSF) (pH 7.4 solution of 126 mM NaCl, 3 mM KCl, 1.4 mM NaH_2PO_4,

10 mM $MgSO_4$, 0.5 mM $CaCl_2$, 26 mM $NaHCO_3$ and 10 mM glucose), equilibrated with 95% O_2 and 5% CO_2. Sections were equilibrated in room temperature *experimental* aCSF (E-aCSF) (pH 7.4 solution of 126 mM NaCl, 3 mM KCl, 1.4 mM NaH_2PO_4, 0 mM $MgSO_4$, 1.4 mM $CaCl_2$, 26 mM $NaHCO_3$ and 4 mM glucose) for 1 h before assaying.

High pressure liquid chromatography (HPLC)

Bile and plasma heme metabolites

Bile and plasma bilirubin, biliverdin, and heme were separated by HPLC with an analytical LC-18 column, 250 × 4.6 mm (Xterra, Waters Corporation) with the following mobile phases: 0.1 M ammonium acetate in 60% methanol / 40% water (v/v) (pH 5.2) (Solvent A) and 100% methanol (Solvent B) at 1 mL/min. Metabolites were eluted as follows: 0 to 14 min: linear gradient from 100% A to 100% B; 14 to 19 min: linear gradient from 100% A to 100% B; 19-24 min: isocratic elution at 100% A. The metabolites were detected by measuring absorbance at 405 nm. The bilirubin standard exhibited a retention time of approximately 14-15 min, whereas biliverdin and heme standards exhibited retention times of 10-11 and 17-18 min, respectively.

DHE, E^+, and 2-OH-E^+

DHE, E^+, and 2-OH-E^+ were extracted and analyzed by HPLC as previously established with a few modifications (Zhao et al., 2003; 2005). To extract intracellular DHE, E^+, and 2-OH-E^+, cells were lysed in lysis buffer (pH 7.4

solution of 50 mM Tris-HCl, 150 mM NaCl, 0.1% SDS, 0.5% sodium deoxycholate, and 1% Triton X-100) supplemented with protease inhibitors (Sigma), mixed with 1 equivalent of 1-butanol, vortexed for 1 min, and then centrifuged at 16,000*g* for 15 min at 4°C. The organic phase was separated and dried under nitrogen gas. Treatments and extractions were performed under dim light to minimize photooxidation of DHE (Zielonka et al., 2006). DHE, E^+, and 2-OH-E^+ were separated by HPLC with an analytical LC-18 column, 150 × 3.9 mm (Xterra, Waters Corporation) with the following mobile phases: 10% acetonitrile in in 0.1% trifluoroacetic acid (Solvent A) and 70% acetonitrile in in 0.1% trifluoroacetic acid (Solvent B) at 1 mL/min. The samples were eluted with a linear gradient from 100% A / 0% B to 80% A / 20% B from 0 to 40 min. DHE, E^+, and 2-OH-E^+ were detected with a fluorescence detector with excitation and emission at 510 and 595 nm, respectively.

a. MEFs: MEFs were treated with 25 µM menadione for 1 h, washed with HBSS, loaded with 25 µM dihydroethidium (DHE) for 45 min, and then rinsed twice more in HBSS before lysis.
b. Brain slices: Slices were loaded with 25 µM dihydroethidium (DHE) for 30 min, washed twice with E-aCSF, and then treated in separate chambers with vehicle or 100 µM NMDA + 10 µM glycine for 30 min. Brain slices were assayed at room temperature in E-aCSF continuously bubbled with 95% O_2 and 5% CO_2.

Cell viability assays

Clonogenic assays

Clonogenic assays were performed as previously described (Weyemi et al., 2015). In brief, equivalent numbers of WT and $BVR^{-/-}$ MEFs were plated on 35 mm dishes. The cells were treated the following day with an oxidant and then fed fresh media the subsequent day. Six days later, the cells were fixed with 100% methanol for 10 min, stained with 1% methylene blue, and then destained for 5 min with a solution of 40% methanol / 10% acetic acid / 50% water (v/v/v). Colonies were quantified under a dissection microscope.

Methylthiazoletetrazolium (MTT) assays

MTT assays were performed as previously described (Baranano et al., 2002). In brief, MEFs were plated at a density of 75,000 cells/well into a 24-well plate. The following day, the culture media was supplemented with pyrogallol, paraquat, menadione, H_2O_2, or 4-HNE for 8 h, after which the media was replaced with fresh media containing 0.5 mg/mL MTT for 1 h. The media was then removed before dissolving the reduced cellular MTT in DMSO. Cell viability was determined by measuring the absorbance at 570 nm and normalizing absorbances to the vehicle condition.

<u>BVR enzymatic activity assays</u>

BVR activity was assayed at pH 8.5 at 37°C. Tissues were dounce homogenized at 4°C in lysis buffer (pH 7.4 solution of 50 mM Tris-HCl, 150 mM NaCl, 1% Triton X-100, and 5% glycerol) supplemented with protease inhibitors (Sigma).

Lysates were centrifuged at 16,000*g* for 15 min at 4°C. 50 micrograms of clarified lysate was incubated for 5 min at room temperature in a pH 8.5 solution of 50 mM Tris, NADP+, glucose-6-phosphate, and glucose-6-phosphate dehydrogenase (NADPH Regeneration System, Promega). The samples were then placed at 37°C and spiked with 10 µM biliverdin IXα. Reaction rates were determined by monitoring the change in absorbance at 442 nm over time.

Live-cell imaging and analysis

DHE ROS imaging

MEFs: To compare the ROS scavenging capacities of WT and $BVR^{-/-}$ MEFs, cells were treated with 25 µM menadione for 1 h. MEFs were then loaded with 25 µM dihydroethidium (DHE) for 45 min, after which they were washed and maintained in HBSS for imaging. Cells were immediately photographed with a confocal microscope.

Brain slices: To assess ROS levels *ex vivo*, cerebellar slices were treated with 100 µM pyrogallol for 30 min in E-aCSF. After washing with E-aCSF, slices were loaded with 10 µM DHE in aCSF for 45 min. After washing with E-aCSF, slices were immediately photographed with a fluorescent confocal microscope. Sections were assayed at room temperature in E-aCSF continuously bubbled with 95% O_2 and 5% CO_2.

MitoSOX Red ROS imaging

MEFs: To specifically quantify mitochondrial ROS, MEFs were plated at a density of 10,000 cells/well in a 96 well plate. The following day, the cells were treated with 25 μM rotenone (Sigma) for 4 h in fresh media. Cells treated with bilirubin were pre-treated with 500 nM bilirubin for 30 min just prior to rotenone. The MEFs were then loaded with 5 μM MitoSOX Red in HBSS for 15 min, after which they were washed and maintained in HBSS for imaging. Cells were immediately photographed with a fluorescent confocal microscope.

Mitochondrial bilirubin imaging

To observe mitochondrial bilirubin, MEFs were plated at a density of 60,000 cells/well in a 35 mm glass-bottom plate (MatTEK). The following day, MEFs were transfected with mitochondria-targeted UnaG (mitoUnaG, Dr. Park Lab) and mitochondria-targeted BFP (mitoBFP, Addgene) using Lipofectamine 3000 (Invitrogen) per the manufacturer's instructions. Two days later, the media was replaced with media lacking phenol red and imaged with a fluorescent confocal microscope. To assess bilirubin trafficking to the mitochondria, exogenous bilirubin was added to the dish to a final concentration of 1 μM. UnaG fluorescence was imaged at several time points.

Neuronal DHE and UnaG imaging

To observe neuronal DHE or UnaG fluorescence, mouse primary cortical neurons were isolated from E15.5-E17.5 mice and plated at a density of 1 million cells/well in a 35 mm glass-bottom plate (MatTEK). Neurons were maintained in

Neurobasal medium for at least 14 days *in vitro* (DIV) before imaging. Neurons were imaged at 25°C in neuronal extracellular solution (NES) (pH 7.3 solution of 5 mM HEPES, 125 mM NaCl, 2.5 mM KCl, 2 mM $CaCl_2$, and 33 mM glucose). After establishing baseline fluorescence over 2 min, neurons were treated with either 100 µM NMDA + 10 µM glycine, 50 µM (*S*)-AMPA, or 50 µM kainate. Neurons treated with (*S*)-AMPA or kainate were pre-equilibrated with NES supplemented with 2 mM $MgCl_2$ and/or 50 µM APV.

a. DHE fluorescence imaging: Neurons were loaded with 5 µM DHE in NES for 15 min at 25°C, after which neurons were washed twice in NES.
b. UnaG fluorescence imaging: Neurons were transfected with UnaG cDNA at two days before imaging, typically DIV12.

Image analysis

Digitized images were quantified with FIJI (ImageJ). The mean fluorescence signal intensity was measured as the mean of the frequency distribution of all collected pixels. When imaging MEFs, frequency distributions were pooled from 3-4 replicates per sample condition. When imaging tissues *ex vivo*, frequency distributions were pooled from 2 sections per brain for each 'n'.

<u>UnaG purification</u>

UnaG was expressed in pMAL-6P2-6xHIS in BL21(DE3) cells. Starter cultures were grown to saturation overnight in Luria Broth (LB) at 37°C and then diluted 10-fold in LB and grown to an OD_{600} of 0.3 at 37°C, after which cultures were

moved to 18°C. At OD_{600} of 0.6, UnaG expression was induced by the addition of 400 μM isopropyl β-D-1-thiogalactopyranoside for 16 h at 18°C. Cells were harvested by centrifugation, resuspended in 15 ml of resuspension buffer (50 mM HEPES, 300 mM NaCl, 0.5 mM TCEP, 10% glycerol, 1 mM PMSF, 2.34 μM leupeptin, 1.45 μM pepstatin at pH 7.4) per liter of culture, and flash frozen in liquid nitrogen. Pellets were thawed on ice and sonicated to lyse. Lysate was clarified by centrifugation at 26,000g at 4°C for 30 min and subsequently loaded onto an amylose column. Protein was eluted with 20 mM maltose in protease buffer (50 mM Tris, 150 mM NaCl, 0.5 mM TCEP, 10% glycerol, 0.01% TritonX-100 at pH 7.4), after which the MBP was were removed by the addition of Prescission Protease (GE Healthcare) for 16 h at 4°C. UnaG was further purified via a nickel column to remove the cleaved tag and Prescission Protease. Protein was further purified on a gel-filtration column (S-200, GE Healthcare) in 50 mM HEPES, 300 mM NaCl, 0.5 mM TCEP, 10% glycerol at pH 7.4, concentrated, and flash frozen in gel filtration buffer at 30% glycerol for storage at −80 °C.

Bilirubin immunostaining

8-12 weeks old mice were anesthetized with 50 mg/kg pentobarbital and transcardially-perfused with 20 mL cold 0.1 M heparin/PBS (pH 7.4), followed by 25 mL of cold fixative (4% formaldehyde (v/v)). Tissues were post-fixed in 4% paraformaldehyde overnight at 4°C and then cryoprotected through a series of 10%, 20%, and 30% sucrose (w/v) gradients for 48 h at 4°C. Tissues were then embedded in Optimal Cutting Temperature compound (OCT) and sectioned in

30 µm intervals with a cryostat, after which the sections were dried on slides for at least 1 h at 25°C. Sections were fixed with 4% paraformaldehyde for 15 min at 25°C and then permeabilized with 100% methanol for 7 min at -20°C. The slides were then pre-incubated in blocking solution (50% Seablock (ThermoFisher Scientific) (v/v) in TBS-T, pH 7.4) for 30 min at 25°C. Sections were incubated overnight at 4°C with a rabbit polyclonal anti-bilirubin antibody (1:100) in blocking solution. Sections were washed and incubated with goat anti-rabbit secondary antibody (Alexa 488, A32723 Invitrogen) diluted 1:250 in blocking solution for 1 h at 25°C. Tissues were then mounted with ProLong Gold Antifade Mountant with DAPI (Invitrogen). Primary bilirubin antibody was generated as previously described (Doré et al., 1999).

Lipid peroxidation quantification

DIV10-14 primary WT and $BVR^{-/-}$ cortical neurons were exposed to vehicle or 10 µM glycine/100 µM NMDA for 20 min in control salt solution (CSS) (pH 7.4 solution of 120 mM NaCl, 5.4 mM KCl, 1.8 mM $CaCl_2$, 25 mM Tris HCl, 15 mM glucose). Neurons were washed twice in CSS and then re-fed conditioned media for another 24 h, after which thiobarbituric acid-reactive substances (TBARS) were measured. TBARS were quantified using the OxiSelect TBARS Assay Kit (Cell Biolabs) per the manufactures instructions. Neurons treated with bilirubin were pre-treated with 50 nM bilirubin for 1 h prior to glycine/NMDA.

Stereotactic microinjections

Adult male mice (2-3 month old) were anesthetized with ketamine (80-100 mg/kg) and xylazine (5-10 mg/kg) and subsequently immobilized to a stereotaxic frame (Stoelting Digital Mouse Stereotaxic Instrument) with ear bars. Mice were maintained at 37°C with a heating pad during surgery. The needle was inserted at a rate of 0.1 mm/s and extracted at a rate of 0.5 mm/min, with a 5 min needle dwell time before extraction.

NMDA

Mice treated with NMDA received unilateral intracortical microinjections of 20 nmoles NMDA with a contralateral microinjection of PBS as a control. NMDA was delivered in a final volume of 0.2 µL over 2 min. NMDA was injected at the following coordinates: AP = 0.5, ML = -2.5, DV = -0.5.

Rotenone

Mice treated with rotenone received unilateral intracerebellar microinjections of 2.5 nmoles rotenone with a contralateral microinjection of DMSO as a control. Rotenone was delivered in a final volume of 1 µL at a rate of 0.2 µL/min. Rotenone was injected at the following coordinates: AP = -6.5, ML = -2.5, DV = -2.0.

Histology and lesion quantification

Histology and quantification were performed as previously described (Paul et al., 2014). In brief, mice were euthanized 2 days post-injection, after which brains were fixed, cryopreserved, and sectioned in the same manner as with bilirubin immunostaining. Dry sections were then stained with Nissl stain. Lesional

volumes were calculated blinded to both genotype and treatment as a sum of 10 sections for NMDA-induced lesions and 6 sections for rotenone-induced lesions, using Cavalieri's principle (Cyr et al., 2005) ($V = s_1 d_1 + s_2 d_2 + \ldots + s_n d_n$, where s is surface area and d is the distance between two sections).

Behavioral tests

Behavioral tests were performed on 2-4 months old WT and $BVR^{-/-}$ littermate male mice. Baseline, NMDA- and MK-801-induced activity in the open field was assessed using activity chambers equipped with infrared beams (Photobeam Activity System; San Diego Instruments, San Diego, CA, USA). Behavioral assays were initiated by placing mice were placed in the center of an enclosed acrylic chamber. Mice were initially habituated to the chambers for 30 min followed by a single injection of either NMDA (100 mg/kg, i.p.) or MK-801 (0.3 mg/kg, i.p.). Total locomotor activity was automatically recorded and analyzed via photobeams in the x and y directions.

Quantification and Statistical Analysis

Group data were expressed as mean ± SEM unless otherwise noted. Statistical comparisons were performed using two-tailed unpaired Student's t-tests and ANOVA analyses, as noted. Differences were considered significant at $P < 0.05$. All *ex vivo* or *in vivo* experiments were performed concomitantly or in a blocked manner with consideration for both genotype and treatment.

Identification of a bilirubin receptor that may mediate a component of cholestatic itch

Summary

Various pathologic conditions result in jaundice, a yellowing of the skin due to a buildup of bilirubin. Patients with jaundice commonly report experiencing an intense non-histaminergic itch. Despite this association, the pruritogenic capacity of bilirubin itself has not been explored, and no bilirubin receptor has been identified. Here, we demonstrate that pathophysiologic levels of bilirubin excite peripheral itch sensory neurons and elicit pruritus through *Mrgprs*, a family of G-protein coupled receptors expressed in primary sensory neurons. Bilirubin binds and activates two *Mrgprs*, mouse MRGPRA1 and human MRGPRX4. In two mouse models of pathologic hyperbilirubinemia, we show that genetic deletion of either *Mrgpra1* or *Blvra*, the bilirubin-producing enzyme, attenuates itch. Similarly, plasma isolated from hyperbilirubinemic patients evoked itch in wild-type animals but not *Mrgpra1*-/- animals. Removing bilirubin decreased the pruritogenic capacity of patient plasma. Based on these data, targeting MRGPRs is a promising strategy for alleviating jaundice-associated itch.

Introduction

Chronic pruritus, or itch, is a complex and often debilitating symptom that accompanies a range of cutaneous and non-cutaneous diseases (Ständer et al., 2007; Yosipovitch and Bernhard, 2013),(Yamamoto et al., 2009; Yosipovitch et al., 2000). The most widely known pruritogen is histamine, which is secreted by mast cells in the skin and activates histamine receptors on nearby sensory neurons (Bautista et al., 2014; Ikoma et al., 2006; LaMotte et al., 2014; Yosipovitch and Bernhard, 2013). While viable treatments exist for histamine-mediated itch, most non-histaminergic conditions are more difficult to treat because the mediators are often unknown (Kremer et al., 2011).

Jaundice, or yellowing of the skin, sclera, and mucosa due to abnormal accumulation of the yellow heme metabolite bilirubin, is often associated with chronic non-histaminergic pruritus. Jaundice often presents in patients with hepatobiliary disorders such as cholestasis, characterized by impaired bile flow. Physiologically, bilirubin is typically bound to albumin in serum and concentrates in the liver, where it is conjugated to glucuronic acid and subsequently excreted in bile. At physiologic and mildly elevated concentrations (0.2-2.7 mg/dL, 3.4 - 46.2 μM), bilirubin is benign. At highly elevated levels however, such as in cutaneous jaundice (> 5 mg/dL, > 85.5 μM bilirubin), it is associated with pruritus, a correlation first noted by physicians as early as the second century B.C.E. (Bassari, 2015).

Results

Bilirubin elicits non-histaminergic, Mrgpr*-dependent pruritus*

Despite the long-standing association between jaundice and pruritus (Talwalkar et al., 2003), bilirubin itself has not been tested as a pruritogen. To determine whether bilirubin directly elicits pruritus, we subcutaneously injected bilirubin into the napes of mice. Pathophysiologic concentrations of bilirubin stimulated scratching in a dose-dependent manner at the site of injection (**Fig. 26a**). Pre-incubating bilirubin with excess human serum albumin, which binds bilirubin with high affinity (Breaven et al., 1973; Griffiths et al., 1975; Jacobsen and Broderson, 1983), elicited fewer scratches (**Fig. 26a**). The behavioral profile of bilirubin-induced scratching mirrored that of two well-characterized pruritogens, histamine and chloroquine (**Fig. 26b**). Notably, histamine and chloroquine only elicit itch when injected into mice at millimolar concentrations despite having nanomolar affinity towards their receptors. In comparison, bilirubin elicited a similar degree of itch even when injected at lower concentrations than histamine or chloroquine (**Fig. 26b**). Since mice indiscriminately scratch if injected at the nape with substances that trigger either itch or pain, we also injected mice at the cheek. Unlike at the nape, painful sensations at the cheek evoke a distinct wiping behavior instead of scratching, whereas itchy sensations still elicit scratching (Shimada and LaMotte, 2008). Injecting bilirubin in the cheek prompted dose-dependent scratching just as it did at the nape (**Fig. 27a**). Bilirubin elicited neither wiping nor licking, indicating that it selectively triggers itch and not pain (**Fig. 27b-c**).

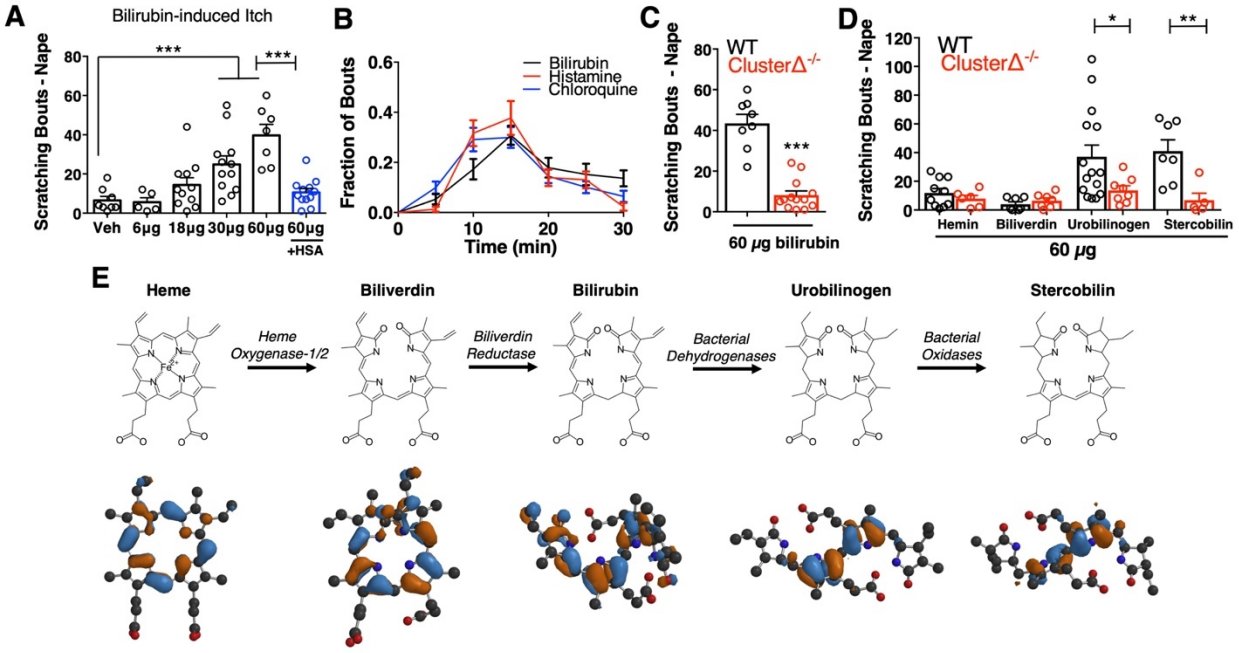

Figure 26. Bilirubin elicits non-histaminergic, *Mrgpr*-dependent pruritus.

a, Scratching bouts associated with injection of bilirubin. The indicated amount of bilirubin was injected into the nape of mice. The blue bar (+HSA) represents animals injected with 60 µg bilirubin pre-incubated with 1% human serum albumin. Veh n = 8; 6 µg n = 5, 18 µg n = 11, 30 µg n = 12, 60 µg n = 7,+HSA n = 12. **b**, Time course of itch behavior associated with bilirubin, histamine, or chloroquine. Scratching bouts were binned according to 5 min intervals. Bilirubin n = 16, Histamine n = 13, Chloroquine n = 11. **c**, 60 µg bilirubin was injected into the nape of WT and Mrgpr-cluster KO littermates. WT n = 8, Mrgpr-cluster KO n = 13. **d**, 60 µg of the indicated metabolite was injected into WT and Mrgpr-cluster KO littermates. Hemin (WT n = 10, Mrgpr-cluster KO n = 6), Biliverdin (WT n = 7, Mrgpr-cluster KO n = 7), Urobilinogen (WT n = 15, Mrgpr-cluster KO n = 8), Stercobilin (WT n = 7, Mrgpr-cluster KO n = 5). **e**, The pathway of heme degradation. The skeletal formula of each metabolite is depicted above its optimal 3D geometry, as calculated by a B3LYP functional and 6-31G(d) basis set. Blue and orange represent orbital parity of each metabolite's HOMO obtained from DFT calculations. (*a, c, and d*) Mean ±s.e.m. depicted. Each open circle represents an individual mouse. *, $p < 0.05$; **, $p < 0.01$; ***, $p < 0.001$; two-tailed unpaired Student's *t*-test.

We injected mice with similarly structured metabolites to determine the specificity of bilirubin's pruritic activity (**Fig. 26e**). The two metabolites directly epistatic to bilirubin, hemin and biliverdin, did not induce scratching despite also being tetrapyrroles (**Fig. 26d**). While hemin, biliverdin, and bilirubin display only minor atomic and electronic differences between them, they vary substantially in their physiochemical properties and structures (**Fig. 26e**). To

better understand these differences, we performed density functional theory (DFT) calculations (Becke, 1993; Hohenberg and Kohn, 1964; Kohn and Sham, 1965; Stephens et al., 1994) followed by single point energy calculations to determine the optimal geometry of each metabolite. Unlike in heme and biliverdin, bilirubin's four pyrroles are extended and do not lie in the same plane (**Fig. 26e**). DFT calculations revealed that urobilinogen and stercobilin, two bacterial metabolites derived from bilirubin, adopt a similar extended conformation. Both urobilinogen and stercobilin were able to stimulate scratching behavior (**Fig. 26d**), indicating that bilirubin's non-polar pyrroles may be important for its pruritic activity.

Patients with jaundice-associated pruritus receive little benefit from antihistamines (Carstens et al., 2014). Consistent with these clinical findings, the histamine receptor 1 blocker cetirizine (30 mg/kg, *i.p.)* failed to alleviate scratching behavior in mice injected with bilirubin (**Fig. 27d**). Furthermore, bilirubin did not elicit a calcium response or induce appreciable histamine release from peritoneal mast cells (**Fig. 27e-f**).

The Mas-related G-protein coupled receptor (*Mrgpr*) family of receptors is a major mediator of non-histaminergic pruritus (Han et al., 2012; Liu et al., 2012; 2009; Sikand et al., 2011). To test whether *Mrgpr*s mediate bilirubin-induced pruritus, we injected mice lacking a cluster of 12 *Mrgpr* genes (Mrgpr-cluster$\Delta^{-/-}$) with bilirubin (Liu et al., 2009). Mrgpr-cluster$\Delta^{-/-}$ animals scratched approximately 75% less than wild type (WT) mice, indicating that one or more of the 12 *Mrgpr*s within the cluster mediates bilirubin-induced pruritus (**Fig. 26c**).

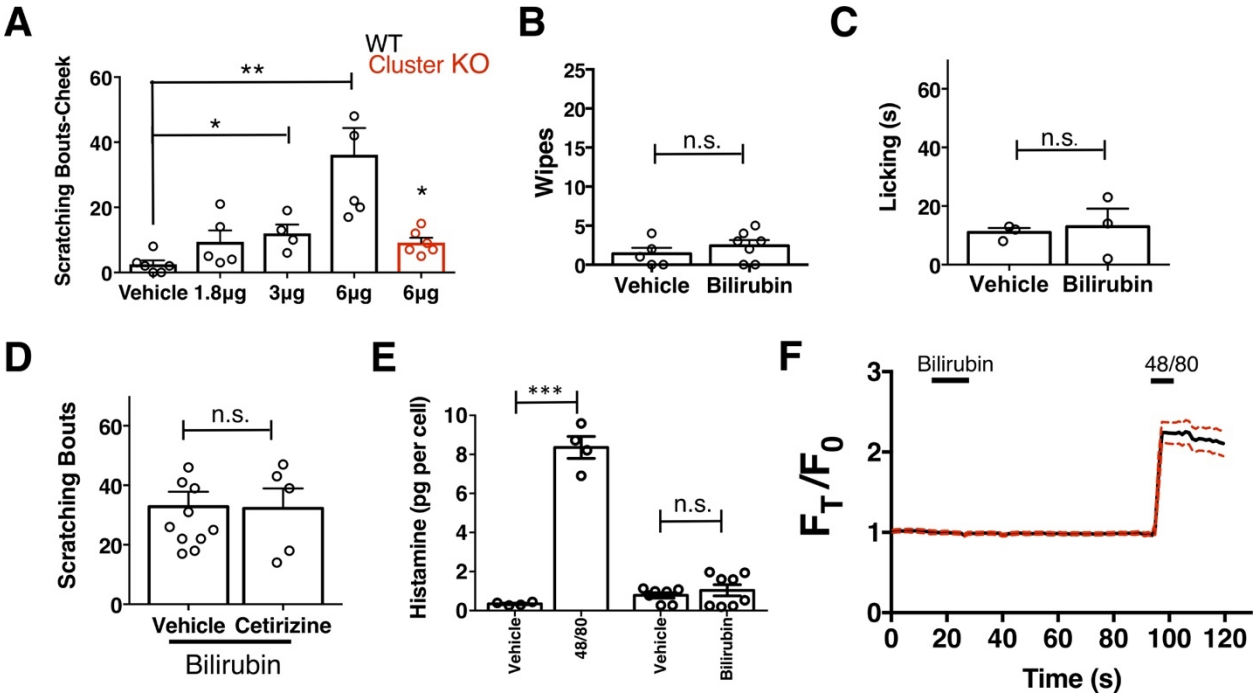

Figure 27. Bilirubin elicits non-histaminergic pruritus and not pain.

a, Scratching bouts associated with cheek injection of bilirubin. The indicated amount of bilirubin was injected in a 10 µl volume and the number of scratching bouts was assessed for 30 min. Vehicle n = 6, 1.8 µg n = 5, 3 µg n = 4, 6 µg n = 5, 6 µg (Mrgpr-clusterΔ$^{-/-}$) n = 6. **b**, Wiping associated with injection of 6 µg bilirubin into the cheek. Wipes were assessed for 10 min post-injection, vehicle n = 5, bilirubin n = 7. **c**, Lick time associated with injection of 6 µg bilirubin into the paw. Licking was assessed for 10 min post-injection. n = 3 per condition. **d**, H1 blocker does not inhibit bilirubin-induced pruritus. Either vehicle or 30 mg/kg Cetirizine was given *i.p.* 30 min prior to injection of bilirubin at the nape of the neck. Scratching bouts were assessed for 30 min post-injection. Vehicle n = 10, Cetirizine n = 5. **e**, Mast cell histamine release in response to 100 µM bilirubin. Vehicle for Compound 48/80 n = 4, Compound 48/80 (10 µg/mL) n = 4, Vehicle n = 6, Bilirubin n = 8. **f**, Ca^{2+} imaging of murine peritoneal mast cells. After a 10 s baseline, 100 µM bilirubin was added. 15 s later, a 1 min wash was applied before addition of 10 µg/mL compound 48/80. Drugs were applied when indicated by the black bars. Mean ±95% CI depicted. n = 26. (*a-e*) Mean plus s.e.m. depicted. Open circles represent independent data points. *, $p < 0.05$; **, $p < 0.01$; ***, $p < 0.001$; two-tailed unpaired Student's *t*-test. n.s., not significant.

Bilirubin activates murine MRGPRA1 and human MRGPRX4

To identify which *Mrgpr* is sensitive to bilirubin, we individually expressed each of the 12 *Mrgpr*s deleted in the Mrgpr-clusterΔ$^{-/-}$ mouse in human embryonic kidney (HEK) 293 cells and monitored changes in intracellular

calcium upon applying bilirubin. To ensure we would observe a calcium response following a true ligand-receptor interaction, we expressed the receptors in HEK293 cells stably expressing the G-protein alpha-subunit $G_{\alpha 15}$, a G_{α} protein that couples GPCRs to intracellular calcium stores via phospholipase C (PLC).

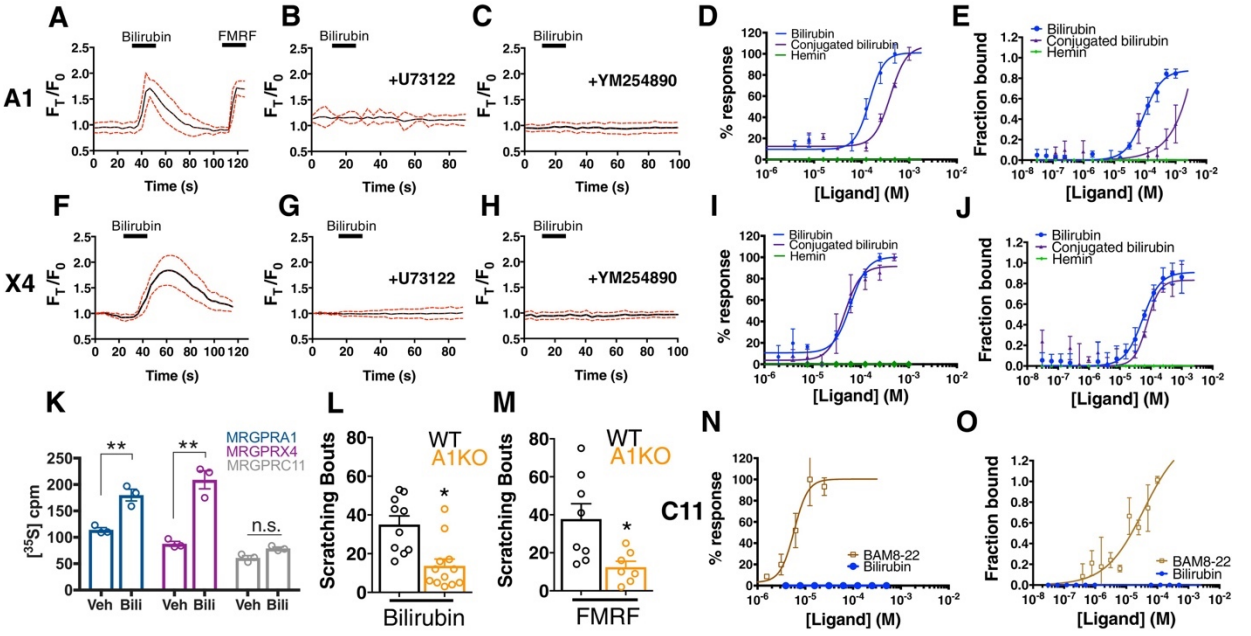

Figure 28. Bilirubin activates murine MRGPRA1 and human MRGPRX4.

Ca^{2+} imaging and transformed binding isotherms of HEK293 cells stably expressing MRGPRA1 (**a-e**) or MRGPRX4 (**f-j**). **a-c and f-h**, 50 μM bilirubin was added where indicated by black bars. After 15 s, a 1 min wash was applied. Mean ±95% confidence interval (CI) depicted. n = 10. In (*a*) 30 μM FMRF was added after washing as indicated by the black bar. In (*b-c*) and (*g-h*), cells were pre-incubated with either 10 μM of the PLC inhibitor U73122 or 10 μM of the $G_{\alpha q}$ inhibitor YM254890 for 30 min prior to imaging. Concentration–Ca^{2+} response curves of bilirubin, conjugated bilirubin, and hemin towards (*d*) MRGPRA1, (*i*) MRGPRX4, and (*n*) MRGPRC11 and BAM8-22 towards MRGPRC11, an established peptide ligand. Data are a representative experiment of three independent replicates performed in triplicate, depicted as mean ±s.e.m. Transformed binding isotherms for bilirubin, conjugated bilirubin, and hemin to (*e*) MRGPRA1, (*j*) MRGPRX4, and (*o*) MRGPRC11 and BAM8-22 to MRGPRC11. Data are an average of three independent experiments, depicted as mean ±s.e.m. **k**, Bilirubin-stimulated G-protein activity of partially-purified MRGPRA1, MRGPRX4, and MRGPRC11 membrane complexes. [^{35}S]GTPγS binding was measured in the presence of 0.5% DMSO or 50 μM bilirubin. Mean ±s.e.m. depicted. **, $p < 0.01$; two-tailed unpaired Student's *t*-test. **l**, Scratching bouts from injection of 60 μg of bilirubin in WT and A1 KO animals. WT n = 10, A1 KO n = 12. **m**, Scratching bouts from injection of 60 μg of FMRF in WT and A1 KO animals. WT n = 8, A1 KO n = 7. (*l-m*) Mean ±s.e.m. depicted. Open circles represent individual mice. *, $p < 0.05$ by two-tailed unpaired Student's t-test.

Among the twelve cell lines expressing an *Mrgpr*, only MRGPRA1-expressing cells exhibited a calcium response to bilirubin (EC_{50} of 145.9 μM [96, 220]) (**Fig. 28a and 28d**). The same cells that responded to bilirubin also responded to FMRF, an MRGPRA1 agonist (Dong et al., 2001). To ensure that bilirubin initiated signaling at MRGPRA1 and not downstream, we pre-treated MRGPRA1-expressing cells with inhibitors of GPCR signaling: the PLC inhibitor U73122 or the $G_{\alpha q}$ inhibitor YM-254890. Both compounds abolished bilirubin-induced calcium responses (**Fig. 26b-c**).

In addition to bilirubin, glucuronidated bilirubin is often upregulated in jaundice-associated itch. We assessed whether ditaurate bilirubin, a distinct but similar bilirubin derivative, could activate MRGPRA1. Indeed, ditaurate bilirubin activated MRGPRA1-expressing cells (**Fig. 28d)**. Hemin failed to activate MRGPRA1 (**Fig. 28d)**, consistent with our earlier behavioral findings in which hemin did not evoke scratching. No other *Mrgpr* among the 12 that we screened responded to bilirubin (**Fig. 28n and Fig. 29**).

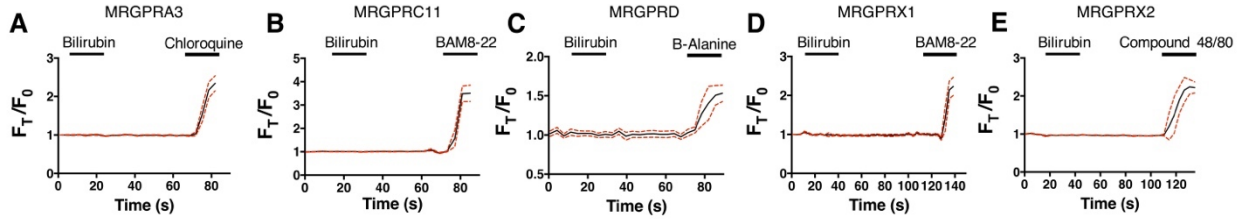

Figure 29. Bilirubin does not activate other itch-associated Mrgprs.

a-e, Ca^{2+} imaging of HEK293 cells transiently expressing (*a*) MRGPRA3, (*b*) MRGPRC11, (*c*) MRGPRD, (*d*) MRGPRX1, or (*e*) MRGPRX2. 50 μM bilirubin was added where indicated by black bars. After fifteen seconds, a one-minute wash was applied. After washing, either (*a*) 1 mM chloroquine, (*b*) 3 μM BAM8-22, (*c*) 1 mM β-alanine, (*d*) 3 μM BAM8-22, or (*e*) 10 μg/mL compound 48/80 was added as indicated by black bars. Mean ±95% CI depicted. n = 10.

The human *MRGPRX* family of receptors has functional similarities between species but have no obvious structural homologs in rodents (Solinski et al., 2014; Zylka et al., 2003). The mouse *Mrgpra* family is closest in sequence homology to the human *MRGPRX* family (Dong et al., 2001; Lembo et al., 2002; Zhang et al., 2005). Of the four human MRGPRX receptors, only MRGPRX4-expressing cells responded to bilirubin (EC_{50} of 61.9 μM [44, 87]) (**Fig. 28f and 28i**). U73122 and YM-254890 inhibited bilirubin-induced calcium responses in MRGPRX4-expressing cells just as with MRGPRA1 (**Fig. 28g-h**). Conjugated bilirubin also activated MRGPRX4, whereas hemin had no effect (**Fig. 28i**).

To confirm that bilirubin directly binds the identified receptors, we assayed thermophoresis of each receptor in the presence and absence of bilirubin. Thermophoresis of a molecule is affected by physical parameters such as size, charge, and solvation. By extension, the thermophoresis of one molecule is altered when it interacts with another, and can therefore be used to measure interactions between molecules (Duhr and Braun, 2006). Using this approach, we determined that bilirubin bound MRGPRA1 with a K_D of 92.9 ± 15 μM and MRGPRX4 with a K_D of 54.4 ± 13 μM (**Fig. 28e and 28j**). Bilirubin exhibited little to no affinity for the closely related BAM8-22 receptor MRGPRC11 (**Fig. 28o**). Hemin, which did not activate MRGPRA1 or MRGPRX4 by calcium imaging (**Fig. 28d and 28i**), also did not bind MRGPRA1 or MRGPRX4 (**Fig. 28e and 28j**). Conjugated bilirubin bound both MRGPRA1 and MRGPRX4, although with a lower affinity than unconjugated bilirubin (**Fig. 28e and 28j**). To make certain that bilirubin activates MRGPRA1 and MRGPRX4 upon binding, we measured

exchange of guanosine diphosphate (GDP) for guanosine triphosphate (GTP), one of the first events in GPCR signaling. Bilirubin increased GTP binding to MRGPRA1 and MRGPRX4 membrane complexes, but not to MRGPRC11 (**Fig. 28k**). To confirm that bilirubin activates MRGPRA1 *in vivo* to trigger itch, we generated an *Mrgpra1* (A1-/-) knockout mouse line using CRISPR-Cas9 (Jinek et al., 2012) (**Fig. 30**). A1-/- animals scratched significantly less than WT mice after exposure to either bilirubin or the established agonist FMRF, demonstrating that Mrgpra1 is functional in adult mice (**Fig. 28l-m**)**.** The K_D of bilirubin towards MRGPRA1 and MRGPRX4 suggests that bilirubin likely does not interact with these receptors in healthy individuals. Additional ligands with nanomolar affinities towards MRGPRA1 or MRGPRX4 may exist that modulate the receptors in normal physiology.

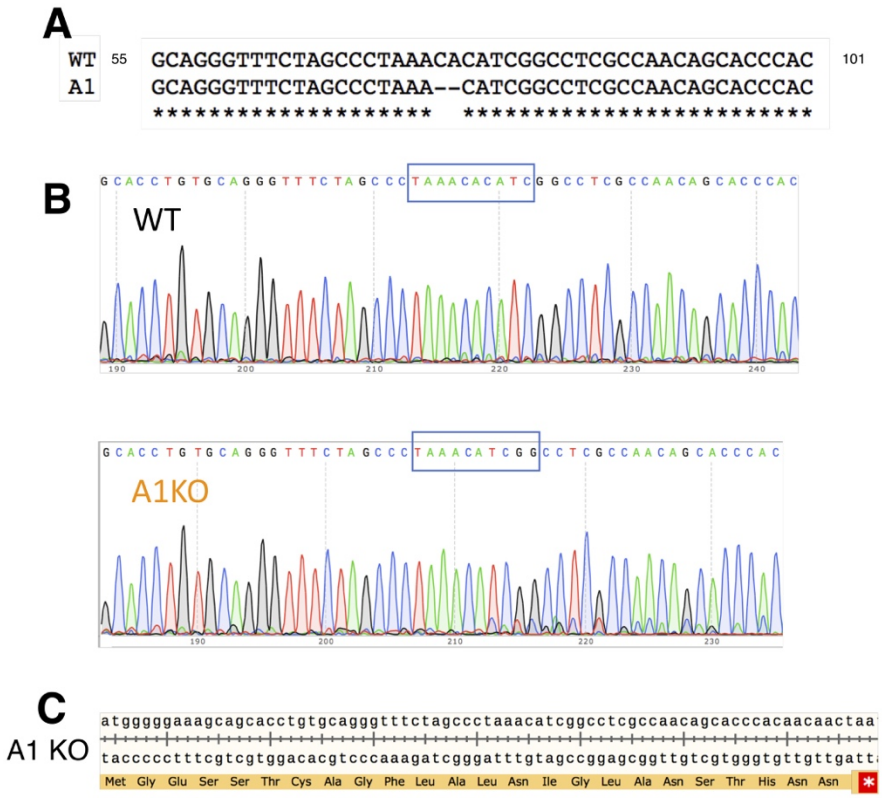

Figure 30. CRISPR deletion of MRGPRA1.

a, Comparison of WT and A1 KO genomic sequences. Location of 2 base pair (bp) deletion shown by dashes. Numbers correspond to MRGPRA1 open reading frame. **b**, Sequencing data depicting the 2 bp deletion. **c**, A translation of the open reading frame of MRGPRA1 KO beginning with the start codon. The 2 bp deletion creates a frameshift which results in early termination, marked by a red asterisk.

Bilirubin activates sensory neurons in an MRGPR-dependent manner

We reasoned that if bilirubin triggers itch through MRGPRA1 and MRGPRX4, bilirubin should activate these receptors in sensory itch neurons. Previous studies have demonstrated that both Mrgpra1 and MRGPRX4 are expressed in sensory neurons within the dorsal root ganglia (DRG) (Dong et al., 2001; Flegel et al., 2015; Lembo et al., 2002). Mrgpra1 is expressed in a subset of adult DRG and trigeminal ganglia (TG) sensory neurons that innervate the skin and ramify in lamina I and II of the spinal cord (**Fig. 31a-d**). Bilirubin elicited robust action potentials in small-diameter (< 30 μm) WT DRG sensory

neurons at a proportion consistent with the percentage of sensory neurons that encode itch (5 of 50). Bilirubin failed to elicit action potentials in A1 -/- neurons (0 of 60), suggesting bilirubin activates sensory neurons through MRGPRA1 (**Fig. 31e**). Bilirubin-sensitive neurons had an average somal diameter of 20.4 ± 1.3 μm, a diameter characteristic of itch sensory neurons (**Fig. 31f**). Applying bilirubin to neurons elicited calcium transients in approximately 5% of WT DRG neurons (**Fig. 31g**), whereas significantly fewer sensory neurons from either Mrgpr-clusterΔ$^{-/-}$ or A1$^{-/-}$ mice responded (**Fig. 31h**). We sought to determine whether expression of either MRGPRA1 or MRGPRX4 was sufficient to render neurons sensitive to bilirubin. To address this question, we infected Mrgpr-clusterΔ$^{-/-}$ DRGs with lentivirus carrying either *Mrgpra1*, *MRGPRX4*, or *MRGPRX3*. Bilirubin activated 14% of *Mrgpra1*-and 32% of *MRGPRX4*-transduced Mrgpr-clusterΔ$^{-/-}$ DRGs (**Fig. 31i-j**). Mrgpr-clusterΔ$^{-/-}$ DRGs infected with the control gene *MRGPRX3* did not respond to bilirubin.

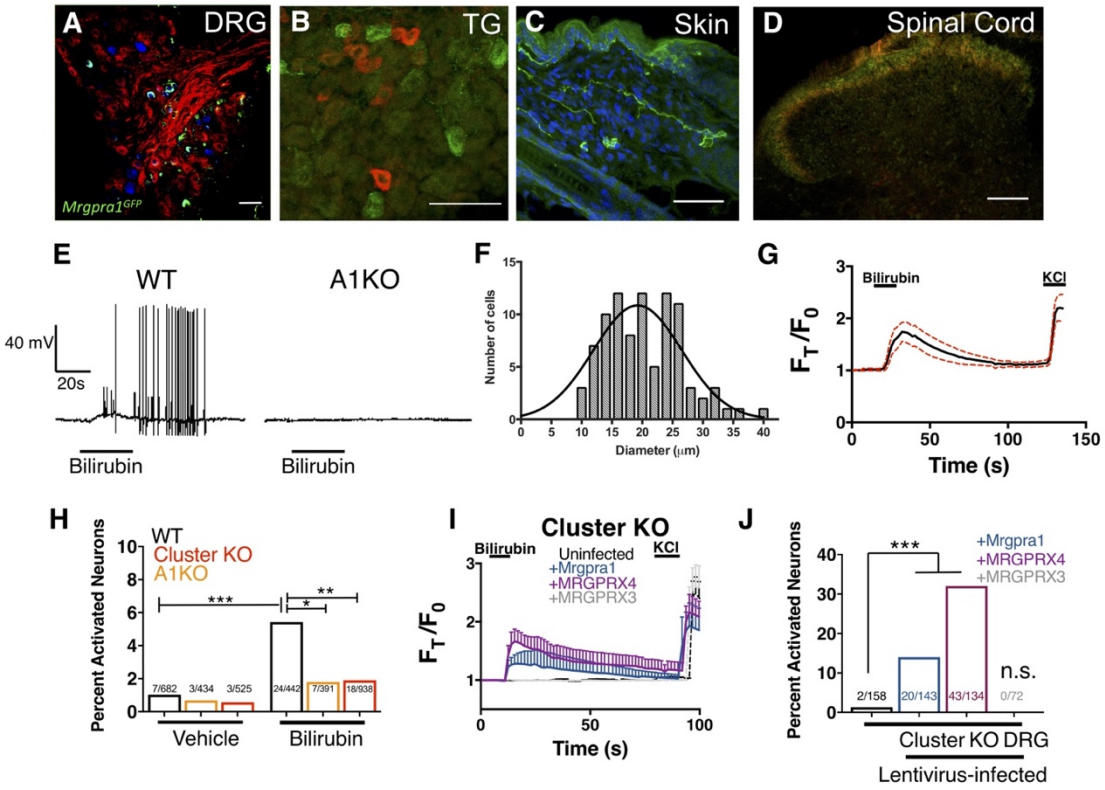

Figure 31. Bilirubin activates sensory neurons in an Mrgpr-dependent manner.

a-d, Confocal microscopy immunofluorescence images of adult mouse tissue sections from Mrgpra1^{GFP} animals with GFP expression under the control of the endogenous *Mrgpra1* locus. **a**, Mrgpra1 expression in dorsal root ganglia. Green depicts Mrgpra1^{GFP}. Red depicts anti-PLAP antibody staining where PLAP expression is controlled by the endogenous *Mrgprd* locus (*Mrgprd*^{PLAP}). Blue depicts antibody staining against calcitonin gene-related peptide (CGRP). Scale bar is 50 μM. **b**, Trigeminal ganglia (TG) stained with Mrgpra1^{GFP} (green) and anti-Substance P antibody (red). Scale bar is 50 μm. **c**, Back skin stained with anti-GFP antibody (green) to visualize Mrgpra1^{GFP} nerve fibers in the dermis. Blue represents DAPI counterstain. Scale bar is 50 μm. **d**, Spinal cord (SC) (lamina 1 and 2) stained with anti-GFP and IB4-564. Mrgpra1^{GFP} (green) staining was found in lamina two along with IB4 (red) positive terminals. Scale bar is 100 μm. **e**, Representative whole-cell current-clamp recording of either WT or A1 KO DRG neurons. In WT DRG, bilirubin elicited action potentials in 5 out of 50 small-diameter neurons. In A1 KO DRG, bilirubin elicited action potentials in 0 out of 60 small-diameter neurons. Fisher's exact test $p < 0.05$. **f**, Histogram of bilirubin-activated neuronal soma diameter. **g**, Ca^{2+} imaging of WT DRG neurons. Mean ±95% CI depicted. Compounds applied where indicated by black bars. After a 10 s baseline, 50 μM bilirubin was added. 50 mM KCl was added at the end of each trial. n = 20 neurons. **h**, Percent activation of WT, A1 KO, and Mrgpr-cluster KO DRG by vehicle and 50 μM bilirubin. *, $P < 0.05$; **, $p < 0.01$; ***, $p < 0.001$; Chi-squared test. A neuron was considered to be activated if $\Delta F > 0.2$ for at a least 30 s. **i**, Ca^{2+} imaging of Mrgpr-cluster KO DRG neurons 48 hr after either mock infection with lentivirus (n = 10) or infected with lentivirus encoding *Mrgpra1* (n = 6), *MRGPRX4* (n = 10), or *MRGPRX3* (n = 20). 50 μM bilirubin was added when indicated by the black bar. After 20 s, a 1 min wash was applied before addition of 50 mM KCl. Compounds applied where indicated by black bars. Mean ±95% CI depicted. n = 10 neurons. **j**, Percent activation of uninfected, *Mrgpra1*-infected, *MRGPRX4*-infected, and *MRGPRX3*-infected Cluster -/- neurons by bilirubin. ***, $p < 0.001$. Chi-squared test.

Bilirubin-responsive neurons partially overlapped with neurons that responded to 1mM chloroquine, a ligand for MRGPRA3 that typifies itch sensory neurons (Han et al., 2012) (**Fig. 32a-c**). To validate that bilirubin activates MRGPRA3-positive itch neurons, we performed calcium imaging on DRG neurons isolated from Tg(*Mrgpra3-Cre)*;*lsl-tdTomato* mice, which express the fluorescent protein tdTomato in *Mrgpra3*-expressing neurons. Bilirubin activated a substantial percentage of *tdTomato*-positive neurons (**Fig. 32d**). To confirm that bilirubin activates sensory neurons *in vivo*, we injected 5μL of vehicle or bilirubin into paws of Tg(*Pirt-Cre)*;*lsl-GCaMP6s* mice, which express the fluorescent calcium reporter GCaMP6s in DRG sensory neurons (Kim et al., 2014). Bilirubin, but not vehicle, activated numerous DRG sensory neurons in the paws of GCaMP6s mice (**Fig. 32e**). Inhibiting transient receptor potential (TRP) and other Ca^{2+} channels with ruthenium red prevented bilirubin from activating sensory neurons (**Fig. 32f-g**) (Imamachi et al., 2009; Liu et al., 2009; Roberson et al., 2013).

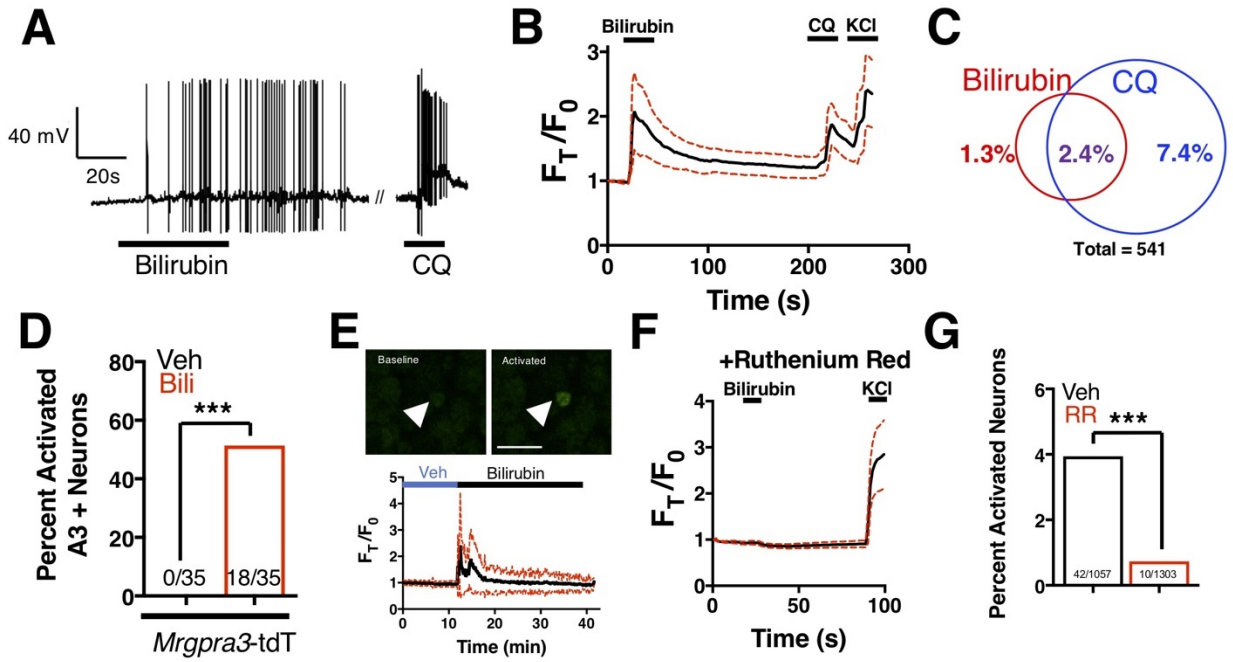

Figure 32. Bilirubin activates a population of small-diameter, chloroquine-sensitive sensory neurons in a TRP channel dependent mechanism.

a, A representative whole-cell current-clamp recording of a WT DRG neuron responsive to addition of both 50 μM bilirubin and 1 mM chloroquine (CQ). **b**, Ca^{2+} imaging of WT DRG neurons. Mean ±95% CI depicted. Compounds applied where indicated by black bars. After a 10 s baseline, 50 μM bilirubin was added. After 20 s, a 3 min wash was applied before 1 mM chloroquine was added. After 15 s, 50 mM KCl was added. n = 10 neurons. **c**, Venn diagram of total neurons activated by either bilirubin and/or chloroquine (Bilirubin alone = 7, Chloroquine = 40, Overlap = 13). **d**, Percent activation of Tg(*Mrgpra3-Cre)*;lsl-tdTomato neurons as assessed by calcium imaging with vehicle, 1 mM Chloroquine, or 50 μM bilirubin. **e**, *In vivo* Ca^{2+} imaging of Pirt-Cre; lsl-GCaMP6s animals. Briefly, a surgery was performed to expose L4 DRG. Baseline measurements were taken before a vehicle injection in ipsilateral paw and subsequent injection of 5 μL of 100 μM bilirubin. Depicted is a representative Ca^{2+} imaging trace of bilirubin-activated neurons, n = 20, identified by post hoc imaging analysis. The black trace is the mean F_t/F_0 and red dotted lines represent 95% confidence intervals. **f**, Neurons were incubated with 10 μM ruthenium red for 10 min before application of 50 μM bilirubin. **g**, Percent activation of WT neurons, incubated with either vehicle or 10 μM ruthenium red, by 50 μM bilirubin.

MrgprA1 KO, Mrgpr-cluster KO, and BVR KO animals exhibit decreased cholestatic pruritus

We wondered whether chronic elevation of bilirubin *in vivo*, like in cholestasis, stimulates *Mrgpr*-dependent itch. Bile is the primary means by which bilirubin is excreted, and patients with cholestasis exhibit elevated levels

of bilirubin and other pruritogenic substances in their blood (Alemi et al., 2013). To induce hyperbilirubinemia and model intrahepatic cholestasis, we administered α-napthyl isothiocyanate (ANIT) to mice (Eliakim et al., 1959). We treated WT, Mrgpr-cluster$\Delta^{-/-}$, and A1$^{-/-}$ animals with 25 mg/kg ANIT for five days before assessing spontaneous itch (**Fig. 33a**). WT, Mrgpr-cluster$\Delta^{-/-}$, and A1$^{-/-}$ animals exhibited equivalently severe hepatocellular injury judged by increases in plasma bilirubin, bile acids, alkaline phosphatase (ALP), aspartate aminotransferase (AST), alanine aminotransferase (ALT), and gamma-glutamyl transferase (GGT) (**Fig. 33d-e and Fig. 34a-d**).

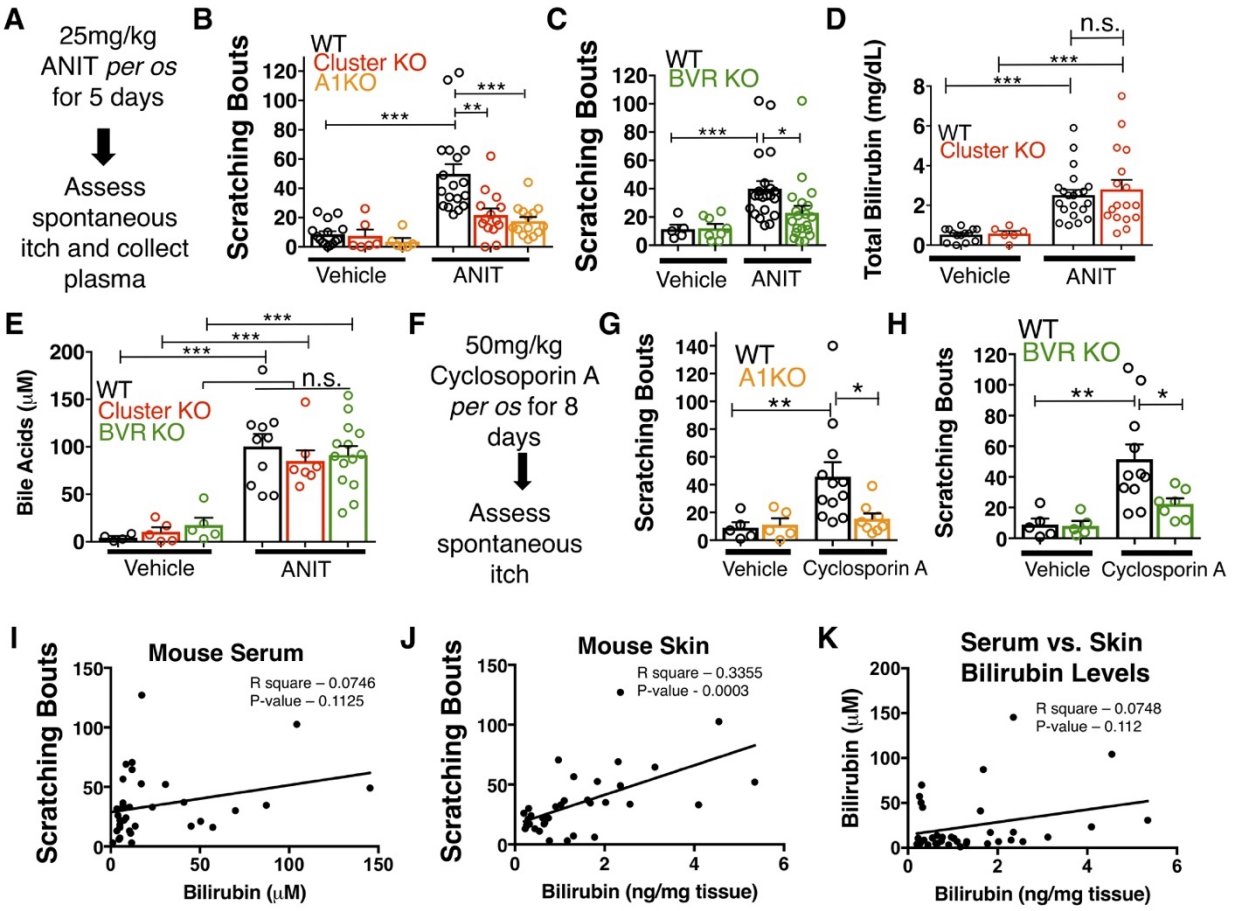

Figure 33. MrgprA1 KO, Mrgpr-cluster KO⁻, and BVR KO animals exhibit decreased cholestatic pruritus.

a, Experimental flowchart for ANIT model of cholestasis. **b**, Scratching bouts for vehicle and ANIT-treated mice among WT, Mrgpr-cluster KO, and A1 KO groups. Bouts were assessed in a 30 min period. For the vehicle cohort: WT n = 15, Mrgpr-cluster KO n = 6, A1 KO n = 6. For ANIT cohort: WT n = 20, Mrgpr-cluster KO n = 14, A1 KO n = 14. **c**, Scratching bouts for vehicle and ANIT-treated animals among WT and BVR KO groups. Bouts were assessed in a 30 min period. For the vehicle cohort: WT n = 5 and BVR KO n = 8. For ANIT cohort: WT n = 21 and BVR KO n = 20. **d**, Plasma bilirubin levels (mg/dL) from WT and Mrgpr-cluster KO ANIT-treated and vehicle-treated animals. For the vehicle cohort: WT n = 14, Mrgpr-cluster KO n = 6. For the ANIT cohort: WT n = 21, Mrgpr-cluster KO n = 17. **e**, Plasma bile acid levels (μM) from ANIT-treated and vehicle-treated animals. For the vehicle cohort: WT n = 4, Mrgpr-cluster KO n = 5, BVR KO n = 5. For the ANIT cohort: WT n = 10, Mrgpr-cluster KO n = 7, BVR KO n = 14. **f**, Experimental flowchart for Cyclosporin A model of cholestasis. **g**, Scratching bouts for vehicle and Cyclosporin A-treated WT and A1 KO animals. For the vehicle cohort: n = 5 for all. For Cyclosporin A cohort: WT n = 10 and A1 KO n = 8. **h**, Scratching bouts from vehicle and Cyclosporin A treated WT and BVR KO animals. For the vehicle cohort: n = 5. For Cyclosporin A cohort: WT n = 11 and BVR KO n = 7. **i**, Correlation of serum bilirubin levels from cholestatic animals and scratching bouts. Line of best fit: Y = 0.23 (X) + 28.78. **j**, Correlation of skin bilirubin levels from cholestatic animals and scratching bouts. Line of best fit: Y = 12.34 (X) + 16.7. **k**, Correlation of skin and serum bilirubin levels from cholestatic animals. Line of best fit: Y = 7.015(X) – 14.52. (*a-h*) Mean ±s.e.m. depicted. Open circles represent individual data points. *, $p < 0.05$; **, $p < 0.01$; ***, $p < 0.001$ by unpaired two-tailed Student's t-test.

As expected, ANIT treatment significantly increased pruritus in all animals (**Fig. 33b**). However, Mrgpr-clusterΔ$^{-/-}$ and A1$^{-/-}$ mice scratched markedly less than WT mice (**Fig. 33b**), suggesting that MRGPRA1 mediates a component of hepatobiliary pruritus. In humans, bile acids, endogenous opioids, and LPA are often increased in cholestatic sera and have been shown to mediate pruritus (Alemi et al., 2013; Bergasa et al., 1998; 1992; Kremer et al., 2010). The serum of ANIT-treated animals exhibited elevated bilirubin and bile acids (**Fig. 33d-e**), whereas neither the endogenous opioid peptide met-enkephalin (Thornton and Losowsky, 1989a; 1989b) nor the LPA-producing enzyme autotaxin were elevated (**Fig. 34e-f**). To assess whether other cholestatic pruritogens act at MRGPRs in mice, we injected WT and Mrgpr-clusterΔ$^{-/-}$ with deoxycholic acid (a bile acid), opiates, and LPA. These other cholestatic pruritogens elicited equivalent degrees of scratching in WT and Mrgpr-clusterΔ$^{-/-}$ animals (**Fig. 35a-d**). Mrgprs are promiscuous receptors. It should be noted that there remain multiple bile acids, LPA molecules, and opiates which remain untested and could be agonists against Mrgprs. However, based on this data, we speculated that Mrgpr-clusterΔ$^{-/-}$ and A1$^{-/-}$ mice scratched less with ANIT because MRGPRA1 mediates bilirubin-induced itch.

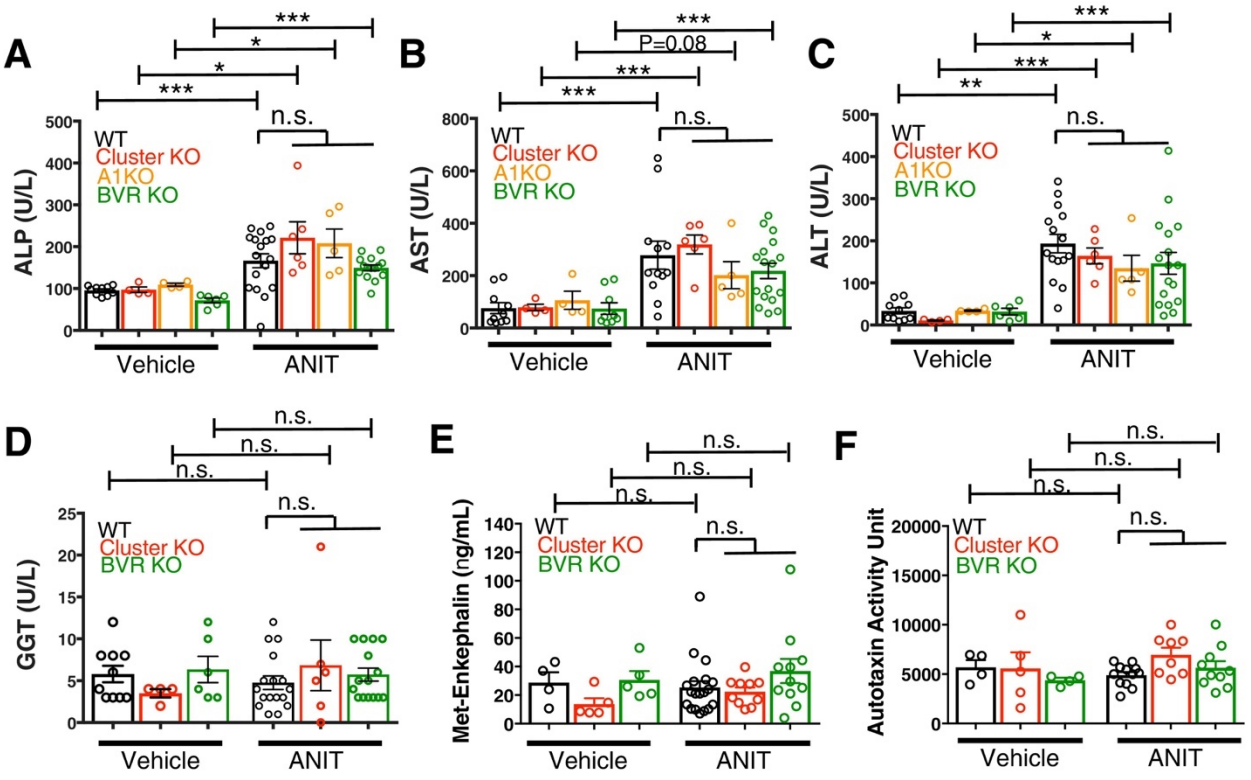

Figure 34. Plasma levels of pathological markers of liver injury are similar between WT, Mrgpr-clusterΔ$^{-/-}$, A1 KO, and BVR KO animals.

a, Plasma alkaline phosphatase (ALP) levels among vehicle and ANIT-treated animals. For vehicle cohort: WT n = 10, Mrgpr-cluster KO n = 4, A1 KO n = 4, BVR KO n = 6. For ANIT cohort: WT n = 17, Mrgpr-cluster KO n = 6, A1 KO n = 5, BVR KO n = 15. **b**, Plasma aspartate aminotransferase (AST) levels among vehicle and ANIT-treated animals. For vehicle cohort: WT n = 10, Mrgpr-cluster KO n = 4, A1 KO n = 4, BVR KO n = 9. For ANIT cohort: WT n = 12, Mrgpr-cluster KO n = 6, A1 KO n = 5, BVR KO n = 17. **c**, Alanine aminotransferase (ALT) levels among vehicle and ANIT-treated animals. For vehicle cohort: WT n = 10, Mrgpr-cluster KO n = 4, A1 KO n = 4, BVR KO n = 6. For ANIT cohort: WT n = 15, Mrgpr-cluster KO n = 6, A1 KO n = 5, BVR KO n = 17. **d**, Gamma-glutamyl transferase (GGT) levels among vehicle and ANIT-treated animals. For vehicle cohort: WT n = 10, Mrgpr-cluster KO n = 4, BVR KO n = 6. For ANIT cohort: WT n = 17, Mrgpr-cluster KO n = 6, BVR KO n = 15. **e**, Met-enkephalin levels among plasma from vehicle and ANIT-treated animals. For vehicle cohort: WT n = 4, Mrgpr-cluster KO and BVR KO n = 5. For ANIT cohort: WT n = 19, Mrgpr-cluster KO n = 10, BVR KO n = 11. **f**, Autotaxin activity among plasma from vehicle and ANIT-treated animals. For vehicle cohort: WT and BVR KO n = 4, Mrgpr-cluster KO n = 5. For ANIT cohort: WT n = 12, Mrgpr-cluster KO n = 8, BVR KO n = 10. (*a-f*) Mean ±s.e.m. depicted. Open circles represent independent data points. *, $p < 0.05$; **, $p < 0.01$, ***, $p < 0.001$; two-tailed unpaired Student's *t*-test. n.s., not significant.

To determine whether bilirubin is activating MRGPRA1 to stimulate itch in cholestasis, we induced cholestasis in a mouse that lacks the biosynthetic enzyme for bilirubin, biliverdin reductase (BVR-/-) (Kutty and Maines, 1981) (**Fig. 26e and Fig. 36a**). Mice lacking BVR do not have detectable levels of bilirubin

in plasma (**Fig. 36b-d**). When treated with ANIT, BVR-/- mice scratched significantly less than WT mice (**Fig. 33c**). Plasma levels of bile acids, ALP, AST, ALT, GGT, met-enkephaline, and autotaxin were indistinguishable between treated BVR-/- animals and WT controls (**Fig. 34a-d**). The diminished response to ANIT is not due to aberrant itch circuits, as BVR-/- mice scratched normally when injected with either chloroquine or exogenous bilirubin (**Fig. 36e-f**).

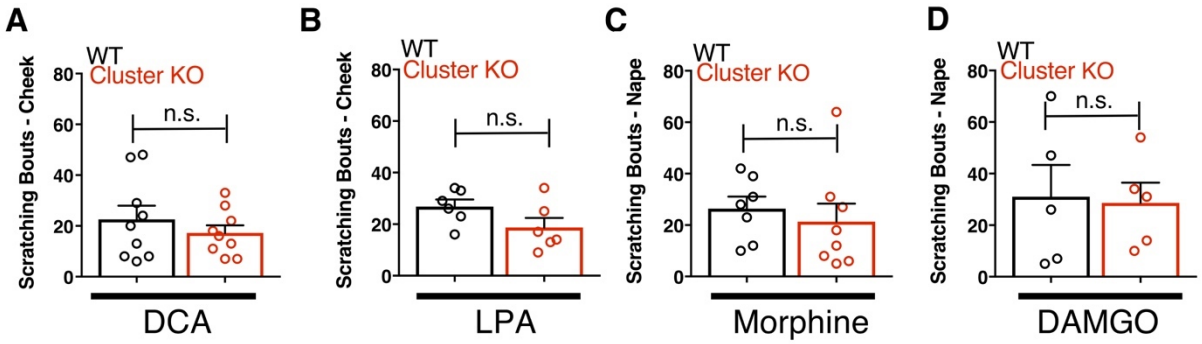

Figure 35. Mrgpr-cluster KO animals have intact itch to other cholestatic pruritogens and bilirubin synergism with chloroquine itch.

a, Scratching bouts to 1.3 mM deoxycholic acid (DCA) injected into cheek. WT n = 9, Mrgpr-cluster KO n = 9. **b**, Scratching bouts to 4 mM lysophosphatidic acid (LPA) injected into cheek. WT n = 6, Mrgpr-cluster$\Delta^{-/-}$n = 6. **c**, Scratching bouts to 25 µg of morphine injected into back. WT n = 7, Mrgpr-cluster$\Delta^{-/-}$n = 8. **d**, Scratching bouts to 25 µg of DAMGO injected into back. WT n = 5, Mrgpr-cluster KO n = 5. **e**, Synergism of bilirubin with chloroquine pruritus. Scratching bouts to 1 mM chloroquine plus either vehicle or 500 µM bilirubin injected into back. For 1 mM chloroquine plus vehicle: WT n = 9, A1 KO n = 5. For 1 mM chloroquine plus 500 µM bilirubin: WT n = 11, A1 KO n = 5. (*a-e*) Mean ±s.e.m. depicted. Open circles represent independent data points. **, $p < 0.01$, ***, $p < 0.001$; two-tailed unpaired Student's *t*-test. n.s., not significant.

To confirm that the observed differences in cholestatic pruritus were not just specific to ANIT, we administered the hepatotoxin cyclosporin A to WT, A1-/-, and BVR -/- mice (Laupacis et al., 1981). We treated mice with either 50 mg/kg cyclosporin A or vehicle for eight days before assessing spontaneous itch (**Fig. 33f**). Cyclosporin A induced spontaneous itch in WT animals, whereas A1-

/- and BVR -/- mice again scratched significantly less than WT mice (**Fig. 33g-h**).

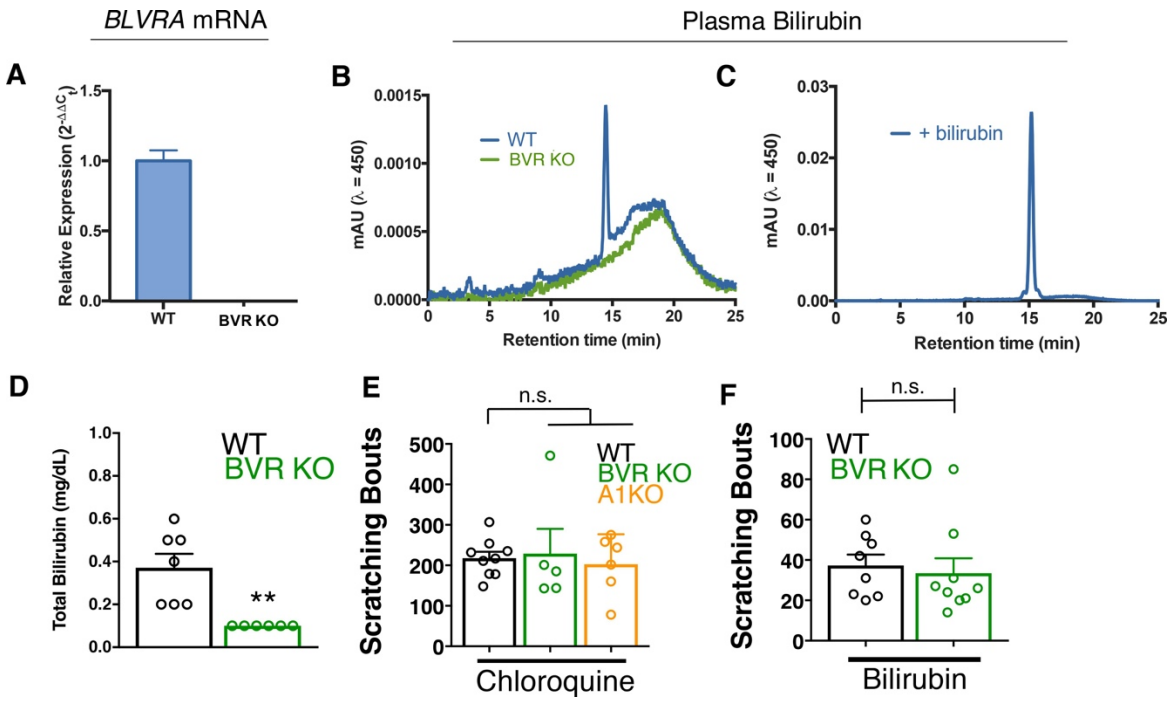

Figure 36. BVR KO and A1 KO animals have intact itch circuits.

a, Quantitative PCR analysis of *BLVRA* transcript from whole brain of WT and BVR KO mice. **b**, Representative chromatogram of HPLC analysis of plasma from WT and BVR KO mice separated via a C18 column and analysed by absorbance at 450 nm. **c**, HPLC chromatogram of plasma from a WT mouse spiked with excess bilirubin. **d**, Total bilirubin levels from plasma of WT and BVR KO animals. WT n = 7, BVR KO n = 6. **e**, Scratching bouts to 150 µg (50 µL of 10 mM) of chloroquine. After chloroquine injection, scratching bouts were assessed in a 30 min period. WT n = 9, BVR KO n = 5, A1 KO n = 6. **f**, Scratching bouts to 60 µg (100 µL of 1 mM) of bilirubin. After bilirubin injection, scratching bouts were assessed in a 30 min period. WT n = 8, BVR KO n = 9. (*d-f*) Mean plus S.E.M. depicted. Open circles represent independent data points. **, $p < 0.01$ by student's t-test. n.s., not significant.

Notably, we found that plasma bilirubin correlates poorly with cholestatic itch in patients and in cholestatic animals (**Fig. 33i**). We hypothesized that the levels of bilirubin in the skin would correlate better with itch than serum bilirubin largely because bilirubin likely binds and activates the sensory neurons in the skin. Unlike with serum, skin bilirubin appears to be a much stronger

predictor of itch severity in mice (**Fig. 33j**). This is consistent with how the anatomical distribution of itch sensory neurons and may explain why studies aimed at identifying plasma pruritogens that correlate with itch severity may have missed bilirubin. Secondarily, we find that plasma bilirubin does not correlate well with skin bilirubin, further suggesting that plasma bilirubin may be a poor predictor of itch severity and may not necessarily serve as a proxy for

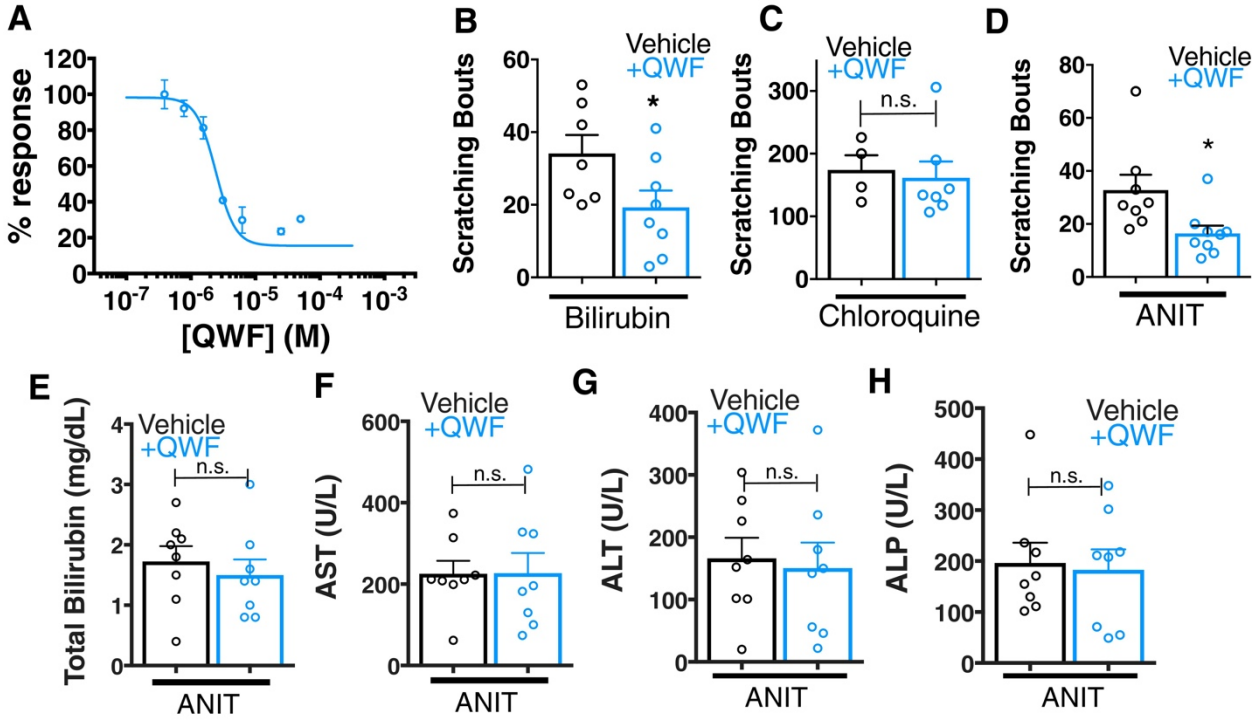

Figure 37. QWF treatment blocks bilirubin activation of Mrgpra1 and cholestatic pruritus.

a, Concentration-response curve for bilirubin induced Ca^{2+} signal in MRGPRA1-expressing HEK cells. 200 μM bilirubin was maintained in competition with indicated doses of QWF. Mean ±s.e.m. depicted. n = 3 replicates in duplicate. **b-c**, Scratching bouts from (*b*) 60 μg (100 mL of 1 mM) bilirubin or (*c*) 150 μg chloroquine co-injected with either vehicle or 1 mg/kg QWF. After injection, the number of scratching bouts in 30 min was assessed. For bilirubin: Vehicle n = 7, QWF n = 8. For chloroquine: Vehicle n = 4, QWF n = 7. **d**, Scratching bouts from WT ANIT-treated animals. Either vehicle or 1 mg/kg QWF was delivered *i.p.* Vehicle n = 8, QWF n = 9. **e-h**, Plasma (*e*) bilirubin, (*f*) AST, (*g*) ALT, and (*h*) ALP levels from of vehicle and QWF-dosed WT animals that have undergone ANIT liver injury. (*b–h*) Mean ±s.e.m. depicted. Open circles represent independent data points. n.s., not significant; *, $p < 0.05$ by two-tailed unpaired Student's *t*-test.

skin bilirubin (**Fig. 33k**). The amount of bilirubin in the skin is likely affected by several factors and equilibria, such as serum albumin.

We assessed whether pharmacologically antagonizing MRGPRs could alleviate cholestatic itch. Recently, a 3-amino acid peptide, QWF, was identified as an MRGPRA1 antagonist (Azimi et al., 2016). QWF abolished bilirubin-associated calcium signaling in MRGPRA1-expressing cells with an IC_{50} of 2.9 μM [1, 5] (**Fig. 37a**). Mirroring its pharmacology *in vitro*, co-injecting 0.25 mg/kg QWF with bilirubin significantly alleviated pruritus associated with bilirubin (**Fig. 37b**). QWF specifically antagonized bilirubin, as it did not attenuate chloroquine-MRGPRA3 associated itch (**Fig. 37c**). Lastly, we evaluated whether the MRGPRA1 antagonist QWF could alleviate cholestatic pruritus. We dosed WT animals with ANIT as previously described, but intraperitoneally injected mice with either vehicle or 1 mg/kg QWF thirty minutes prior to behavioral analysis. Mice treated with QWF scratched significantly less than vehicle-treated animals (**Fig. 37d**). QWF treatment did not change plasma levels of total bilirubin, AST, ALT, or ALP, suggesting that QWF treatment did not alter the underlying liver pathology (**Fig. 37e-h**).

Bilirubin from mouse and human cholestatic plasma contributes to pruritus in a Mrgpra1-dependent manner

Nasobiliary drainage is the most effective treatment for cholestatic pruritus (Hegade et al., 2016). Based on this clinical observation, we predicted that plasma isolated from cholestatic animals would elicit pruritus (**Fig. 38a**). Indeed,

plasma from WT animals with cholestasis elicited itch when injected into naïve WT animals (**Fig. 38b**). Cholestatic plasma isolated from BVR -/- mice, which lacks bilirubin (**Fig. 36b-d**), elicited significantly fewer scratches than WT cholestatic plasma (**Fig. 38b**). The levels of ALP, AST, and ALT were indistinguishable between WT and BVR -/- cholestatic plasma (**Fig. 34a-d**), presumably because ANIT induced similar hepatotoxicity in WT and BVR -/- mice. Instead, BVR -/- plasma likely results in less pruritus because it lacks bilirubin.

We also isolated plasma from six patients suffering from various conditions that result in hyperbilirubinemia and six age- and sex-matched control patients (**Fig. 38c-g**). All six cholestatic patients' plasma evoked itch in WT animals (**Fig. 38d**). When injected into A1 -/- animals, each patient's plasma elicited less itch (**Fig. 38d**). Compared to plasma from itchy patients, plasma from healthy donors (six tested) which have low level of bilirubin elicited less itch in WT animals (**Fig. 38c**). When injected into A1 -/- animals, we observed no differences in scratching behavior (**Fig. 38c**). To assess whether removing bilirubin from cholestatic plasma may be therapeutic, we depleted bilirubin both by selective oxidation with $FeCl_3$ or an anti-bilirubin antibody before evaluating its pruritic capacity. We verified depletion of bilirubin by HPLC (**Fig. 39a-b**). Injecting WT mice with plasma (cholestatic patients 1 and 4) treated with $FeCl_3$ or an anti-bilirubin antibody evoked less pruritus compared to untreated or control IgG-treated patient plasma (**Fig. 38h-i**).

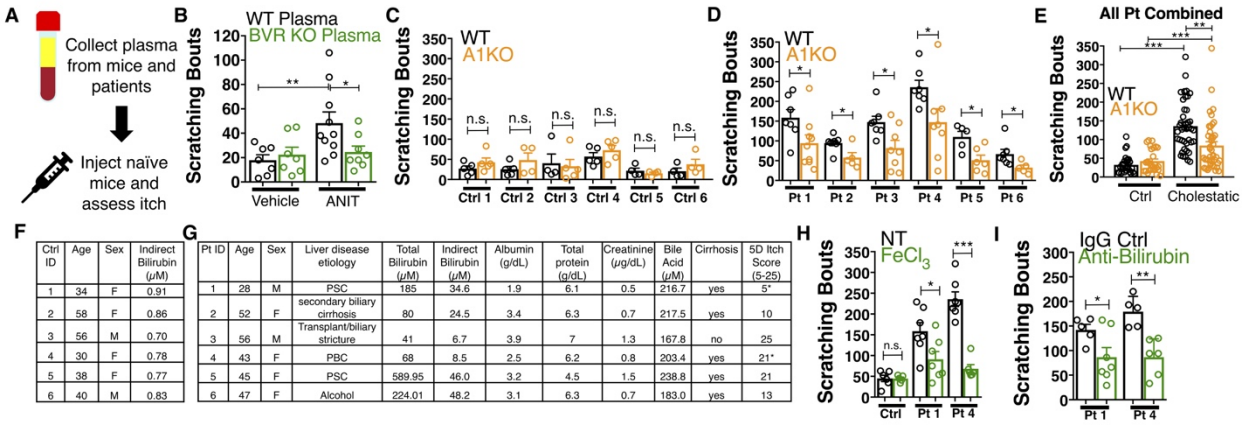

Ctrl ID	Age	Sex	Indirect Bilirubin (μM)
1	34	F	0.91
2	58	F	0.86
3	56	M	0.70
4	30	F	0.78
5	38	F	0.77
6	40	M	0.83

Pt ID	Age	Sex	Liver disease etiology	Total Bilirubin (μM)	Indirect Bilirubin (μM)	Albumin (g/dL)	Total protein (g/dL)	Creatinine (μg/dL)	Bile Acid (μM)	Cirrhosis	5D Itch Score (5-25)
1	28	M	PSC	185	34.6	1.9	6.1	0.5	216.7	yes	5*
2	52	F	secondary biliary cirrhosis	80	24.5	3.4	6.3	0.7	217.5	yes	10
3	56	M	Transplant/biliary stricture	41	6.7	3.9	7	1.3	167.8	no	25
4	43	F	PBC	68	8.5	2.5	6.2	0.8	203.4	yes	21*
5	45	F	PSC	589.95	46.0	3.2	4.5	1.5	238.8	yes	21
6	47	F	Alcohol	224.01	48.2	3.1	6.3	0.7	183.0	yes	13

Figure 38. Bilirubin from mouse and human cholestatic plasma contributes to pruritus in an Mrgpra1-dependent manner.

a, Experimental flowchart of plasma injection assay. **b**, Scratching bouts from WT mice injected with either vehicle- or ANIT-treated plasma from WT and BVR KO animals. For the vehicle plasma cohort: n = 7. For cholestatic ANIT-treated plasma: WT n = 10 and BVR KO n = 8. **c**, Scratching bouts from either WT or A1 KO mice injected with control donor plasma. Ctrl 1, WT n = 5, A1 KO n = 5. Ctrl 2, WT n = 5, A1 KO n = 5. Ctrl 3, WT n = 5, A1 KO n = 4. Ctrl 4, WT n = 4, A1 KO n = 5. Ctrl 5, WT n = 4, A1 KO n = 4. Ctrl 6, WT n = 4, A1 KO n = 4. **d**, Scratching bouts from either WT or A1 KO mice injected with either cholestatic patient plasma. Patient 1, WT n = 7, A1 KO n = 9. Patient 2, WT n = 8, A1 KO n = 5. Patient 3, WT n = 7, A1 KO n = 8. Patient 4, WT n = 6, A1 KO n = 8. Patient 5, WT n = 5, A1 KO n = 6. Patient 6, WT n = 7, A1 KO n = 5. **e**, Scratching bouts from either WT or A1 KO mice injected with plasma collected from all tested control donor samples and all tested cholestatic patient samples. For Control: WT n = 27, A1 KO n = 27. For cholestatic patient: WT n = 41, A1 KO n = 41. **f–g**, Biochemical characteristics of patient and control plasma. **f**, Age, sex, and bilirubin levels of control plasma collected. All control plasma donors did not suffer from any chronic itch condition. **g**, 5D itch questionnaire was administered at time of plasma collection. Asterisk denotes patients taking anti-pruritic medication at time of plasma collection and questionnaire administration. Patient one was taking sertraline (100 mg QD) and Patient four was taking Gabapentin (800 mg TID). A score of 25 represents the maximum level of itchiness. **h**, Scratching bouts from mice injected with either untreated (NT) control human plasma, $FeCl_3$-treated control human plasma, NT cholestatic patient 1 and 4 plasma (same data from Patient WT data in (*d*), or $FeCl_3$-treated patient plasma. For control plasma, NT n = 6 and $FeCl_3$n = 5. For Patient one plasma, NT n = 7 and $FeCl_3$n = 7. For Patient four plasma, NT n = 7 and $FeCl_3$n = 6. **i**, Scratching bouts from mice injected with either normal rabbit IgG –treated patient plasma or anti-bilirubin IgG – treated patient plasma. For Patient 1, Normal IgG n = 5, Anti-bilirubin n = 7. For Patient 4, Normal IgG n = 5, Anti-bilirubin n = 6. (*b–i*) Mean ±s.e.m. depicted. Open circles represent independent data points. n.s., not significant; *, p<0.05; **, p<0.01; ***, p<0.001 by unpaired two-tailed Student's t-test.

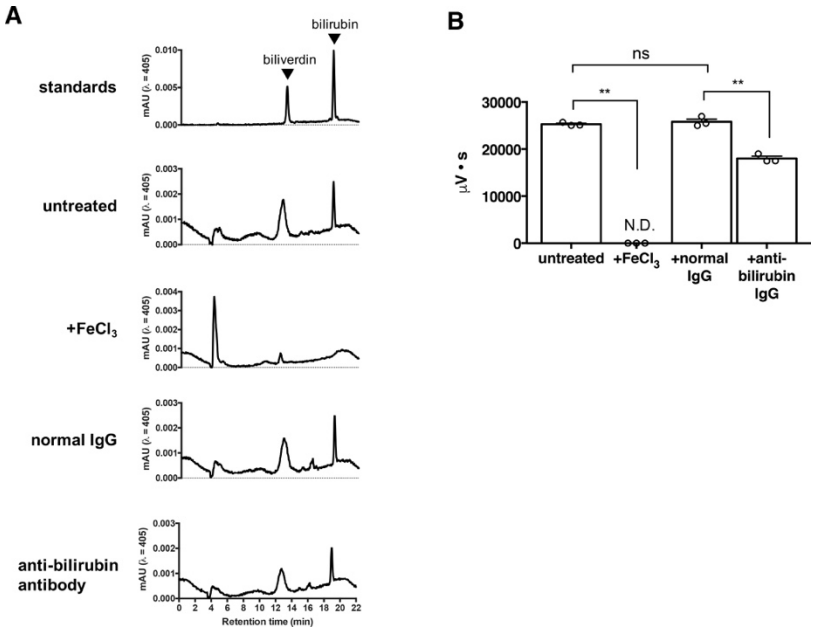

Figure 39. $FeCl_3$ and anti-bilirubin antibody depletion of plasma bilirubin.

a, Representative HPLC chromatogram of 100 μM biliverdin +100 μM bilirubin standards and treated plasma samples. Absorbance was measured at 405 nm. **b**, Quantification of plasma bilirubin in untreated, $FeCl_3$, normal rabbit IgG, and bilirubin antibody-treated samples. Points represent technical replicates. Mean ±s.e.m. depicted **, $p<0.01$; n.s., not significant by two-way ANOVA followed by *post-hoc* Tukey test.

Discussion

To date, bilirubin has either been considered a neonatal neurotoxin or an inert biomarker in disease. Our results reveal that bilirubin itself is a pruritogen that evokes itch by binding and activating MRGPRs on sensory neurons and may be an overlooked source of some patients' unrelenting itch. The K_D of bilirubin towards MRGPRA1 and MRGPRX4 suggests that bilirubin likely only interacts and activates these receptors in individuals with markedly elevated bilirubin and not in healthy people. More narrowly in hepatobiliary diseases such as cholestasis, our data supports a model in which bilirubin is one of several pruritogens that contributes to itch. Specifically, we find that genetically

removing either MRPGRA1 ($A1^{-/-}$) or bilirubin ($BVR^{-/-}$) both strongly attenuated itch. However, these mutant mice still exhibit greater itch compared to untreated mice. This suggests that other pruritogens contribute to itch alongside bilirubin in hepatobiliary disease, consistent with the diverse and complex presentations of patients suffering from conditions such as chronic pruritus. Other responsible pruritogens could include bile acids, endogenous opioids, and LPA. While depleting bilirubin in jaundiced patients like in mice may be effective in reducing itch, not every patient who suffers from hepatobiliary pruritus is jaundiced. Accordingly, identifying and depleting other pruritogens may similarly reduce itch.

Although our findings directly illustrate that bilirubin is pruritic, it is also clear that not every patient with jaundice experiences itch. For example, patients with genetic hyperbilirubinemias such as Dubin-Johnson syndrome, a disorder involving mutations in the bilirubin transporter ABCC2, or Crigler-Najjar Type 1, a disorder involving mutations in the bilirubin glucuronosyltransferase UGT1A1, rarely complain of pruritus (Levitt and Levitt, 2014; Van Der Veere et al., 1996). Moreover, neonates can have high levels of bilirubin in their skin but not itch. Bilirubin thus appears to exert selective pruritic activity in certain contexts, which we hypothesize may derive from its dynamic biophysical behavior and complex network of interactions.

In isolated genetic hyperbilirubinemias, few – if any – other organic metabolites are elevated. In contrast, several other metabolites are elevated in addition to bilirubin in cholestasis, many of which may alter the equilibrium

between bilirubin and albumin (Alemi et al., 2013; Jacobsen and Broderson, 1983; Kalir et al., 1990; Kozaki et al., 1998). Moreover, bilirubin's affinity for albumin and other lipoproteins is disrupted by numerous agents in bile that are upregulated specifically in cholestasis. Bilirubin also exhibits distinct chemical behavior in cholestatic serum, and several groups have suggested that bile acids affect bilirubin's solubility and conformation (Ostrow and Celic, 1984; Rege et al., 1988). Accordingly, it is reasonable to speculate that bilirubin is more likely bound to albumin in isolated hyperbilirubinemias than in cholestasis, and is therefore less likely to enter the skin in conditions like Dubin-Johnson. Notably, a predictive metrics for cholestatic pruritus is the Mayo risk score, which considers both serum bilirubin and albumin levels (Talwalkar et al., 2003). The Mayo risk score predicts that itch burden increases with increasing bilirubin and decreasing albumin levels; in such circumstances, bilirubin is less likely bound to albumin and is free to enter other tissues such as the skin. Crigler-Najjar patients may be even less likely to complain of itch than Dubin-Johnson patients because the standard treatments for Crigler-Najjar (phenobarbital and light therapy) may directly interfere with bilirubin's pruritic activity. Specifically, light therapy induces photoisomerization and/or photolysis of bilirubin, which alter its structure and activity. Phenobarbital itself acts by broadly decreasing neural excitability, and may dampen itch circuitry alongside other central nervous system circuits. Notwithstanding these questions, our results suggest that blocking MRGPRX4 may offer relief to those suffering from jaundice and/or cholestatic-associated pruritus.

Materials and methods

Experimental Model and Subject Details

Mice

Animal care and use

All experiments were performed in accordance with protocols approved by the Animal Care and Use Committee at the Johns Hopkins University School of Medicine.

Generation of knock-in and knock-out mice

Mrgpr-clusterΔ$^{-/-}$ mice, *Mrgpra1*^{GFP} mice, and *Mrgprd*^{PLAP} were generated as previously described (Dong et al., 2001; Liu et al., 2009; 2007). Tg(*Mrgpra3-Cre*) mice were generated as previously described (Han et al., 2012). Tg(*Pirt-Cre*) mice were generated as previously described via homologous recombination (Kim et al., 2014).

Rosa26-LoxP-STOP-LoxP (lsl)-GCaMP6s mice were purchased from Jackson Labs. Lsl-tdTomato mice (Ai9, 007909) were purchased from Jackson Labs.

Mrgpra1$^{-/-}$ mice were generated using CRISPR-Cas9 on the C57BL/6 background using the following guide RNA sequence: TTCCCAGCAGCACCTGTGCAGGG. *Blvra*$^{-/-}$ mice were generated at Ozgene (Australia) on a C57BL/6J background.

Age-matched wild-type C57BL/6J mice were used as controls.

Human plasma

Plasma from patients suffering from hyperbilirubinemia, specifically cholestasis, was isolated under a protocol approved by the Institutional Review Board at the Johns Hopkins University School of Medicine (Study number: IRB00154650). Control plasma was isolated from donors who did not exhibit kidney or liver disease, had no complaints of itch, and were free from any detectable viral infection (HCV, HBV, HIV). Both cholestatic and control plasma were isolated under protocols approved by the Institutional Review Board at the Johns Hopkins University School of Medicine (Cholestasis Study number: IRB00154650; Control study number: NA_00013177, the Johns Hopkins Department of Dermatology Patient Database and Tissue Bank). Whole blood was collected into PAXgene tubes (PreAnalytiX 761115) and centrifuged for 5 minutes at 300g. Plasma was then collected, aliquoted, and stored at -20°C until experimentation. At time of plasma collection, a 5D itch questionnaire was administered.

Cell culture

DRGs

DRG neurons from all spinal levels were collected in cold DH10 media (90% Dulbecco's modified Eagle's medium (DMEM)/F-12, 10% FBS, penicillin (100 U/mL), and streptomycin (100 µg/mL)). DRGs were digested with a dispase (5 mg/ml)/collagenase type I (1 mg/ml) enzyme mixture at 37°C for 45 minutes.

After trituration, cells were spun at 300*g* and re-suspended in DH10 before being plated on glass coverslips coated with poly-D-lysine (0.5 mg/ml) and laminin (10 µg/ml, Invitrogen). DRGs were cultured with DH10 supplemented with 50 ng/mL NGF at 37°C.

HEK293

Human embryonic kidney 293 (HEK293) cells were cultured in DMEM (Gibco) supplemented with 10% FBS, 100 U/mL penicillin and streptomycin, and 2 mM glutamine at 37°C with 5% CO_2.

Method Details

Materials and preparation

Solvents and compounds were obtained as follows:

The following molecules were used: bilirubin IXα (Frontier Scientific). α-naphthyl isothiocyanate (ANIT, Sigma), biliverdin (Sigma), chloroquine (Sigma), compound 48/80 (Sigma), cyclosporin A (Sigma), hemin (Sigma), human serum albumin (HSA, Sigma), BAM8-22 (Sigma), BOC-GLN-D-(FORMYL)TRP-PHE-BENZYLESTER (QWF, Sigma), bilirubin ditaurate (Lee Biosciences). cetirizine (Tocris Biosciences), stercobilin (Santa Cruz Biotechnology), urobilinogen (Santa Cruz Biotechnology), FMRF peptide (Sigma), cholera toxin (Santa Cruz Biotechnology), U73122 (Santa Cruz Biotechnology), YM-254890 (Wako Chemicals), pertussis toxin (Fisher Scientific), fibronectin (Sigma), ruthenium red (Sigma), Fluo 4-AM (Molecular Probes), and Fura 2-AM (Molecular Probes)

Material preparation:

Bilirubin is highly susceptible to oxidation and photolysis. Accordingly, bilirubin was freshly prepared just prior to each experiment in either DMSO or 0.1 M NaOH and then maintained in the dark. For calcium imaging analyses, bilirubin was diluted into calcium imaging buffer a few seconds before use. Final concentration of DMSO in all applicable tested solutions was < 0.5%. ANIT and cyclosporin A were dissolved in olive oil and prepared freshly as needed. Urobilinogen and stercobilin were dissolved in phosphate buffered saline and adjusted to a pH of 7.4 before being stored at -20°C in 100 μl aliquots until needed. To maintain the integrity of bilirubin in human plasma samples, samples were stored at -80°C until use. Plasma stocks were maintained in the dark to minimize photolysis during injection or experimental manipulation. Plasma bilirubin was evaluated by HPLC as described above. All other drugs were prepared as 100 μl – 1,000 μl aliquots and stored at -20°C before thawing at 4°C. Freeze/thaw cycles were avoided whenever possible. To remove microprecipitates, we centrifuged our bilirubin solutions at 21,000g for 20 min to ensure that bilirubin was in solution. Whenever physiologically and experimentally reasonable, we excluded divalent cations in our in vitro biophysical experiments.

Behavioral studies

All applicable behavioral tests were performed and analysed with the experimenter blind to genotype. All mice used were 8-12 week old males and

females (20 to 30 g) that had either been generated on a C57BL/6J background or backcrossed to C57BL/6J mice for at least 10 generations. There were no significant differences in itch between male and female mice. All itch behavior experiments were performed between 8 a.m. and 12 p.m. On the day before the experiment, animals were placed in the test chamber for 30 minutes before being subjected to a series of three mock injections with 5-minute break periods in between. On the day of the experiment, animals were first allowed to acclimatize to the test chamber for 10 minutes before injection. Pruritic compounds were subcutaneously injected into the nape of the neck (50μL volume) or cheek (10μL volume), and scratching behavior was observed for 30 minutes. A bout of scratching was defined as a continuous scratching movement with either hindpaw directed at the area of the injection site. In the cheek injection model, a wipe was defined as a single forepaw stroking the site of the injection. Use of both forepaws on the face or cheek was considered as grooming behavior. Scratching behavior was quantified by counting the number of scratching bouts at 5 min intervals over the 30-min observation period. Wiping was quantified at 2 min intervals over a ten-minute observation period. For H1R block, 30 mg/kg of cetirizine HCl (pH 7.4) was given intraperitoneally thirty minutes prior to injection of bilirubin. Licking behavior was quantified in seconds and identified as the licking of the toes or footpad of the hind paw site of injection that was neither preceded nor followed by licking of any other portion of the body. For QWF co-injection experiments, either 100 μM (for bilirubin) or 500 μM (for chloroquine) QWF was injected in the same volume as solubilized pruritogen.

Quantum mechanical calculations

DFT calculations were performed with Spartan 16 and modelled with wxMacMolPlt. Geometry optimizations and single point energy calculations were carried out with DFT-Hartree Fock hybrid B3LYP theory with the 6-31G(d) basis set. Energies were calculated at ground state in the gas phase 298 K.

Calcium imaging and analysis

Cells were imaged in calcium imaging buffer (CIB; 10 mM HEPES, 1.2 mM $NaHCO_3$, 130 mM NaCl, 3 mM KCl, 2.5 mM $CaCl_2$, 0.6 mM $MgCl_2$, 20 mM glucose, and 20 mM sucrose at pH 7.4 and 290-300 mOsm). To monitor changes in intracellular $[Ca^{2+}]$ ($[Ca^{2+}]_i$), cells were loaded with either Fura 2-AM (HEK293 cells) or Fluo 4-AM (DRG neurons and mast cells) for 30 min in the dark at 37°C in CIB just prior to imaging. With Fura 2-AM, emission at 510 nm was monitored from excitation at both 340 nm and 380 nm. With Fluo 4-AM, emission at 520 nm was monitored from excitation at 488 nm. Cells were identified as responding if the intracellular $[Ca^{2+}]$ rose by either 50% compared to baseline or 50% compared to the $[Ca^{2+}]_i$ change assayed during addition of 50 mM KCl (neurons only). Damaged, detached, high-baseline, and motion-activated cells were excluded from analysis.

HEK293 cells

In initial screens, HEK293 cells stably expressing the murine G-protein alpha-subunit $G_{\alpha 15}$, a unique G_{α} protein that non-selectively couples a large variety of GPCRs to phospholipase C [30], were plated on poly-D-lysine-coated coverslips and transiently transfected with constructs encoding the MRGRPR of interest. 12-24 h later, cells were loaded with the Fura 2-AM. Unless otherwise specified, compounds were perfused into the imaging chamber for approximately thirty seconds after a baseline period was established. Response was then monitored at 5 s intervals for an additional 60 s.

DRG neurons

DRGs were incubated with Fluo-4 AM 24 hour after dissociation (native genotype) or 48 hour after dissociation (virally transduced). Unless otherwise noted, cells were imaged for 20 sseconds to establish a baseline before compounds were added. After 30 s, a 2 min wash was applied before addition of another substances. At the end of every imaging trial, 50 mM KCl was added as a positive control. Cells included in calculating percentages all displayed at least a 50% increase in $[Ca^{2+}]_i$ compared to baseline upon addition of KCl. For ruthenium red inhibitor experiments, neurons were incubated with 10 μM ruthenium red for 5 minutes prior to imaging. Percentage activated was determined as earlier described.

Mast cells

Mast cells were purified as described and plated onto glass coverslips coated with 30 mg/mL fibronectin and allowed to recover for 2 h at 37°C. Cells were then loaded with Fluo-4 AM.

EC_{50} and IC_{50} determinations

HEK293 cells stably expressing either MRGPRA1, MRGPRX4, and MRGRPC11 were seeded in poly-D-lysine-coated 96-well plates at 10,000 cells/well. Cells were loaded with Fura 2–AM, washed twice, and maintained in CIB. Haem metabolites were freshly dissolved in DMSO in dim light and then diluted into a buffer comprised of 20 mM Tris and 150 mM NaCl at pH 8.8. Potential changes in pH were evaluated prior to each experiment. EC_{50} values were determined from dose-responses performed in triplicate, repeated 2-4 times. To determine potential antagonism by QWF against bilirubin, cells were treated with varying doses of QWF for 1 min in CIB prior to application of agonist.

Murine peritoneal mast cell purification and calcium imaging.

Adult male mice 8–12 weeks of age were sacrificed through CO_2 inhalation. A total of 25 mL of mast cell dissociation media (MCDM; HBSS with 3% fetal bovine serum and 10 mM HEPES, pH 7.2) was chilled on ice before being used to make two sequential peritoneal lavages. Lavages were combined and spun at 200*g*. The pellet was re-suspended in 2 mL MCDM, layered over 4 ml of an isotonic 70% Percoll suspension (2.8 ml Percoll, 320 ml 10% HBSS, 40 ml 1 M HEPES, 830 ml MCDM), and spun for 20 min at 500*g* at 4°C. Mast cells were recovered in the

pellet. Mast cells were re-suspended in DMEM with 10% fetal bovine serum (FBS) and 25 ng/mL recombinant mouse stem cell factor (Sigma).

Mouse peritoneal mast cell histamine release assay

Mast cells were purified as described and allowed to recover for 2 h at 37°C. Cells were then seeded in 96-well plates coated with 20 mg/mL fibronectin at 300 cells/well. Plates were incubated at 37°C for 45 min before assay. For the assay, all compounds tested were diluted in CIB. Five minutes after compound addition, supernatant was aspirated and frozen at -80°C until histamine levels were determined with an HTRF histamine assay kit (Cisbio Assays) according to the manufacturer's instructions.

Generation of cells stably expressing GFP-tagged MRGPRs

HEK293 stable cell lines expressing GFP-tagged MRGPRA3, MRGPRC11, MRGPRD, MRGPRX1, and MRGPRX2 were generated in previously described reports (Liu et al., 2009; 2012; McNeil et al., 2015). Briefly, plasmids containing the receptor of interest were transfected into HEK cells using Lipofectamine 3000. After 3 days, cells were then selected using 0.5 mg/mL G418. After 3 weeks, monoclonal colonies were established and each the highest expressing clones were identified. For this study, *Mrgpra1* and *MRGPRX4* were inserted into pEGFP-N1 and transfected into HEK293 cells. MRGPR-positive cells were selected using 0.5 mg/mL G418 for three weeks, after which GFP-positive cells were sorted by FACS and monoclonally expanded. Two lines expressing similar

levels of MRGPRA1 and MRGPRX4, as measured by GFP fluorescence, were selected for study.

Microscale thermophoresis binding

Binding isotherms for MRGPRA1, MRGPRX4, and MRGRPC11 towards various ligands were determined by microscale thermophoresis with the NanoTemper monolith NT.115 instrument (Duhr and Braun, 2006). Ligands were pre-incubated with 10 μM of the GFP-tagged receptor of interest for 5 minutes at room temperature in binding buffer (20 mM Tris and 150 mM NaCl at pH 8.8). Receptors were crudely purified as a membrane fraction from cells stably expressing the receptor (Vasavda et al., 2017). Haem metabolites were freshly dissolved in 0.1 M NaOH in dim light and then diluted into assay buffer. Lyophilized BAM8-22 was dissolved in binding buffer. The pH of each ligand was evaluated prior to incubation with a receptor. Samples were loaded into NT.115 Hydrophobic-Treated Capillaries from NanoTemper. Microscale thermophoretic experiments were executed using 20% LED power and 15% MST power. K_Ds were calculated using the law of mass action with data from three independent experiments. Binding between bilirubin and receptors was evaluated purely thermophoretically, whereas binding between BAM8-22 and MRGPRC11 was evaluated by T-Jump. Samples with dramatic deviations in initial fluorescence were excluded.

[^{35}S]GTPγS binding

MRGPR activation was determined by measuring binding of a radiolabelled and non-hydrolyzable form of GTP, [^{35}S]guanosine-5'-(γ-thio)triphosphate ([^{35}S]GTPγS) as previously described (Vasavda et al., 2017). Briefly, 10 µg of crude membrane fractions were diluted into 175 µL assay buffer (50 mM HEPES, 5 mM $MgCl_2$, 100 mM NaCl, 1 mM EDTA, 0.1% Triton 80) supplemented with 10 µM GDP and incubated at room temperature for 5 min. Membranes were then incubated an additional 1 min in a final volume of 199 µL assay buffer supplemented with 50 µM bilirubin. Samples were then brought to 200 µL with the addition of 10 nM [^{35}S]GTPγS. Samples were incubated for 2 h at 4°C with gentle agitation. The experiment was terminated by rapid filtration onto GF/B filters and washed three times with wash buffer (50 mM Tris-HCl, 5 mM $MgCl_2$, and 50 mM NaCl at pH 7.4). Filters were then immersed in scintillation cocktail and counted. Nonspecific binding was determined by competition with 10 µM unlabelled GTPγS. GTPγS binding assays were performed as two independent experiments, in triplicate.

DRG dissociation and culture

DRG neurons from all spinal levels were collected in cold DH10 media (90% Dulbecco's modified Eagle's medium (DMEM)/F-12, 10% FBS, penicillin (100 U/mL), and streptomycin (100 µg/mL)). DRGs were digested with a dispase (5 mg/ml)/collagenase type I (1 mg/ml) enzyme mixture at 37°C for 45 minutes. After trituration, cells were spun at 300*g* and re-suspended in DH10 before being plated on glass coverslips coated with poly-D-lysine (0.5 mg/ml) and laminin (10

μg/ml, Invitrogen). DRGs were cultured with DH10 supplemented with 50 ng/mL NGF at 37°C.

DRG viral transduction

Lentiviruses encoding various cDNA for MRGPRs were generated using psPAX2 and pMD2.G. Virus was pelleted by centrifugation at 100,000*g* for 4 h, gently washed with twice with DH10 media, and suspended in DH10. One day after DRG isolation and culture, DRGs were infected with lentivirus 24 h overnight. The following morning, media was completely replaced with fresh DH10 supplemented with 50 ng/mL NGF. 24 h after infection, cells were processed for calcium imaging.

DRG electrophysiology

DRG neurons from 3-5 week old mice were collected as described. After culture for 1-3 days, DRG neurons were transferred into a chamber with extracellular solution containing (in mM) 144 NaCl, 2.5 KCl, 2 CaCl2, 0.5 MgCl2, 5 HEPES, and 10 glucose, adjusted to pH 7.4 with NaOH. Whole-cell current-clamp recordings were performed at ~23°C using borosilicate capillary glass electrodes (Sutter Instrument) with a tip resistance of 3-5 MΩ. Internal solution contained (in mM) 80 K-acetate, 30 KCl, 40 HEPES, and 1 CaCl2, adjusted to pH 7.4 with potassium hydroxide (KOH). Small-diameter neurons with diameter 15-25μm were chosen for patch-clamp. Data were acquired using an Axopatch 700B Amplifier and Digidata 1322A Digitizer with pClamp9.2 software package (Axon

Instrument). Chloroquine (CQ) in 1mM was added by perfusion for 20 seconds, and bilirubin freshly made in 50μM was added by pipette. Solutions containing 50mM KCl were applied at the end of each cellular recording. Only neurons that could fire action potentials after adding KCl were regarded as healthy and appropriate for inclusion in data analysis.

Immunohistochemistry

Adult mice (5-6 weeks old) were anesthetized by i.p. injection of chloral hydrate (20 μl /gram of 25mg/ml solution) and perfused with 30 ml 0.1 M phosphate buffered saline (PBS) (pH 7.4, 4 °C) followed with 30 ml of fixative (4% paraformaldehyde (vol/vol), 4 °C). Skin, trigeminal ganglia, dorsal root ganglia, and spinal cord were dissected from the perfused mice. Tissues were post-fixed in fixative at 4° for 2 h. Tissues were cryoprotected in 20% sucrose (wt/vol) for up to 8 h followed by 30% sucrose for 24 h and then sectioned (25 μm width) with a cryostat. The sections were dried at 37°C on slides for 1 h and fixed with 4% paraformaldehyde at 21–23 °C for 10 min. The slides were pre-incubated in blocking solution (10% normal goat serum (v/v), 0.2% Triton X-100 (v/v) in PBS, pH 7.4) for 1 h at 21–23 °C, then incubated overnight at 4 °C with primary antibodies. Secondary antibody incubation was performed at 21–23 °C for 2 h. For primary antibodies, we used rabbit antibody to CGRP (T-4239, Peninsula, 1:1,000), rabbit antibody to GFP (A-11122, Molecular Probes, 1:1,000), and Substance P (rat monoclonal from Abcam, 1:250 dilution, M09205). For secondary antibodies, we used goat antibody to rabbit (A11011, Alexa 568

conjugated; A11008, Alexa 488 conjugated; Molecular Probes) and Invitrogen 547 (A-21247) for Substance P, all diluted 1:500 in blocking solution. To detect IB4 binding, sections were incubated with Griffonia simplicifolia isolectin GS-IB4 Alexa 568 from Invitrogen at 1:500 dilution (I-21412). Sections were washed three times with PBS and Fluoromount (Southern Biotech) was applied before cover slips were placed over section.

In vivo DRG calcium imaging

Adult mice expressing Pirt-Cre and lox-stop-lox GCaMP6s were anesthetized by i.p. injection of chloral hydrate (20 µl /gram of 25 mg/ml solution). The back was shaved and disinfected with alcohol before application of ophthalmic ointment (Lacrilube; Allergen Pharmaceuticals). A dorsal laminectomy was performed below the lumbar enlargement (L5) targeting S1. During the procedure, care was taken to keep dura intact. A 2 cm incision was made at the lumbar enlargement. 0.1 mL of 1% lidocaine was injected into paravertebral muscles before dissection to expose L3–L5 vertebrae. Using rongeurs, the surface aspect of the L4 DRG transverse process was removed and the underlying DRG exposed. Mice were laid abdomen-down on a custom-designed microscope stage and the spinal column was secured at two sites using clamps. Images were acquired using a laser-scanning confocal microscope (Leica LSI microscope) equipped with a 53 0.5 NA macro dry objective and fast EM-CCD camera. Live images were acquired at 8 to 10 frames in frame-scan mode per 7–8 s, at depths of 0 to 70 mm below the dura with the DRG in the focal plane. Images were taken 30 min

after peripheral stimulation of DRG via injection of vehicle or bilirubin by Hamilton syringe (5 μl) Throughout imaging, body temperature was maintained at 37°C ± 0.5°C with a heating pad and rectal temperature monitoring. Anesthesia was maintained with 2% isoflourane and pure oxygen delivered through nosecone.

Raw image stacks were collected, deconvoluted, and imported into ImageJ (NIH). Optical planes from sequential time points were re-aligned and motion-corrected using the stackreg rigid-body cross-correlation-based image alignment plugin in ImageJ. Calcium signaling amplitudes were expressed as F_t / F_0 as a function of time. F_0 was defined as the average pixel intensity during the first two to six frames of each imaging experiment. All neurons that displayed a > 0.25 F_0 change from baseline were selected for further analysis. In subsequent analysis, neurons that displayed a > 0.25 F_0 change during either the baseline or the saline imaging periods were excluded from analysis.

Mouse models of cholestasis and sample collection

1-naphthyl isothiocyanate (ANIT; Sigma) was solubilized in olive oil (Sigma). Animals were dosed with 25 mg/kg ANIT *per os* daily for five days. On day five, animals were acclimatized for itch behavior. On day six, animals were placed in test chambers and videotaped for one hour. The number of scratching bouts, defined as a continuous scratching movement with either hindpaw, was counted and binned in five minute intervals during the one hour period. After itch

behavior was assessed, animals were administered pentobarbital (50 mg/kg, *i.p.)*. Blood was collected by cardiac puncture and placed into heparinized tubes (BD Biosciences). After centrifugation, plasma was collected, aliquoted, and stored at -20°C until analysis. Bile acid levels were assessed by a fluorometric kit from Cell Biolabs. When applicable, mice were then proceeded for histology. For QWF antagonism of cholestatic itch, Day 5 ANIT-treated animals were dosed with either 1mg/kg QWF dissolved in PBS or PBS vehicle *i.v.* via tail vein injection approximately 10 minutes before behavioral assessment of spontaneous itch. The dose was chosen based on previous studies (Azimi et al., 2017) as well as published pK data indicating stability in plasma ($t_{1/2}$ = 70 min).

Skin bilirubin extraction

The skin of mice were exposed by applying a hair removal cream for 5 min, after which the skin was excised from the back and nape of mice and frozen at -80°C until processing. To extract skin bilirubin, skin was finely minced with a blade and then dounce homogenized at 4°C in 99% chloroform/1% glacial acetic acid (v/v). The organic layer was separated from any remaining tissue by centrifugation at 4°C at 16,000*g* for 10 min. The organic layer was subsequently washed in 1% glacial acetic acid, then 0.2 M $NaHCO_3$, and then H_2O. The organic layer was evaporated with a speedvac until the pellet was dry, after which the pellet was resolubilized in buffer (50 mM Tris,150 mM NaCl, 1% TritonX-100, 5% glycerol at pH 7.4). The final pellet was resuspended as thoroughly as possible,

but was unfortunately relatively insoluble. The calculated yield was 1.83 ± 0.2463 (SD) % and accordingly factored in to normalize skin bilirubin.

UnaG purification

UnaG was expressed in pMAL-6P2-6xHIS in BL21(DE3) cells. Starter cultures were grown to saturation overnight in Luria Broth (LB) at 37°C. Starter cultures were then diluted 10-fold in LB and grown to an OD_{600} of 0.3 at 37°C, after which cultures were moved to 18°C. At OD_{600} of 0.6, protein expression was induced by the addition of 400 µM isopropyl β-D-1-thiogalactopyranoside for 16 h at 18°C. Cells were harvested by centrifugation, resuspended in 15 ml of resuspension buffer (50 mM HEPES, 300 mM NaCl, 0.5 mM TCEP, 10% glycerol, 1 mM PMSF, 2.34 µM leupeptin, 1.45 µM pepstatin at pH 7.4) per liter of culture, and flash frozen in liquid nitrogen for storage at −80 °C.

For purification, pellets were thawed on ice and sonicated to lyse. Lysate was clarified by centrifugation at 26,000*g* at 4°C for 30 min and subsequently loaded onto an amylose column. Protein was eluted with 20 mM maltose in protease buffer (50 mM Tris, 150 mM NaCl, 0.5 mM TCEP, 10% glycerol, 0.01% TritonX-100 at pH 7.4), after which the MBP was were removed by the addition of Prescission Protease (GE Healthcare) for 16 h at 4°C. UnaG was further purified by a second nickel-affinity step to remove the cleaved tag and Prescission Protease. Protein was further purified on a gel-filtration column (S-200, GE Healthcare) in 50 mM HEPES, 300 mM NaCl, 0.5 mM TCEP, 10% glycerol at pH 7.4. The purity of peak fractions was assessed by SDS-PAGE. The purified

protein was concentrated using a 10-kDa MWCO filter (Amicon) and flash frozen in gel filtration buffer supplemented with 30% glycerol for storage at −80 °C.

Patient plasma and skin bilirubin quantification

To measure plasma bilirubin, patient plasma was diluted 1:20 in HBSS containing purified UnaG. To measure skin bilirubin, UnaG was added directly After a 10 min incubation at 25°C, bilirubin was quantified by interpolating from a standard curve. Samples with blood and hemolysis were excluded from analysis. Skin bilirubin was ormalized to the dry weight of the skin.

Plasma bilirubin depletion

Plasma bilirubin was depleted either by selective oxidation by $FeCl_3$ to biliverdin IXα/biliverdin XIIIα or by immunoprecipitation. $FeCl_3$ was prepared as solution of 20% $FeCl_3$ in 0.1N HCl/methanol. $FeCl_3$ was fluxed with plasma at a final concentration of 1.5% $FeCl_3$ at 37°C for 10 min. $FeCl_3$ is a mild oxidant but exhibits a redox potential that the oxidation of bilirubin to biliverdin (Dolphin, 1978). Bilirubin was also immunopreciptated by incubating plasma with 5 µg of either normal rabbit IgG or anti-bilirubin antibody (generated as previously described (Doré et al., 1999)) coupled to protein A/G beads for 1 h at 25°C. To quantify bilirubin depletion, bilirubin was extracted from samples with 100% methanol and subjected to HPLC and UV-visible spectroscopic analysis. Absorbance was adjusted to a baseline of 0 OD, and bilirubin was quantified by integrating the area under the chromatographic peak.

High pressure liquid chromatography (HPLC)

Plasma bilirubin was detected by HPLC using an analytical LC-18 column, 25 cm × 4.6 mm (Xterra, Waters Corporation). Bilirubin was eluted with gradients of mobile phases: 0.1 M ammonium acetate in 60% methanol/40% water (v/v) (pH 5.2) (Solvent A) and 100% methanol (Solvent B). Bilirubin was eluted as follows: 0 to 14 min: linear gradient from 100% A to 100% B; 14 to 19 min: linear gradient from 100% A to 100% B; 19-24 min: isocratic elution at 100% A. Bilirubin exhibited a retention time of approximately 14-15 min and was detected by measuring absorbance at 450 nm. The peak corresponding to plasma bilirubin was confirmed with the addition of 10 μM bilirubin to the sample as an internal standard.

Quantification and Statistical Analysis

Group data were expressed as mean ± SEM unless otherwise noted. Two-tailed unpaired Student's t-tests, Fisher's exact test, and Chi-squared tests were used to determine significance in statistical comparisons, and differences were considered significant at $P < 0.05$. Statistical power analysis was used to justify sample size, and variance was determined to be similar among all treatment groups as determined by F test. No samples or animals subjected to successful procedures and/or treatments were excluded from analysis. All behavior experiments were designed in a blocked manner with consideration for both genotype and treatment.

Measuring G-protein-coupled receptor signaling via radiolabeled GTP binding

Summary

G-protein-coupled receptors (GPCR) are a large family of transmembrane receptors that play critical roles in normal cellular physiology and constitute a major pharmacological target for multiple indications, including analgesia, blood pressure regulation, and the treatment of psychiatric disease. Upon ligand binding, GPCRs catalyze the activation of intracellular G-proteins by stimulating the incorporation of guanosine triphosphate (GTP). Activated G-proteins then stimulate signaling pathways that elicit cellular responses. GPCR signaling can be monitored by measuring the incorporation of a radiolabeled and non-hydrolyzable form of GTP, [^{35}S]guanosine-5'-O-(3-thio)triphosphate ([^{35}S]GTPγS), into G-proteins. Unlike other methods that assess more downstream signaling processes, [^{35}S]GTPγS binding measures a proximal event in GPCR signaling and, importantly, can distinguish agonists, antagonists, and inverse agonists. The present protocol outlines a sensitive and specific method for studying GPCR signaling using crude membrane preparations of an archetypal GPCR, the μ-opioid receptor (MOR1). Although alternative approaches to fractionate cells and tissues exist, many are cost-prohibitive, tedious, and/or require non-standard laboratory equipment. The present method provides a simple procedure that enriches functional crude membranes. After isolating MOR1, various

pharmacological properties of its agonist, [D-Ala, N-MePhe, Gly-ol]-enkephalin (DAMGO), and antagonist, naloxone, were determined.

Introduction

G-protein-coupled receptors (GPCRs) are a large family of cell-surface receptors responsible for a remarkable array of physiological processes, including analgesia, olfaction, and behavior(Kobilka, 2007). GPCRs act by sensing specific external signals and subsequently stimulating intracellular signaling. They therefore mark a key junction between the external and internal environments of a cell. Due to the critical role GPCRs play in biology, they have become major targets for both basic research and drug discovery(Neubig and Siderovski, 2002; Overington et al., 2006).

Unlike other receptor families that bind discrete ligands, GPCRs can bind very different types of molecules. While one GPCR may interact with peptides, another may sense photons, small molecules, or ions(Buck and Axel, 1991; Kobilka, 2007). While their ligands are diverse, GPCRs are unified in their overall architecture and function. Individual GPCRs are made up of seven α-helical transmembrane proteins with extracellular amino terminals and intracellular carboxyl terminals(Kobilka et al., 1987; Stenkamp et al., 2000). GPCRs are coupled to intracellular G-proteins—heterotrimeric protein complexes composed of α, β, and γ subunits—which mediate diverse signaling pathways(Neer, 1995). The G_α subunit is a guanine nucleotide-binding protein that is inactive when bound to guanosine diphosphate (GDP) and active when bound to guanosine triphosphate (GTP)(LONDOS et al., 1974; Ross and Gilman, 1977). When GPCRs bind their ligands, they undergo a conformational change that permits G_α to dissociate from $G_{\beta\gamma}$, thereby allowing G_α to exchange GDP for GTP(Neer, 1995).

The receptor itself is phosphorylated at its carboxyl terminal by various serine/threonine kinases(STADEL et al., 1983; WILDEN and KUHN, 1982) and internalized to attenuate receptor signaling(Lefkowitz, 2004; Leftowitz and Shenoy, 2005; Lohse et al., 1990). Meanwhile, the activated G_{α} monomer and $G_{\beta\gamma}$ dimer proceed to activate distinct signaling pathways(Neer, 1995). There are several isoforms of each G-protein subunit, and each isoform targets particular downstream pathways and secondary messenger systems. The major G_{α} isoforms include G_s, G_q, $G_{i/o}$, and $G_{12\text{-}13}$. Typically, individual GPCRs associate with a particular G_{α} isoform, thereby linking an external stimulus to a specific cellular response(Kobilka, 2007).

Characterizing a GPCR-ligand interaction is critical to understanding the biology of the receptor. As GDP/GTP exchange is one of the earliest events that follows ligand binding, monitoring GTP binding can measure GPCR activation or inhibition. Assaying more downstream events in GPCR signaling is often not as quantitative or stoichiometric, may not distinguish full agonists from partial ones, and can require expensive reagents. Moreover, increased GTP binding to G_{α} proteins is an almost-universal event following GPCR activation, meaning that measuring GTP binding is a broadly applicable assay for monitoring the activity of most GPCRs. Measuring GTP binding is a simple and rapid approach to monitor GPCR signaling in cells overexpressing the receptor of interest or in native tissue. The present protocol details a functional GTP-binding assay using an archetypal GPCR, the μ-opioid receptor (MOR1), to quantitatively determine the activity of an agonist and antagonist on GPCR signaling.

This protocol first outlines how to isolate crude membranes from cells overexpressing MOR1. Note that this protocol is not limited to overexpression systems and can be applied to many sources of membrane, including native tissue or preparations expressing multiple receptors and G proteins(Salah-Uddin et al., 2008). The protocol then details how to measure the binding of a radioactive GTP analog to these membranes in response to varying concentrations of [D-Ala, N-MePhe, Gly-ol]-enkephalin (DAMGO) or naloxone, a MOR1 agonist and antagonist, respectively. The GTP analog, [^{35}S]guanosine-5'-O-(3-thio) triphosphate ([^{35}S]GTPγS), is non-hydrolyzable. This property is critical because G_{α} subunits exhibit intrinsic GTPase activity(Neer, 1995) and would eliminate the labeled gamma phosphate on a hydrolyzable GTP radiochemical. Membranes are then trapped onto glass fiber filters and washed, after which the radiolabeled GTP is quantified by liquid scintillation counting. Multiple pharmacological parameters can be derived to characterize the receptor-ligand interaction, including the half-maximal response (EC_{50}) and Hill coefficient (n_H) for agonists and the half-maximal inhibitory concentration (IC_{50}) and equilibrium dissociation constant (K_b) for antagonists(Lazareno and Birdsall, 1993; MarÉchal, 2011; Yung-Chi and Prusoff, 1973).

Protocol

1. *Expression of recombinant HA-MOR1 in cultured cells*

Note: Follow all cell culture protocols in a sterile laminar flow hood.

1.1) Sterilize the cell culture laminar flow hood with 70% ethanol and maintain sterile technique throughout the cell culture.

1.2) Prepare human embryonic kidney cells 293 (HEK293) cell culture medium, complete Dulbecco's Modified Eagle Medium (DMEM): DMEM, pH 7.4, supplemented with 2 mM L-glutamine, 1% penicillin/streptomycin, and 10% fetal bovine serum.

1.3) Plate 2.5 x 10^6 HEK293 cells onto a 10-cm tissue culture plate in 10 mL of complete DMEM and incubate at 37 °C and 5% CO_2 until 70%-80% confluency is reached (overnight).

Note: To collect enough protein for a complete GTP-binding experiment, plate at least three 10-cm plates of cells.

1.4) Transfect the cells with HA-MOR1 using a transfection reagent of choice and by following the manufacturer's guidelines. Incubate for 36-48 h.

Note: Human MOR-1 cDNA (NCBI Reference Sequence: NM_000914.4) was a generous gift from Gavril Pasternak and was cloned into pCMV-HA.

2. *Cell fractionation and membrane collection*

2.1) Prepare the following lysis buffers:

2.1.1) Buffer 1: 10 mM 4-(2-hydroxyethyl)-1-piperazineethanesulfonic acid (HEPES), pH 7.4; 1 mM ethylene glycol-bis(β-aminoethyl ether)-N,N,N',N'-tetraacetic acid (EGTA); 10% sucrose; protease inhibitor cocktail; and 1 mM dithiothreitol (DTT). Add the DTT fresh on the day of membrane isolation.

2.1.2) Buffer 2: 10 mM HEPES, pH 7.4; 1 mM EGTA; 1 mM $MgCl_2$; and 1 mM DTT. Add the DTT fresh on the day of membrane isolation.

2.2) Remove the transfected cells from the incubator (step 1.4), aspirate the medium, and rinse the cells with 5 mL of ice-cold phosphate-buffered saline (PBS). Aspirate the PBS and excess liquid from the plate.

2.3) Add 600 µL of Buffer 1 to the cells. Using a cell scraper, dislodge the cells from the plate surface and pipette the cell suspension into a 1.6-mL microcentrifuge tube.

2.4) Immediately snap-freeze the microcentrifuge tube in liquid nitrogen. Once the samples are frozen, thaw the lysates on ice or place them at -80 °C for long-term storage.

2.5) Repeat steps 2.3 and 2.4 with all plates of cells.

2.6) Once the lysates have thawed, use a single-pulse micro-tube homogenizer to break open the cells. Pulse the homogenizer 3-5 times for 10 s, placing the tube back on ice for 30 s between pulses.

2.6.1) Collect 20 µL as whole cell fraction.

2.7) Centrifuge the remaining sample for 10 min at 1,000 x g and 4°C. Collect the supernatant and place in a new 1.6-mL microcentrifuge tube on ice.

2.8) Resuspend the pellet in 100 µL of Buffer 1 and re-homogenize with a pestle. Pulse the homogenizer 3-5 times for 5 s, placing the tube back on ice for 30 s between pulses.

2.8.1) Centrifuge the sample a second time for 10 min at 1,000 x g and 4 °C. Combine the supernatant with the supernatant from step 2.7.

Note: The remaining pellet contains nuclear and membrane proteins.

2.9) Centrifuge the combined supernatants for 20 min at 11,000 x g and 4 °C. Separate the supernatant (the cytosolic fraction) into a new 1.6-mL microcentrifuge tube.

2.10) Resuspend the pellet in 200 µL of Buffer 2. Homogenize the pellet by triturating it 3-5 times. Centrifuge the sample for 20 min at 21,100 x g and 4 °C. Aspirate the supernatant. Resuspend the pellet containing the crude membrane fraction in 50 µL of Buffer 2.

2.11) Immediately proceed to the GTPγS binding experiments (section 3) or snap-freeze in liquid nitrogen and store at -80 °C.

3. *[^{35}S]GTPγS binding*

Note: Use standard radiochemical safety protocol when handling [^{35}S]GTPγS and when conducing [^{35}S]GTPγS binding experiments. Wear protective gloves and a lab coat at all times. Check the packaging material for leaks or cracks. Dispose of waste and excess reagents according to institutional protocols.

3.1) Prepare incomplete binding buffer (IBB) by mixing 50 mM HEPES, pH 7.4; 5 mM MgCl2; 100 mM NaCl; and 1 mM ethylenediaminetetraacetic acid (EDTA) in distilled water.

3.2) Dilute stock [^{35}S]GTPγS to 50 nM in 10 mM Tris-HCl, pH 7.6, and 10 mM DTT. Make 500-µL aliquots and store them at -80 °C. Use only a freshly thawed aliquot immediately before initiating the experiment. Thaw the aliquots on ice.

3.3) Prepare non-radiolabeled GTPγS by dissolving 1 mg of GTPγS powder in 177.62 µL of pure water for a stock concentration of 10 mM. Make 10-µL aliquots and store them at -20 °C.

3.4) Prepare complete binding buffer (CBB) by supplementing IBB to include a final concentration of 1 mM DTT, 0.1% (wt/vol) bovine serum albumin (BSA), 10 µM GDP, and 0.1 nM [^{35}S]GTPγS.

Note: The CBB now contains radiolabeled GTP. Take appropriate safety precautions while working with radioactive solutions.

3.5) Thaw the membrane fraction from step 2.11 on ice.

3.6) Quantify the protein concentration of the membrane fraction via a Bradford protein assay using a spectrophotometer at 595 nm.

3.6.1) Prepare a dilution series of BSA protein standards with Buffer 2, at final concentrations of 0, 250, 500, 750, 1,500, 2,500, and 5,000 µg/mL.

3.6.2) Add 2 µL of each standard or membrane to 1 mL of Bradford reagent in a cuvette. Mix thoroughly by vortexing.

3.6.3) Adjust the spectrophotometer to a wavelength of 595 nm and blank using the cuvette with 0 µg/mL protein.

3.6.4) Wait 5 min and read each of the standards and each of the samples at a 595-nm wavelength.

3.6.5) Plot the absorbance of the standards versus the concentration. Using the Beer-Lambert Law (A = εcl, where ε = extinction coefficient,

l = length of cuvette, and c = concentration), calculate the concentration of the membrane samples.

3.7) Dilute the membrane fractions to a concentration of 100 μg protein/mL in IBB.

Note: One 10-cm dish of HEK293 cells typically yields between 1 and 3 mg protein/mL.

3.8) Prepare the following experimental conditions in individual 1.6-mL microcentrifuge tubes: a ligand dilution series, a basal activity condition to measure basal GTP binding, and a non-specific binding condition to measure non-specific GTP binding.

3.8.1) For the ligand dilution series, prepare a dilution series of the ligand of interest in a final volume of 100 μL of CBB. Prepare the ligand series at 2x the desired final concentrations. Space the ligand concentrations to adequately cover a range of responses.

3.8.1.1) To assay the effect of DAMGO on GTP binding via MOR1, prepare DAMGO dilutions of 2 mM, 200 μM, 20 μM, 2 μM, 200 nM, 20 nM, 2 nM, 200 pM, 20 pM, and 2 pM in CBB (final volume: 100 μL).

Note: For example, if the ligand of interest has an expected EC_{50} value of 10 μM, prepare ligand dilutions of 200 nM, 2 μM, 20 μM, 200 μM, and 2 mM. These five conditions cover a wide range of concentrations and are 2x the concentration desired for the assay.

3.8.2) For basal binding, prepare a tube with 100 μL of CBB only.

3.8.3) For non-specific binding, prepare a tube with 99 µL of CBB supplemented with 1 µL of 2 mM non-radiolabeled GTPγS.

3.9) Add 100 µL of the diluted membrane solution (step 3.7) to each experimental condition.

3.10) Incubate the membranes with the various experimental conditions in 1.6-mL microcentrifuge tubes for 30 min at 25 °C in a thermomixer or on an orbital shaker.

4. *Membrane filtration*

4.1) Prepare wash buffer by combining 50 mM Tris-HCl, pH 7.4; 5 mM $MgCl_2$; and 50 mM NaCl in distilled water.

4.2) Presoak the glass fiber filters in water for 10 min.

Note: Filters have a pore size of 1 µm, a diameter of 2.1 cm, and a thickness of 675 µm.

4.3) Remove the samples from the thermomixer or orbital shaker (step 3.10). Briefly pulse-spin the samples for 5 s to collect each sample at the bottom of the tube.

4.4) Remove the lid of the vacuum filtration apparatus. Lay the presoaked filters onto the vacuum ports of the apparatus. Re-secure the apparatus lid to form a vacuum seal. Turn on the vacuum.

4.5) Pipette 195 µL of each 200-µL experimental condition onto filters to minimize error from adsorption to the walls of the tube and/or from pipetting.

4.6) Wash the filters three times with 1 mL of ice-cold wash buffer.

5. *Liquid scintillation counting*

5.1) Place 5-mL scintillation counting vials in a counting rack. Add 5 mL of scintillation fluid to each vial.

5.2) Turn off the vacuum (step 4.4). Remove the lid of the vacuum filtration apparatus. Using tweezers, pick up the filters from the vacuum ports of the filtration apparatus and drop each filter into an individual 5-mL scintillation vial.

5.3) Prepare one vial with 195 µL of CBB to determine the maximal signal.

5.4) Cap each vial securely. Incubate the vials on an orbital shaker at 25 °C for 10 min.

5.5) Turn on the scintillation counter. Program the scintillation counter to measure ^{35}S isotope emission for 5 min per sample using the standard associated scintillation program.

5.6) Press “Start” to take a count.

5.7) When the counting is done, dispose the counted vials as hazardous waste.

6. *Data analysis*

6.1) Enter the data into statistics and analysis software.

6.1.1) Subtract the non-specific binding from each of the other measurements to determine the specific binding.

Note: The degree of non-specific binding is determined by the sample incubated with non-radiolabeled GTPγS (step 3.8.3).

6.1.2) Open the statistics and analysis software and select an XY dataset entry.

6.1.3) Enter the specific binding data from the [^{35}S]GTPγS-binding experiments into a data table in the statistics and analysis software. Enter the agonist concentrations, as molar concentrations, in the "X" column. Enter the associated ^{35}S counts as "Y" values.

6.2) Transform the data.

6.2.1) Convert the X values to their respective logarithm by clicking "Analyze." Select "Transform" from the built-in analyses.

6.2.2) Within the "Transform" dialog box, select "Transform X values using" and select the function "X=log(X)." Choose to create a new graph of the results.

6.2.3) Click "OK."

6.3) Normalize the Y-values.

6.3.1) With the transformed results displayed, click "Analyze." Select "Normalize" from the built-in analyses.

6.3.2) Within the "Normalize" dialog box, select the radio button to define 0% as the "smallest value in each data set" and 100% as the "largest value in each data set." Select the box to present the results as percentages. Select the box to create a new graph of the results.

6.3.3) Click "OK."

6.4) Fit a nonlinear regression curves to the plotted data. Perform a nonlinear regression analysis.

6.4.1) With the normalized results displayed, click "Analyze." From the built-in analyses, select "Nonlinear regression (curve fit)."

6.4.2) If investigating an agonist, select “log(agonist) vs. normalized response - variable slope” from the dialog box.

6.4.3) If investigating an antagonist, “select log(antagonist) vs. normalized response - variable slope” from the dialog box.

6.4.4) Click “OK.”

6.5) Review the graph and results to ensure that the fit and data are in reasonable agreement. Ensure that the regression matches the general pattern of the plotted data and that the residuals are not so large that they render the dose-response curve flat.

Note: The software will summarize the results of the nonlinear regression and detail the half-maximal response (EC_{50}), Hill coefficient (n_H), and half-maximal inhibitory concentration (IC_{50}).

6.6) Derive agonist/antagonist parameter potency.

6.6.1) Derive the agonist equilibrium dissociation constants (K_b) from either of the following experiments(Lazareno and Birdsall, 1993; MarÉchal, 2011; Yung-Chi and Prusoff, 1973):

6.6.1.1) Assess the shift in the dose-response of an agonist in competition with a fixed concentration of antagonist. Here, $EC_{50}' = EC_{50}$ (1 + [antagonist]/$antagonist_{Kb}$), where EC_{50}' is the right-shifted EC_{50}.

6.6.1.2) Assess [^{35}S]GTPγS binding with varying concentrations of antagonist in competition with a fixed concentration of agonist. Here, $K_b = IC_{50}/ (2 +([agonist]/agonist\ EC_{50})^n)^{1/n} - 1$, where n is the Hill coefficient of the agonist.

Depending upon the variability of the data, repeat the experiment (steps 3.8-5.6) for each ligand approximately 3-5 times and average the results using a statistics and analysis software.

Representative Results

Cell fractionation can be used to isolate and enrich membrane-associated proteins from cytosolic and nuclear proteins. **Fig. 40** is a Western blot demonstrating the contents of the three primary fractions that can be collected during the subcellular fractionation process. Specifically, **Fig. 40** shows that fractionation cleanly separates membrane proteins (*i.e.,* Na+/K+ ATPase, protein disulfide isomerase (PDI), and HA-MOR1) from histone H2A and glyceraldehyde 3-phosphate dehydrogenase (GAPDH), nuclear proteins, and cytosolic proteins, respectively. Additionally, **Fig. 40** demonstrates the enrichment of proteins (lane 1 compared to lane 4) in their respective subcellular fractions as a result of fractionation. A representative Ponceau stain demonstrates equal protein loading in each fraction. It is important to note that this fractionation protocol does not distinguish between different cellular membranes. PDI is generally localized to the endoplasmic reticulum (ER), whereas Na+/K+ATPase is predominantly at the plasma membrane. However, both proteins are present in the final crude membrane fraction (**Fig. 40, lane 4**). Additionally, while this protocol robustly separates nuclear proteins from the cytosolic and final membrane fraction (**Fig. 40, lanes 2-4**), the fraction enriched for nuclear proteins contains some membrane proteins (**Fig. 40, lane 2**), possibly from the ER.

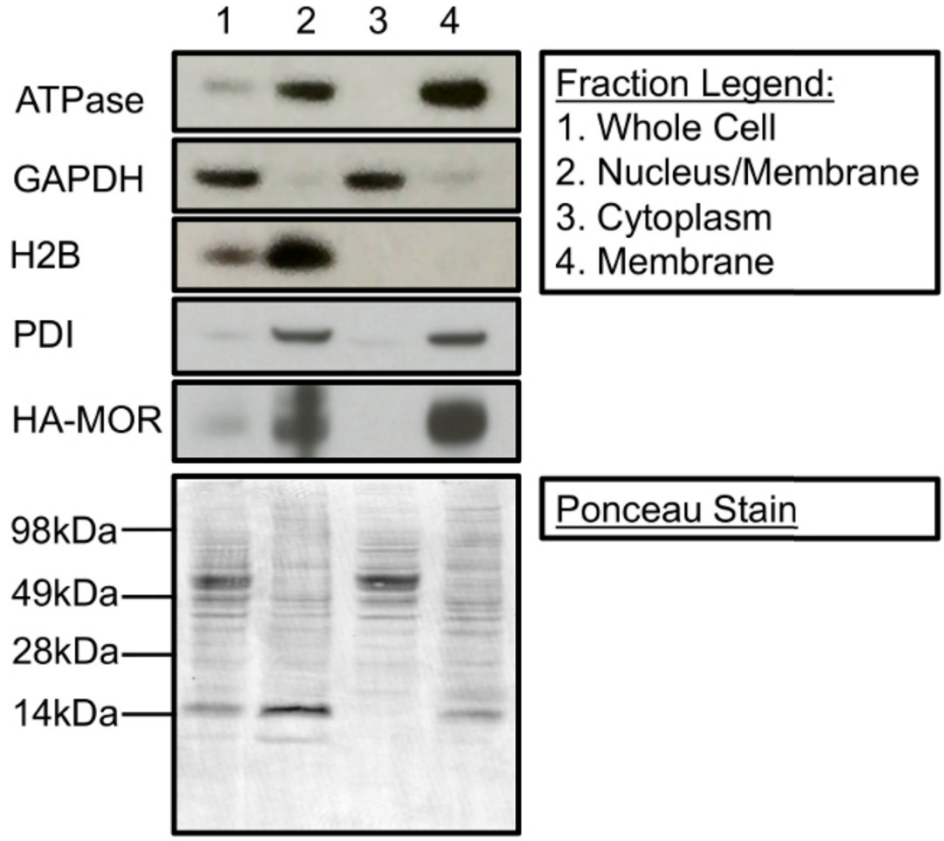

Figure 40. Cellular Fractionation Separates Membrane-associated, Nuclear, and Cytosolic proteins.

(**Top**) Lane 1 represents the protein present in the whole cell. Lane 2 contains nuclear and membrane-associated proteins separated during the first centrifugation steps. Lane 3 is the cytosolic fraction separated following 20 min of centrifugation at 11,000 x g. Lane 4 contains a crude membrane fraction suitable for [^{35}S]GTPγS-binding experiments. (**Bottom**) Ponceau stain of a Western membrane demonstrates protein loading for each cellular fraction.

Multiple pharmacological parameters can be derived to characterize a GPCR-ligand interaction via GTP-binding experiments (**Table 2**). For example, the half-maximal response (EC_{50}) and Hill coefficient (n_H) of an agonist can be derived by monitoring GTP binding in response to varying doses of the agonist. **Fig. 41a** demonstrates dose-responsive GTP binding to MOR1 after DAMGO treatment. When the data is fit to a four-parameter nonlinear regression, the fit describes a receptor-ligand interaction with an EC_{50} of 185 ± 23 nM and a Hill

coefficient of 0.46 ± 0.06. The shallow GTP-binding curve observed after DAMGO treatment suggests negative cooperativity between DAMGO and MOR1. This method can also identify and describe the pharmacology of an antagonist. As **Fig. 41a-b** illustrates, naloxone is an MOR1 antagonist. The agonist potency (K_b) of naloxone, 97 ± 20 nM, was determined by varying the concentration of naloxone in competition with a fixed concentration of DAMGO (**Fig. 41a**). Naloxone exhibited a Hill coefficient of 0.88 ± 0.06, suggesting independent binding between naloxone and MOR1. If the action of a ligand is unknown, this assay can discriminate between an agonist, antagonist, and inverse agonist. If the ligand is an agonist, there would be an increase in GTP binding, as in **Fig. 41a**, following DAMGO application. If the ligand is an inverse agonist, there would be diminished binding of GTP relative to basal binding. If the ligand is an antagonist, there would be no effect upon treatment with ligand alone. If applied concomitantly with an agonist, an antagonist would inhibit the ability of the agonist to stimulate GTP binding. **Fig. 41a** illustrates the antagonist activity of naloxone against the agonist DAMGO.

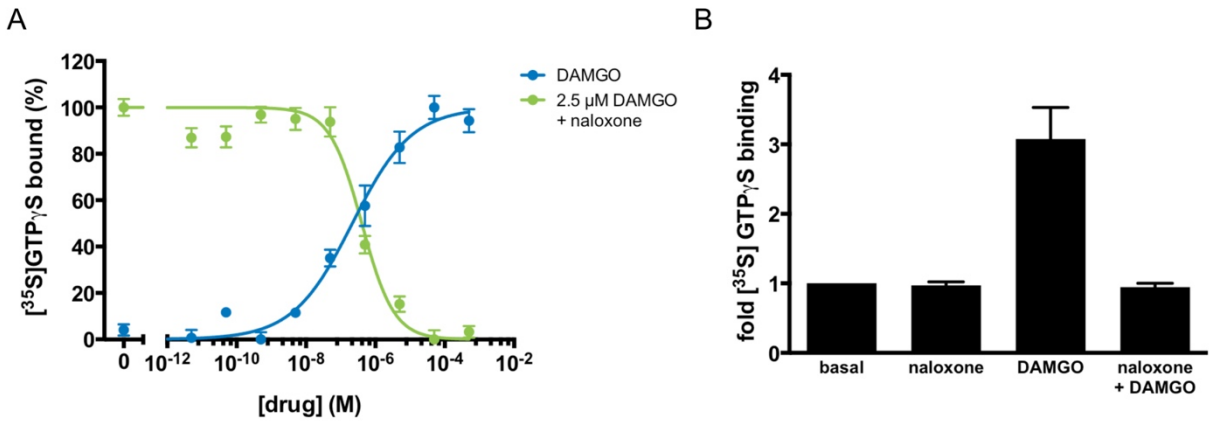

Figure 41. Agonism and Antagonism at μ-opioid Receptors Defined by [^{35}S]GTPγS binding.

a, [^{35}S]GTPγS dose-response curve to DAMGO alone (blue) or naloxone in competition with 2.5 μM DAMGO (green). [^{35}S]GTPγS binding was normalized to the maximal stimulation in each experiment and was expressed as a percentage. The points shown are the mean of triplicate determinations and are expressed as the mean ±S.E.M. **b**, Antagonism of DAMGO-stimulated [^{35}S]GTPγS binding by naloxone. [^{35}S]GTPγS binding was quantified after the addition of naloxone alone (100 μM), DAMGO alone (10 μM), or DAMGO (10 μM) in competition with naloxone (100 μM). The results are expressed as the mean ±S.E.M. of three independent experiments.

Discussion

The present protocol describes two separate but complementary methods: a simple approach to fractionate cells and tissues into broad but distinct compartments and a means to investigate GPCR signaling by measuring [^{35}S]GTPγS binding.

Ligand	EC_{50} or IC_{50}	n_H	K_b
	nM		*nM*
DAMGO	185 ± 23	0.46 ± 0.06	
naloxone	420 ± 87	0.88 ± 0.06	97 ± 20

Table 2. Pharmacological parameters of DAMGO and naloxone activity at μ-opioid receptors.

The half-maximal response (EC_{50}) and Hill coefficient (n_H) for DAMGO were derived from [^{35}S]GTPγS binding in response to varying doses of DAMGO. The half-maximal inhibitory concentration (IC_{50}) and equilibrium dissociation constant (K_b) for naloxone were determined from the effect of competition between naloxone and 2.5 μM DAMGO on [^{35}S]GTPγS binding. The results are expressed as the mean ±S.E.M. of three independent experiments.

Efficient cellular fractionation has a wide range of applications, ranging from the extraction and enrichment of proteins, to the assessment of the subcellular localization of proteins, to the study of receptor pharmacology. Although alternative approaches to fractionate cells and tissues exist, the protocol presented here is comparatively cheaper, faster, and simpler. Unlike more established methods, however, this method is unable to cleanly separate plasma membrane-associated proteins from other membranous compartments, such as endosomes or the ER. It must also be noted that while the above protocol uses a transient overexpression system to generate cell membranes containing the GPCR of interest, this protocol is compatible with stable overexpression systems, as well as with animal or human tissue(Salah-Uddin et al., 2008).

Sample preparation is critical to maximize fraction yield and purity. It is particularly important to ensure complete homogenization and to minimize the transition times between centrifugation steps. Using a pellet homogenizer/pestle to completely disrupt the cell membrane significantly increases the crude membrane yield in the final cell fraction. If the membrane yield is too low, the two simplest solutions would be to scale up the initial cell culture and/or to homogenize the cell pellet a few more times. If individual fractions show a high degree of impurity, reduce the transition times between centrifugation and separation. Do not allow the samples to sit following centrifugation, as proteins may diffuse into the sample and reduce fraction purity.

Filtration-based [^{35}S]GTPγS binding is a rapid and quantitative method to measure the activation of G-proteins using the associated receptor. Measuring

GTP binding allows for a more quantitative measurement of GPCR activity than is generally possible when monitoring downstream processes. However, there are two critical limitations to the method outlined here. Most importantly, filtration-based [^{35}S]GTPγS quantitation is not equally feasible with all G_α isoforms(Harrison and Traynor, 2003; Milligan, 2003). In general, this method is restricted to $G_{i/o}$-coupled GPCRs like MOR1(Traynor and Nahorski, 1995). G_s- and G_q-coupled receptors tend to be less sensitive. This is likely due to the combination of the lower abundance of G_s/G_q and their relatively slower nucleotide exchange rate, making it difficult to distinguish real [^{35}S]GTPγS binding above background. This limitation has been addressed elsewhere using G-protein antibody capture techniques(Milligan, 2003). Some groups have found that eliminating GDP from the reaction improves the signal-to-noise ratio for G_s- or G_q-coupled receptors(Sittampalam et al., 2004). The second limitation is the membrane sensitivity to lipophilic agonists or surfactants. [^{35}S]GTPγS assays require functional receptor-G-protein complexes, and the addition of lipophilic molecules to the reaction system may disrupt the structure of the membranes or these complexes. If this is a potential concern, it may be advantageous to test whether the reagent of interest disrupts [^{35}S]GTPγS binding in an already well-characterized system, such as in DAMGO-mediated MOR1 stimulation. Other conditions to consider optimizing include the binding buffer pH, the concentrations of Mg^{2+} and NaCl, the protein concentration, and the incubation time(Sittampalam et al., 2004; Strange, 2010).

This protocol focused on a well-characterized GPCR, the MOR1, and well-characterized drugs, DAMGO (agonist) and naloxone (antagonist), that act on MOR1. However, one of the advantages of this technique is that it can be used to characterize unknown ligands as agonists, antagonists, or inverse agonists, depending upon how the ligand modulates GTP binding. When designing experiments, it is critical to use a range of concentrations of the ligand of interest and to be mindful of the range of outcomes: agonists will cause an increase in GTP binding over baseline, inverse agonists will cause a decrease in GTP binding compared to baseline, and antagonists will have little to no effect when added in isolation on baseline GTP binding.

In summary, this protocol describes a technique for performing subcellular fractionation, collecting crude membrane preparations, and investigating GPCR activation by measuring [^{35}S]GTPγS binding. These techniques can be readily adapted to a variety of cell culture and tissue models to study the pharmacology of one of the most important families of receptors.

References

1. Alemi, F., Kwon, E., Poole, D.P., Lieu, T., Lyo, V., Cattaruzza, F., Cevikbas, F., Steinhoff, M., Nassini, R., Materazzi, S., et al. (2013). The TGR5 receptor mediates bile acid-induced itch and analgesia. J. Clin. Invest. *123*, 1513–1530.

2. Applegate, L.A., Luscher, P., and TYRRELL, R.M. (1991). Induction of Heme Oxygenase - a General Response to Oxidant Stress in Cultured-Mammalian-Cells. Cancer Res *51*, 974–978.

3. Arnold, W.P., Mittal, C.K., Katsuki, S., and Murad, F. (1977). Nitric oxide activates guanylate cyclase and increases guanosine 3′: 5′-cyclic monophosphate levels in various tissue preparations. Proc. Natl. Acad. Sci. U.S.a. *74*, 3203–3207.

4. Azimi, E., Reddy, V.B., Pereira, P.J.S., Talbot, S., Woolf, C.J., and Lerner, E.A. (2017). Substance P activates Mas-related G protein-coupled receptors to induce itch. J. Allergy Clin. Immunol. *140*, 447–453.e3.

5. Azimi, E., Reddy, V.B., Shade, K.-T.C., Anthony, R.M., Talbot, S., Pereira, P.J.S., and Lerner, E.A. (2016). Dual action of neurokinin-1 antagonists on Mas-related GPCRs. JCI Insight *1*, e89362.

6. Babbedge, R.C., Bland-Ward, P.A., Hart, S.L., and Moore, P.K. (1993). Inhibition of rat cerebellar nitric oxide synthase by 7-nitro indazole and related substituted indazoles. Br J Pharmacol *110*, 225–228.

7. Bagchi, R.N., Bond, A.M., Scholz, F., and Stösser, R. (1989). Characterization of the ESR Spectrum of the Superoxide Anion in the Liquid Phase. J. Am. Chem. Soc. *111*, 8270–8271.

8. Baranano, D.E., Rao, M., Ferris, C.D., and Snyder, S.H. (2002). Biliverdin reductase: A major physiologic cytoprotectant. Proc. Natl. Acad. Sci. U.S.a. *99*, 16093–16098.

9. Bassari, R. (2015). Jaundice associated pruritis: A review of pathophysiology and treatment. World J. Gastroenterol. *21*, 1404–1411.

10. Bautista, D.M., Wilson, S.R., and Hoon, M.A. (2014). Why we scratch an itch: the molecules, cells and circuits of itch. Nat. Neurosci. *17*, 175–182.

11. Becke, A.D. (1993). Density-Functional Thermochemistry .3. the Role of Exact Exchange. Journal of Chemical Physics *98*, 5648–5652.

12. BERENDSOHN, S., LOWMAN, J., SUNDBERG, D., and WATSON, C.J. (1964). Idiopathic Dyserythropoietic Jaundice. Blood *24*, 1–&.

13. Bergasa, N.V., Schmitt, J.M., Talbot, T.L., Alling, D.W., Swain, M.G., Turner, M.L., Jenkins, J.B., and Jones, E.A. (1998). Open-label trial of oral nalmefene therapy for the pruritus of cholestasis. Hepatology *27*, 679–684.

14. Bergasa, N.V., Talbot, T.L., Alling, D.W., Schmitt, J.M., Walker, E.C., Baker, B.L., Korenman, J.C., Park, Y., Hoofnagle, J.H., and Jones, E.A. (1992). A controlled trial of naloxone infusions for the pruritus of chronic cholestasis. Ygast *102*, 544–549.

15. Bielski, B.H.J., and Richter, H.W. (1977). A study of the superoxide radical chemistry by stopped-flow radiolysis and radiation induced oxygen consumption. J. Am. Chem. Soc. *99*, 3019–3023.

16. Bielski, B.H.J., Cabelli, D.E., Arudi, R.L., and Ross, A.B. (1985). Reactivity of HO 2/O −2Radicals in Aqueous Solution. Journal of Physical and Chemical Reference Data *14*, 1041–1100.

17. Bindokas, V.P., Jordán, J., Lee, C.C., and Miller, R.J. (1996). Superoxide production in rat hippocampal neurons: selective imaging with hydroethidine. J. Neurosci. *16*, 1324–1336.

18. Bisht, K., Canesin, G., Cheytan, T., Li, M., Nemeth, Z., Csizmadia, E., Woodruff, T.M., Stec, D.E., Bulmer, A.C., Otterbein, L.E., et al. (2019). Deletion of Biliverdin Reductase A in Myeloid Cells Promotes Chemokine Expression and Chemotaxis in Part via a Complement C5a--C5aR1 Pathway. J. Immunol. *202*, 2982–2990.

19. Breaven, G.H., D'Albis, A., and Gratzer, W.B. (1973). The interaction of bilirubin with human serum albumin. Eur. J. Biochem. *33*, 500–509.

20. BREIMER, L.H., WANNAMETHEE, G., EBRAHIM, S., and SHAPER, A.G. (1995). Serum Bilirubin and Risk of Ischemic-Heart-Disease in Middle-Aged British Men. Clin. Chem. *41*, 1504–1508.

21. Brennan, A.M., Suh, S.W., Won, S.J., Narasimhan, P., Kauppinen, T.M., Lee, H., Edling, Y., Chan, P.H., and Swanson, R.A. (2009). NADPH oxidase is the primary source of superoxide induced by NMDA receptor activation. Nat. Neurosci. *12*, 857–U857.

22. Browning, J.D., and Horton, J.D. (2004). Molecular mediators of hepatic steatosis and liver injury. J. Clin. Invest. *114*, 147–152.

23. Buck, L., and Axel, R. (1991). A novel multigene family may encode odorant receptors: a molecular basis for odor recognition. Cell *65*, 175–187.

24. Carstens, E., Akiyama, T., and Bergasa, N.V. (2014). Pruritus of Cholestasis.

25. Chen, W., Maghzal, G.J., Ayer, A., Suarna, C., Dunn, L.L., and Stocker, R. (2018). Absence of the biliverdin reductase-a gene is associated with increased endogenous oxidative stress. Free Radic. Biol. Med. *115*, 156–165.

26. Chouchani, E.T., Pell, V.R., Gaude, E., Aksentijević, D., Sundier, S.Y., Robb, E.L., Logan, A., Nadtochiy, S.M., Ord, E.N.J., Smith, A.C., et al. (2014). Ischaemic accumulation of succinate controls reperfusion injury through mitochondrial ROS. Nature *515*, 431–435.

27. CLAIREAUX, A.E., COLE, P.G., and LATHE, G.H. (1953). Icterus of the Brain in the Newborn. Lancet *265*, 1226–1230.

28. Cyr, M., Caron, M.G., Johnson, G.A., and Laakso, A. (2005). Magnetic resonance imaging at microscopic resolution reveals subtle morphological changes in a mouse model of dopaminergic hyperfunction. Neuroimage *26*, 83–90.

29. Dempsey, J.A., and Forster, H.V. (1982). Mediation of Ventilatory Adaptations. Physiol. Rev. *62*, 262–346.

30. Dennery, P.A., McDonagh, A.F., Spitz, D.R., RODGERS, P.A., and Stevenson, D.K. (1995). Hyperbilirubinemia Results in Reduced Oxidative Injury in Neonatal Gunn-Rats Exposed to Hyperoxia. Free Radic. Biol. Med. *19*, 395–404.

31. Dennery, P.A., Spitz, D.R., Yang, G., Tatarov, A., Lee, C.S., Shegog, M.L., and Poss, K.D. (1998). Oxygen toxicity and iron accumulation in the lungs of mice lacking heme oxygenase-2. J. Clin. Invest. *101*, 1001–1011.

32. DEXTER, D.T., HOLLEY, A.E., FLITTER, W.D., SLATER, T.F., WELLS, F.R., DANIEL, S.E., LEES, A.J., JENNER, P., and MARSDEN, C.D. (1994). Increased Levels of Lipid Hydroperoxides in the Parkinsonian Substantia-Nigra - an Hplc and Esr Study. Mov. Disord. *9*, 92–97.

33. Djousse, L., Levy, D., Cupples, L.A., Evans, J.C., D'Agostino, R.B., and Ellison, R.C. (2001). Total serum bilirubin and risk of cardiovascular disease in the Framingham Offspring Study. Am. J. Cardiol. *87*, 1196–.

34. Dolphin, D. (1978). The Porphyrins: Biochemistry, part A-B (Academic Pr).

35. Dong, X., Han, S.-K., Zylka, M.J., Simon, M.I., and Anderson, D.J. (2001). A Diverse Family of GPCRs Expressed in Specific Subsets of Nociceptive Sensory Neurons. Cell *106*, 619–632.

36. Doré, S., Goto, S., Sampei, K., Blackshaw, S., Hester, L.D., Ingi, T., Sawa, A., Traystman, R.J., Koehler, R.C., and Snyder, S.H. (2000). Heme oxygenase-2 acts to prevent neuronal death in brain cultures and following transient cerebral ischemia. Neuroscience *99*, 587–592.

37. Doré, S., Takahashi, M., Ferris, C.D., Hester, L.D., Guastella, D., and Snyder, S.H. (1999). Bilirubin, formed by activation of heme oxygenase-2, protects neurons against oxidative stress injury. Proc. Natl. Acad. Sci. U.S.a. *96*, 2445–2450.

38. Doré, S., and Snyder, S.H. (1999). Neuroprotective Action of Bilirubin against Oxidative Stress in Primary Hippocampal Cultures. Annals NY Acad Sci *890*, 167–172.

39. Duhr, S., and Braun, D. (2006). Why molecules move along a temperature gradient. Proc. Natl. Acad. Sci. U.S.a. *103*, 19678–19682.

40. d'Alessandro, N., Bianchi, G., Fang, X., Jin, F., Schuchmann, H.-P., and Sonntag, von, C. (2000). Reaction of superoxide with phenoxyl-type radicals. J. Chem. Soc., Perkin Trans. 2 1862–1867.

41. Eliakim, M., Eisner, M., and Ungar, H. (1959). Experimental intrahepatic obstructive jaundice following ingestion of alphanaphthyl-iso-thiocyanate. Bull Res Counc Isr Sect E Exp Med *8E*, 7–17.

42. Falchuk, K.H., Contin, J.M., Dziedzic, T.S., Feng, Z., French, T.C., Heffron, G.J., and Montorzi, M. (2002). A role for biliverdin IXalpha in dorsal axis development of Xenopus laevis embryos. Proc. Natl. Acad. Sci. U.S.a. *99*, 251–256.

43. FEE, J.A. (1982). Is Superoxide Important in Oxygen Poisoning. Trends Biochem Sci *7*, 84–86.

44. Ferrante, R.J., Browne, S.E., Shinobu, L.A., Bowling, A.C., Baik, M.J., MacGarvey, U., Kowall, N.W., Brown, R.H., and Beal, M.F. (1997). Evidence of increased oxidative damage in both sporadic and familial amyotrophic lateral sclerosis. J Neurochem *69*, 2064–2074.

45. Filonov, G.S., Piatkevich, K.D., Ting, L.-M., Zhang, J., Kim, K., and Verkhusha, V.V. (2011). Bright and stable near-infrared fluorescent protein for in vivo imaging. Nat. Biotechnol. *29*, 757–761.

46. Flegel, C., Schöbel, N., Altmüller, J., Becker, C., Tannapfel, A., Hatt, H., and Gisselmann, G. (2015). RNA-Seq Analysis of Human Trigeminal and Dorsal Root Ganglia with a Focus on Chemoreceptors. PLoS ONE *10*, e0128951.

47. Friebe, A., Schultz, G., and Koesling, D. (1996). Sensitizing soluble guanylyl cyclase to become a highly CO-sensitive enzyme. The EMBO Journal *15*, 6863.

48. Gao, X., Kim, H.K., Chung, J.M., and Chung, K. (2007). Reactive oxygen species (ROS) are involved in enhancement of NMDA-receptor phosphorylation in animal models of pain. Pain *131*, 262–271.

49. Gåfvels, M., Holmström, P., Somell, A., Sjövall, F., Svensson, J.-O., Ståhle, L., Broomé, U., and Stål, P. (2009). A novel mutation in the biliverdin reductase-A gene combined with liver cirrhosis results in hyperbiliverdinaemia (green jaundice). Liver Int. *29*, 1116–1124.

50. GIBLETT, E.R., COLEMAN, D.H., PIRZIOBIROLI, G., DONOHUE, D.M., MOTULSKY, A.G., and FINCH, C.A. (1956). Erythrokinetics - Quantitative Measurements of Red Cell Production and Destruction in Normal Subjects and Patients with Anemia. Blood *11*, 291–309.

51. Griffiths, W.C., Diamond, I., and Dextraze, P. (1975). The albumin binding of unconjugated bilirubin in serum. Clin. Biochem. *8*, 254–260.

52. Guo, J., and Lemire, B.D. (2003). The ubiquinone-binding site of the Saccharomyces cerevisiae succinate-ubiquinone oxidoreductase is a source of superoxide. J Biol Chem *278*, 47629–47635.

53. Hackett, P.H., Roach, R.C., Schoene, R.B., Harrison, G.L., and Mills, W.J. (1988). Abnormal control of ventilation in high-altitude pulmonary edema. J. Appl. Physiol. *64*, 1268–1272.

54. Han, L., Ma, C., Liu, Q., Weng, H.-J., Cui, Y., Tang, Z., Kim, Y., Nie, H., Qu, L., Patel, K.N., et al. (2012). A subpopulation of nociceptors specifically linked to itch. Nat. Neurosci. *16*, 174–182.

55. Harrison, C., and Traynor, J.R. (2003). The [35S]GTPγS binding assay: approaches and applications in pharmacology. Life Sciences *74*, 489–508.

56. Hatano, T., Saiki, S., Okuzumi, A., Mohney, R.P., and Hattori, N. (2016). Identification of novel biomarkers for Parkinson's disease by metabolomic technologies. J. Neurol. Neurosurg. Psychiatry *87*, 295–301.

57. Hegade, V.S., Krawczyk, M., Kremer, A.E., Kuczka, J., Gaouar, F., Kuiper, E.M.M., van Buuren, H.R., Lammert, F., Corpechot, C., and Jones, D.E.J. (2016). The safety and efficacy of nasobiliary drainage in the treatment of refractory cholestatic pruritus: a multicentre European study. Aliment. Pharmacol. Ther. *43*, 294–302.

58. Heusler, P., and Boehmer, G. (2004). The superoxide anion is involved in the induction of long-term potentiation in the rat somatosensory cortex in vitro. Brain Res. *1024*, 104–112.

59. Hinds, T.D., Jr, Hinds, T.D., Burns, K.A., Hosick, P.A., McBeth, L., Nestor-Kalinoski, A., Drummond, H.A., AlAmodi, A.A., Hankins, M.W., Vanden Heuvel, J.P., et al. (2016). Biliverdin reductase A attenuates hepatic steatosis by inhibition of glycogen synthase kinase (GSK) 3β phosphorylation of serine 73 of peroxisome proliferator-activated receptor (PPAR) α. J Biol Chem.

60. Hohenberg, P., and Kohn, W. (1964). Inhomogeneous Electron Gas. Physical Review B *136*, B864–.

61. Huie, R.E., and Padmaja, S. (1993). The reaction of no with superoxide. Free Radical Research *18*, 195–199.

62. Husen, P., and Solov'yov, I.A. (2016). Spontaneous Binding of Molecular Oxygen at the Qo-Site of the bc1 Complex Could Stimulate Superoxide Formation. J. Am. Chem. Soc. *138*, 12150–12158.

63. Ikoma, A., Steinhoff, M., Ständer, S., Yosipovitch, G., and Schmelz, M. (2006). The neurobiology of itch. Nat. Rev. Neurosci. *7*, 535–547.

64. Imamachi, N., Park, G.H., Lee, H., Anderson, D.J., Simon, M.I., Basbaum, A.I., and Han, S.-K. (2009). TRPV1-expressing primary afferents generate

behavioral responses to pruritogens via multiple mechanisms. Proc. Natl. Acad. Sci. U.S.a. *106*, 11330–11335.

65. IWANAGA, M., NAKAGAWARA, A., MATSUO, S., and IKEDA, K. (1987). Impaired Polymorphonuclear Leukocyte Function in Biliary Atresia - Role of Bilirubin and Bile-Acids. J. Pediatr. Surg. *22*, 967–972.

66. Jacobsen, J., and Broderson, R. (1983). Albumin-bilirubin binding mechanism. J Biol Chem *258*, 6319–6326.

67. Jansen, T., Hortmann, M., Oelze, M., Opitz, B., Steven, S., Schell, R., Knorr, M., Karbach, S., Schuhmacher, S., Wenzel, P., et al. (2010). Conversion of biliverdin to bilirubin by biliverdin reductase contributes to endothelial cell protection by heme oxygenase-1-evidence for direct and indirect antioxidant actions of bilirubin. J. Mol. Cell. Cardiol. *49*, 186–195.

68. Jenkins, P.M., Vasavda, C., Davis, J.Q., and Bennett, V. (2013). E-cadherin polarity is determined by a multifunction motif mediating lateral membrane retention through ankyrin-G and apical-lateral transcytosis through clathrin. J Biol Chem *288*, 14018–14031.

69. Jinek, M., Chylinski, K., Fonfara, I., Hauer, M., Doudna, J.A., and Charpentier, E. (2012). A Programmable Dual-RNA–Guided DNA Endonuclease in Adaptive Bacterial Immunity. Science *337*, 816–821.

70. Jones, C.M., Lawrence, A., and Wardman, P. (2002). Electron paramagnetic resonance spin trapping investigation into the kinetics of glutathione oxidation by the superoxide radical: re-evaluation of the rate …. Free Radical Biology and … *32*, 982–990.

71. Kaasik, K., and Lee, C.C. (2004). Reciprocal regulation of haem biosynthesis and the circadian clock in mammals. Nature *430*, 467.

72. Kajimura, M., Fukuda, R., Bateman, R.M., Yamamoto, T., and Suematsu, M. (2010). Interactions of Multiple Gas-Transducing Systems: Hallmarks and Uncertainties of CO, NO, and H 2S Gas Biology. Antioxid. Redox Signal. *13*, 157–192.

73. Kalir, T., Catanese, G.S., and Clejan, S. (1990). Clinical Diagnostic Utility of Delta Bilirubin. Lab Med *21*, 159–162.

74. Kellogg, E.W., and Fridovich, I. (1975). Superoxide, hydrogen peroxide, and singlet oxygen in lipid peroxidation by a xanthine oxidase system. J Biol Chem *250*, 8812–8817.

75. Kennelly, P.J., and Krebs, E.G. (1991). Consensus sequences as substrate specificity determinants for protein kinases and protein phosphatases. J Biol Chem.

76. Kikuchi, A., Park, S.-Y., Miyatake, H., Sun, D., Sato, M., Yoshida, T., and Shiro, Y. (2001). Crystal structure of rat biliverdin reductase. Nat. Struct Biol. *8*, 221–225.

77. Kim, Y.S., Chu, Y., Han, L., Li, M., Li, Z., LaVinka, P.C., Sun, S., Tang, Z., Park, K., Caterina, M.J., et al. (2014). Central Terminal Sensitization of TRPV1 by Descending Serotonergic Facilitation Modulates Chronic Pain. Neuron *81*, 873–887.

78. Klann, E. (1998). Cell-permeable scavengers of superoxide prevent long-term potentiation in hippocampal area CA1. J. Neurophysiol. *80*, 452–457.

79. Kobilka, B.K., Matsui, H., Kobilka, T.S., Yang-Feng, T.L., Francke, U., Caron, M.G., Lefkowitz, R.J., and Regan, J.W. (1987). Cloning, sequencing, and expression of the gene coding for the human platelet alpha 2-adrenergic receptor. Science *238*, 650–656.

80. Kobilka, B.K. (2007). G protein coupled receptor structure and activation. Biochim. Biophys. Acta *1768*, 794–807.

81. Kohn, W., and Sham, L.J. (1965). Self-Consistent Equations Including Exchange and Correlation Effects. Physical Review *140*, 1133–&.

82. Kontos, C.D., Wei, E.P., Williams, J.I., Kontos, H.A., and Povlishock, J.T. (1992). Cytochemical detection of superoxide in cerebral inflammation and ischemia in vivo. Am. J. Physiol. *263*, H1234–H1242.

83. Kozaki, N., Shimizu, S., Higashijima, H., Kuroki, S., Yamashita, H., Yamaguchi, K., Chijiiwa, K., and Tanaka, M. (1998). Significance of serum delta-bilirubin in patients with obstructive jaundice. J. Surg. Res. *79*, 61–65.

84. Kremer, A.E., Martens, J., Kulik, W., and Ruëff, F. (2010). Lysophosphatidic acid is a potential mediator of cholestatic pruritus. Gastroenterology.

85. Kremer, A.E., Elferink, R.P.J.O., and Beuers, U. (2011). Pathophysiology and current management of pruritus in liver disease. Clin Res Hepatol Gastroenterol *35*, 89–97.

86. Kumagai, A., Ando, R., Miyatake, H., Greimel, P., Kobayashi, T., Hirabayashi, Y., Shimogori, T., and Miyawaki, A. (2013). A bilirubin-inducible fluorescent protein from eel muscle. Cell *153*, 1602–1611.

87. Kumar, P., and Prabhakar, N.R. (2011). Peripheral Chemoreceptors: Function and Plasticity of the Carotid Body (Hoboken, NJ, USA: John Wiley & Sons, Inc.).

88. Kutty, R.K., and Maines, M.D. (1981). Purification and characterization of biliverdin reductase from rat liver. J. Biol. Chem. *256*, 3956–3962.

89. Kuzkaya, N., Weissmann, N., Harrison, D.G., and Dikalov, S. (2005). Interactions of peroxynitrite with uric acid in the presence of ascorbate and

thiols: implications for uncoupling endothelial nitric oxide synthase. Biochem. Pharmacol. *70*, 343–354.

90. Kwak, J.Y., Takeshige, K., Cheung, B.S., and Minakami, S. (1991). Bilirubin inhibits the activation of superoxide-producing NADPH oxidase in a neutrophil cell-free system. Biochim. Biophys. Acta *1076*, 369–373.

91. Lafon-Cazal, M., PIETRI, S., CULCASI, M., and BOCKAERT, J. (1993). NMDA-dependent superoxide production and neurotoxicity. Nature *364*, 535–537.

92. LaMotte, R.H., Dong, X., and Ringkamp, M. (2014). Sensory neurons and circuits mediating itch. Nature Publishing Group *15*, 19–31.

93. Laupacis, A., Keown, P.A., Ulan, R.A., Sinclair, N.R., and Stiller, C.R. (1981). Hyperbilirubinaemia and cyclosporin A levels. Lancet *2*, 1426–1427.

94. Lazareno, S., and Birdsall, N. (1993). Estimation of competitive antagonist affinity from functional inhibition curves using the Gaddum, Schild and Cheng-Prusoíf equations. Br J Pharmacol *109*, 1110–1119.

95. Lefkowitz, R.J. (2004). Historical review: a brief history and personal retrospective of seven-transmembrane receptors. Trends Pharmacol. Sci. *25*, 413–422.

96. Leftowitz, R.J., and Shenoy, S.K. (2005). Transduction of receptor signals by beta-arrestins. Science *308*, 512–517.

97. Legg, K.D., and Hercules, D.M. (1969). Electrochemically Generated Chemiluminescence of Lucigenin. J. Am. Chem. Soc. *91*, 1902–1907.

98. Lembo, P.M.C., Grazzini, E., Groblewski, T., O'Donnell, D., Roy, M.-O., Zhang, J., Hoffert, C., Cao, J., Schmidt, R., Pelletier, M., et al. (2002). Proenkephalin A gene products activate a new family of sensory neuron--specific GPCRs. Nat. Neurosci. *5*, 201–209.

99. Lerner-Marmarosh, N., Miralem, T., Gibbs, P.E.M., and Maines, M.D. (2008). Human biliverdin reductase is an ERK activator; hBVR is an ERK nuclear transporter and is required for MAPK signaling. Proc. Natl. Acad. Sci. U.S.a. *105*, 6870–6875.

100. Lerner-Marmarosh, N., Shen, J., Torno, M.D., Kravets, A., Hu, Z., and Maines, M.D. (2005). Human biliverdin reductase: a member of the insulin receptor substrate family with serine/threonine/tyrosine kinase activity. Proc. Natl. Acad. Sci. U.S.a. *102*, 7109–7114.

101. Levinson, S.S. (1997). Relationship between bilirubin, apolipoprotein B, and coronary artery disease. Ann. Clin. Lab. Sci. *27*, 185–192.

102. Levitt, D.G., and Levitt, M.D. (2014). Quantitative assessment of the multiple processes responsible for bilirubin homeostasis in health and disease. Clin Exp Gastroenterol *7*, 307–328.

103. Liu, Q., Sikand, P., Ma, C., Tang, Z., Han, L., Li, Z., Sun, S., LaMotte, R.H., and Dong, X. (2012). Mechanisms of itch evoked by β-alanine. Journal of Neuroscience *32*, 14532–14537.

104. Liu, Q., Tang, Z., Surdenikova, L., Kim, S., Patel, K.N., Ru, F., Kim, A., Weng, H.-J., Guan, Y., Geng, Y., et al. (2009). Sensory Neuron-Specific GPCR Mrgprs Are Itch Receptors Mediating Chloroquine-Induced Pruritus. Cell *139*, 1353–1365.

105. Liu, Q., Vrontou, S., Rice, F.L., Zylka, M.J., Dong, X., and Anderson, D.J. (2007). Molecular genetic visualization of a rare subset of unmyelinated sensory neurons that may detect gentle touch. Nat. Neurosci. *10*, 946–948.

106. Lohse, M., Benovic, J., Codina, J., Caron, M., and Lefkowitz, R. (1990). beta-Arrestin: a protein that regulates beta-adrenergic receptor function. Science *248*, 1547–1550.

107. LONDOS, C., SALOMON, Y., LIN, M.C., HARWOOD, J.P., SCHRAMM, M., WOLFF, J., and Rodbell, M. (1974). 5'-Guanylylimidodiphosphate, a Potent Activator of Adenylate Cyclase Systems in Eukaryotic Cells. Proc. Natl. Acad. Sci. U.S.a. *71*, 3087–3090.

108. Ma, D.K., Vozdek, R., Bhatla, N., and Horvitz, H.R. (2012). CYSL-1 interacts with the O2-sensing hydroxylase EGL-9 to promote H2S-modulated hypoxia-induced behavioral plasticity in C. elegans. Neuron *73*, 925–940.

109. Maghzal, G.J., Leck, M.-C., Collinson, E., Li, C., and Stocker, R. (2009). Limited role for the bilirubin-biliverdin redox amplification cycle in the cellular antioxidant protection by biliverdin reductase. J Biol Chem *284*, 29251–29259.

110. Maines, M.D. (2004). The heme oxygenase system: past, present, and future. Antioxid. Redox Signal.

111. Maines, M.D., Trakshel, G.M., and Kutty, R.K. (1986). Characterization of two constitutive forms of rat liver microsomal heme oxygenase. Only one molecular species of the enzyme is inducible. J Biol Chem *261*, 411–419.

112. Makarenko, V.V., Nanduri, J., Raghuraman, G., Fox, A.P., Gadalla, M.M., Kumar, G.K., Snyder, S.H., and Prabhakar, N.R. (2012). Endogenous H2S is required for hypoxic sensing by carotid body glomus cells. Am. J. Physiol., Cell Physiol. *303*, C916–C923.

113. Marcus, N.J., Del Rio, R., Schultz, E.P., Xia, X.-H., and Schultz, H.D. (2014). Carotid body denervation improves autonomic and cardiac function and attenuates disordered breathing in congestive heart failure. The Journal of Physiology *592*, 391–408.

114. MarÉchal, E. (2011). Measuring Bioactivity: KI, IC50 and EC50. In Chemogenomics and Chemical Genetics, (Berlin, Heidelberg: Springer Berlin Heidelberg), pp. 55–65.

115. MCCORD, J.M., and I, F. (1969). Superoxide Dismutase an Enzymic Function for Erythrocuprein (Hemocuprein). J Biol Chem *244*, 6049–&.

116. McCoubrey, W.K., Jr (1997). Heme Oxygenase-2 Is a Hemoprotein and Binds Heme through Heme Regulatory Motifs That Are Not Involved in Heme Catalysis. J. Biol. Chem. *272*, 12568–12574.

117. McDonagh, A.F. (2010). The biliverdin-bilirubin antioxidant cycle of cellular protection: Missing a wheel? Free Radic. Biol. Med. *49*, 814–820.

118. McNeil, B.D., Pundir, P., Meeker, S., Han, L., Undem, B.J., Kulka, M., and Dong, X. (2015). Identification of a mast-cell-specific receptor crucial for pseudo-allergic drug reactions. Nature *519*, 237–241.

119. Migita, C.T., Matera, K.M., Ikeda-Saito, M., Olson, J.S., Fujii, H., Yoshimura, T., Zhou, H., and Yoshida, T. (1998). The Oxygen and Carbon Monoxide Reactions of Heme Oxygenase. Journal of Biological ….

120. Milligan, G. (2003). Principles: extending the utility of [35S]GTP gamma S binding assays. Trends Pharmacol. Sci. *24*, 87–90.

121. Miwa, S., St-Pierre, J., Partridge, L., and Brand, M.D. (2003). Superoxide and hydrogen peroxide production by Drosophila mitochondria. Free Radic. Biol. Med. *35*, 938–948.

122. Moccia, M., Picillo, M., Erro, R., Longo, K., Amboni, M., Santangelo, G., Palladino, R., Allocca, R., Caporale, O., Triassi, M., et al. (2015). Increased bilirubin levels in de novo Parkinson's disease. Eur. J. Neurol. *22*, 954–959.

123. Moore, P.K., Wallace, P., Gaffen, Z., Hart, S.L., and Babbedge, R.C. (1993). Characterization of the novel nitric oxide synthase inhibitor 7-nitro indazole and related indazoles: antinociceptive and cardiovascular effects. Br J Pharmacol *110*, 219–224.

124. Morikawa, T., Kajimura, M., Nakamura, T., Hishiki, T., Nakanishi, T., Yukutake, Y., Nagahata, Y., Ishikawa, M., Hattori, K., Takenouchi, T., et al. (2012). Hypoxic regulation of the cerebral microcirculation is mediated by a carbon monoxide-sensitive hydrogen sulfide pathway. Proc. Natl. Acad. Sci. U.S.a. *109*, 1293–1298.

125. Motterlini, R. (2002). Carbon Monoxide-Releasing Molecules: Characterization of Biochemical and Vascular Activities. Circulation Research *90*, 17e–24.

126. Murphy, M.P. (2009). How mitochondria produce reactive oxygen species. Biochemical Journal.

127. Mustafa, A.K., Gadalla, M.M., and Snyder, S.H. (2009). Signaling by gasotransmitters. Sci Signal *2*, re2.

128. Nagy, P., Kettle, A.J., and Winterbourn, C.C. (2009). Superoxide-mediated Formation of Tyrosine Hydroperoxides and Methionine Sulfoxide in Peptides through Radical Addition and Intramolecular Oxygen Transfer. J Biol Chem *284*, 14723–14733.

129. NAKAMURA, H., UETANI, Y., KOMURA, M., TAKADA, S., SANO, K., and MATSUO, T. (1987). Inhibitory-Action of Bilirubin on Superoxide Production by Polymorphonuclear Leukocytes. Biol. Neonate *52*, 273–278.

130. Nanduri, J., Makarenko, V., Reddy, V.D., Yuan, G., Pawar, A., Wang, N., Khan, S.A., Zhang, X., Kinsman, B., Peng, Y.-J., et al. (2012). Epigenetic regulation of hypoxic sensing disrupts cardiorespiratory homeostasis. Proc. Natl. Acad. Sci. U.S.a. *109*, 2515–2520.

131. Neer, E.J. (1995). Heterotrimeric c proteins: organizers of transmembrane signals. Cell *80*, 249–257.

132. Neubig, R.R., and Siderovski, D.P. (2002). Regulators of G-protein signalling as new central nervous system drug targets. Nat Rev Drug Discov *1*, 187–197.

133. Nytofte, N.S., Serrano, M.A., Monte, M.J., Gonzalez-Sanchez, E., Tumer, Z., Ladefoged, K., Briz, O., and Marin, J.J.G. (2011). A homozygous nonsense mutation (c.214C→A) in the biliverdin reductase alpha gene (BLVRA) results in accumulation of biliverdin during episodes of cholestasis. J. Med. Genet. *48*, 219–225.

134. OBERG, K.E. (1961). The site of the action of rotenone in the respiratory chain. Exp. Cell Res. *24*, 163–164.

135. Olson, K.R., Donald, J.A., and Dombkowski, R.A. (2012). Evolutionary and comparative aspects of nitric oxide, carbon monoxide and hydrogen sulfide. Respiratory Physiology & ….

136. Olson, K.R., Healy, M.J., and Qin, Z. (2008a). Hydrogen sulfide as an oxygen sensor in trout gill chemoreceptors | Regulatory, Integrative and Comparative Physiology. American Journal of ….

137. Olson, K.R., Forgan, L.G., Dombkowski, R.A., and Forster, M.E. (2008b). Oxygen dependency of hydrogen sulfide-mediated vasoconstriction in cyclostome aortas. J. Exp. Biol. *211*, 2205–2213.

138. Ortega-Saenz, P. (2006). Acute Oxygen Sensing in Heme Oxygenase-2 Null Mice. The Journal of General Physiology *128*, 405–411.

139. Osborn, E.C., Wootton, I.D.P., Da Silva, L.C., and Sherlock, S. (1959). SERUM-BILE-ACID LEVELS IN LIVER DISEASE. The Lancet *274*, 1049–1053.

140. Ostrow, J.D., and Celic, L. (1984). Bilirubin chemistry, ionization and solubilization by bile salts. Hepatology *4*, 38S–45S.

141. Overington, J.P., Al-Lazikani, B., and Hopkins, A.L. (2006). How many drug targets are there? Nat Rev Drug Discov *5*, 993–996.

142. Park, J.-S., Nam, E., Lee, H.-K., Lim, M.H., and Rhee, H.-W. (2016). In Cellulo Mapping of Subcellular Localized Bilirubin. ACS Chem. Biol.

143. Paton, J.F.R., Sobotka, P.A., Fudim, M., Engelman, Z.J., Engleman, Z.J., Hart, E.C.J., McBryde, F.D., Abdala, A.P., Marina, N., Gourine, A.V., et al. (2013). The carotid body as a therapeutic target for the treatment of sympathetically mediated diseases. Hypertension *61*, 5–13.

144. Paul, B.D., and Snyder, S.H. (2012). S signalling through protein sulfhydration and beyond. Nat. Rev. Mol. Cell Biol. *13*, 449–507.

145. Paul, B.D., and Snyder, S.H. (2014). Modes of Physiologic H2S Signaling in the Brain and Peripheral Tissues. Antioxid. Redox Signal.

146. Paul, B.D., Sbodio, J.I., Xu, R., Vandiver, M.S., Cha, J.Y., Snowman, A.M., and Snyder, S.H. (2014). Cystathionine c-lyase deficiency mediates neurodegeneration in Huntington's disease. Nature 1–8.

147. Peng, Y.-J., Makarenko, V.V., Nanduri, J., Vasavda, C., Raghuraman, G., Yuan, G., Gadalla, M.M., Kumar, G.K., Snyder, S.H., and Prabhakar, N.R. (2014). Inherent variations in CO-H2S-mediated carotid body O2 sensing mediate hypertension and pulmonary edema. Proc. Natl. Acad. Sci. U.S.a. *111*, 1174–1179.

148. Peng, Y.-J., Nanduri, J., Raghuraman, G., Souvannakitti, D., Gadalla, M.M., Kumar, G.K., Snyder, S.H., and Prabhakar, N.R. (2010). H2S mediates

O2 sensing in the carotid body. Proc. Natl. Acad. Sci. U.S.a. *107*, 10719–10724.

149. Perlstein, T.S., Pande, R.L., Creager, M.A., Weuve, J., and Beckman, J.A. (2008). Serum total bilirubin level, prevalent stroke, and stroke outcomes: NHANES 1999-2004. Am. J. Med. *121*, 781–788.e781.

150. PETRONE, W.F., ENGLISH, D.K., WONG, K., and MCCORD, J.M. (1980). Free-Radicals and Inflammation - Superoxide-Dependent Activation of a Neutrophil Chemotactic Factor in Plasma. Proc. Natl. Acad. Sci. U.S.a. *77*, 1159–1163.

151. Prabhakar, N.R., Dinerman, J.L., Agani, F.H., and Snyder, S.H. (1995). Carbon monoxide: a role in carotid body chemoreception. Proc. Natl. Acad. Sci. U.S.a. *92*, 1994–1997.

152. Prabhakar, N.R., Kumar, G.K., Chang, C.H., Agani, F.H., and Haxhiu, M.A. (1993). Nitric oxide in the sensory function of the carotid body. Brain Res. *625*, 16–22.

153. Prabhakar, N.R. (2013). Sensing hypoxia: physiology, genetics and epigenetics. The Journal of Physiology no–no.

154. Prabhakar, N.R., and Semenza, G.L. (2012). Gaseous messengers in oxygen sensing. J. Mol. Med. *90*, 265–272.

155. Rege, R.V., Webster, C.C., and Ostrow, J.D. (1988). Interactions of unconjugated bilirubin with bile salts. J. Lipid Res. *29*, 1289–1296.

156. Reyes, R.C., Brennan, A.M., Shen, Y., Baldwin, Y., and Swanson, R.A. (2012). Activation of neuronal NMDA receptors induces superoxide-mediated oxidative stress in neighboring neurons and astrocytes. Journal of Neuroscience *32*, 12973–12978.

157. Roberson, D.P., Gudes, S., Sprague, J.M., Patoski, H.A.W., Robson, V.K., Blasl, F., Duan, B., Oh, S.B., Bean, B.P., Ma, Q., et al. (2013). Activity-dependent silencing reveals functionally distinct itch-generating sensory neurons. Nat. Neurosci. *16*, 910–918.

158. Rosenthal, I., and Bercovici, T. (1973). Chemiluminescenece of N-methylacridone induced by potassium superoxide. Journal of the Chemical Society, Chemical Communications 200–201.

159. Ross, E.M., and Gilman, A.G. (1977). Resolution of Some Components of Adenylate-Cyclase Necessary for Catalytic Activity. J Biol Chem *252*, 6966–6969.

160. Salah-Uddin, H., Thomas, D.R., Davies, C.H., Hagan, J.J., Wood, M.D., Watson, J.M., and Challiss, R.A.J. (2008). Pharmacological Assessment of M1 Muscarinic Acetylcholine Receptor-Gq/11 Protein Coupling in Membranes Prepared from Postmortem Human Brain Tissue. J. Pharmacol. Exp. Ther. *325*, 869–874.

161. Sawyer, D.T., and Valentine, J.S. (2002). How super is superoxide? Acc. Chem. Res. *14*, 393–400.

162. SCHWERTNER, H.A., JACKSON, W.G., and TOLAN, G. (1994). Association of Low Serum Concentration of Bilirubin with Increased Risk of Coronary-Artery Disease. Clin. Chem. *40*, 18–23.

163. Scigliano, G., Girotti, F., Soliveri, P., Musicco, M., Radice, D., and Caraceni, T. (1997). Increased plasma bilirubin in Parkinson patients on L-dopa: evidence against the free radical hypothesis? Ital J Neurol Sci *18*, 69–72.

164. Shibuta, S., Mashimo, T., Zhang, P., Ohara, A., and Yoshiya, I. (1996). A new nitric oxide donor, NOC-18, exhibits a nociceptive effect in the rat formalin model. Journal of the Neurological Sciences *141*, 1–5.

165. Shimada, S.G., and LaMotte, R.H. (2008). Behavioral differentiation between itch and pain in mouse. Pain *139*, 681–687.

166. Shintani, T., Iwabuchi, T., Soga, T., Kato, Y., Yamamoto, T., Takano, N., Hishiki, T., Ueno, Y., Ikeda, S., Sakuragawa, T., et al. (2009). Cystathionine beta-synthase as a carbon monoxide-sensitive regulator of bile excretion. Hepatology *49*, 141–150.

167. Sikand, P., Dong, X., and LaMotte, R.H. (2011). BAM8-22 peptide produces itch and nociceptive sensations in humans independent of histamine release. Journal of Neuroscience *31*, 7563–7567.

168. Sittampalam, G.S., Coussens, N.P., Nelson, H., Arkin, M., Auld, D., Austin, C., Bejcek, B., Glicksman, M., Inglese, J., Iversen, P.W., et al. (2004). GTPγS Binding Assays.

169. Solinski, H.J., Gudermann, T., and Breit, A. (2014). Pharmacology and signaling of MAS-related G protein-coupled receptors. Pharmacological Reviews *66*, 570–597.

170. STADEL, J.M., NAMBI, P., SHORR, R., SAWYER, D.F., Caron, M.G., and Lefkowitz, R.J. (1983). Catecholamine-Induced Desensitization of Turkey Erythrocyte Adenylate-Cyclase Is Associated with Phosphorylation of the Beta-Adrenergic-Receptor. Proc. Natl. Acad. Sci. U.S.a. *80*, 3173–3177.

171. Ständer, S., Weisshaar, E., Mettang, T., Szepietowski, J.C., Carstens, E., Ikoma, A., Bergasa, N.V., Gieler, U., Misery, L., Wallengren, J., et al. (2007). Clinical classification of itch: a position paper of the International Forum for the Study of Itch. Acta Derm. Venereol. *87*, 291–294.

172. Stec, D.E., Storm, M.V., Pruett, B.E., and Gousset, M.U. (2013). Antihypertensive actions of moderate hyperbilirubinemia: role of superoxide inhibition. Am. J. Hypertens. *26*, 918–923.

173. Stenkamp, R.E., Kumasaka, T., Palczewski, K., Hori, T., Behnke, C.A., Motoshima, H., Fox, B.A., Le Trong, I., Teller, D.C., Okada, T., et al. (2000). Crystal structure of rhodopsin: A G protein-coupled receptor. Science *289*, 739–745.

174. Stephens, P.J., Devlin, F.J., Chabalowski, C.F., and Frisch, M.J. (1994). Ab-Initio Calculation of Vibrational Absorption and Circular-Dichroism Spectra Using Density-Functional Force-Fields. J. Phys. Chem. *98*, 11623–11627.

175. Stocker, R., Yamamoto, Y., McDonagh, A., Glazer, A., and Ames, B. (1987). Bilirubin is an antioxidant of possible physiological importance. Science *235*, 1043.

176. Strange, P.G. (2010). Use of the GTPγS ([35S]GTPγS and Eu-GTPγS) binding assay for analysis of ligand potency and efficacy at G protein-coupled receptors. Br J Pharmacol *161*, 1238–1249.

177. Subbarao, K.V., Richardson, J.S., and Ang, L.C. (1990). Autopsy samples of Alzheimer's cortex show increased peroxidation in vitro. J Neurochem *55*, 342–345.

178. Talwalkar, J.A., Souto, E., Jorgensen, R.A., and Lindor, K.D. (2003). Natural history of pruritus in primary biliary cirrhosis. Clin. Gastroenterol. Hepatol. *1*, 297–302.

179. Tan, Z.Y., Lu, Y., Whiteis, C.A., Simms, A.E., Paton, J.F.R., Chapleau, M.W., and Abboud, F.M. (2010). Chemoreceptor Hypersensitivity, Sympathetic Excitation, and Overexpression of ASIC and TASK Channels Before the Onset of Hypertension in SHR. Circulation Research *106*, 536–545.

180. Taoka, S., and Banerjee, R. (2001). Characterization of NO binding to human cystathionine beta-synthase: possible implications of the effects of CO and NO binding to the human enzyme. Journal of Inorganic Biochemistry *87*, 245–251.

181. Taoka, S., West, M., and Banerjee, R. (1999). Characterization of the heme and pyridoxal phosphate cofactors of human cystathionine beta-synthase reveals nonequivalent active sites. Biochemistry *38*, 2738–2744.

182. TAPPEL, A.L. (1955). Unsaturated lipide oxidation catalyzed by hematin compounds. J Biol Chem *217*, 721–733.

183. Thornton, J.R., and Losowsky, M.S. (1989a). Methionine enkephalin is increased in plasma in acute liver disease and is present in bile and urine. J. Hepatol. *8*, 53–59.

184. Thornton, J.R., and Losowsky, M.S. (1989b). Plasma leucine enkephalin is increased in liver disease. Gut *30*, 1392–1395.

185. Traynor, J.R., and Nahorski, S.R. (1995). Modulation by mu-opioid agonists of guanosine-5'-O-(3-[35S]thio)triphosphate binding to membranes from human neuroblastoma SH-SY5Y cells. Mol. Pharmacol. *47*, 848–854.

186. Trzebski, A. (1992). Arterial chemoreceptor reflex and hypertension. Hypertension.

187. Van Der Veere, C.N., Sinaasappel, M., McDonagh, A.F., Rosenthal, P., Labrune, P., Odièvre, M., Fevery, J., Otte, J.B., Mcclean, P., Bürk, G., et al. (1996). Current therapy for Crigler-Najjar syndrome type 1: Report of a world registry. Hepatology *24*, 311–315.

188. Vandiver, M.S., Paul, B.D., Xu, R., Karuppagounder, S., Rao, F., Snowman, A.M., Ko, H.S., Lee, Y.I., Dawson, V.L., Dawson, T.M., et al. (2013). Sulfhydration mediates neuroprotective actions of parkin. Nat Commun *4*, 1626.

189. Vasavda, C., Zaccor, N.W., Scherer, P.C., Sumner, C.J., and Snyder, S.H. (2017). Measuring G-protein-coupled Receptor Signaling via Radio-labeled GTP Binding. J Vis Exp.

190. Vera, T., Granger, J.P., and Stec, D.E. (2009). Inhibition of bilirubin metabolism induces moderate hyperbilirubinemia and attenuates ANG II-dependent hypertension in mice. Am. J. Physiol. Regul. Integr. Comp. Physiol. *297*, R738–R743.

191. Verma, A., Hirsch, D.J., Glatt, C.E., Ronnett, G.V., and Snyder, S.H. (1993). Carbon monoxide: a putative neural messenger. Science *259*, 381–384.

192. Vitek, L., Jirsa, M., Brodanova, M., Kalab, M., Marecek, Z., Danzig, V., Novotny, L., and Kotal, P. (2002). Gilbert syndrome and ischemic heart disease: a protective effect of elevated bilirubin levels. Atherosclerosis *160*, 449–456.

193. Voet, D., Voet, J.G., and Pratt, C.W. (2016). Fundamentals of Biochemistry: Life at the Molecular Level, 5th Edition (Wiley Global Education).

194. Wang, T., and Kass, I.S. (1997). Preparation of brain slices. Methods Mol. Biol. *72*, 1–14.

195. Wang, X.T., Culotta, V.C., and Klee, C.B. (1996). Superoxide dismutase protects calcineurin from inactivation. Nature *383*, 434–437.

196. Wegiel, B., Baty, C.J., Gallo, D., Csizmadia, E., Scott, J.R., Akhavan, A., Chin, B.Y., Kaczmarek, E., Alam, J., Bach, F.H., et al. (2009). Cell surface biliverdin reductase mediates biliverdin-induced anti-inflammatory effects via phosphatidylinositol 3-kinase and Akt. J Biol Chem *284*, 21369–21378.

197. Weyemi, U., Redon, C.E., Aziz, T., Choudhuri, R., Maeda, D., Parekh, P.R., Bonner, M.Y., Arbiser, J.L., and Bonner, W.M. (2015). Inactivation of NADPH oxidases NOX4 and NOX5 protects human primary fibroblasts from ionizing radiation-induced DNA damage. Radiat. Res. *183*, 262–270.

198. WILDEN, U., and KUHN, H. (1982). Light-Dependent Phosphorylation of Rhodopsin - Number of Phosphorylation Sites. Biochemistry *21*, 3014–3022.

199. Williams, S.E.J. (2004). Hemoxygenase-2 Is an Oxygen Sensor for a Calcium-Sensitive Potassium Channel. Science *306*, 2093–2097.

200. Winterbourn, C.C., and Metodiewa, D. (1999). Reactivity of biologically important thiol compounds with superoxide and hydrogen peroxide. Free Radic. Biol. Med. *27*, 322–328.

201. Winterbourn, C.C., Parsons-Mair, H.N., Gebicki, S., Gebicki, J.M., and Davies, M.J. (2004). Requirements for superoxide-dependent tyrosine hydroperoxide formation in peptides. Biochemical Journal *381*, 241–248.

202. Yamamoto, Y., Yamazaki, S., Hayashino, Y., Takahashi, O., Tokuda, Y., Shimbo, T., Fukui, T., Hinohara, S., Miyachi, Y., and Fukuhara, S. (2009). Association between frequency of pruritic symptoms and perceived psychological stress: a Japanese population-based study. Arch Dermatol *145*, 1384–1388.

203. Yang, G., Wu, L., Jiang, B., Yang, W., Qi, J., Cao, K., Meng, Q., Mustafa, A.K., Mu, W., Zhang, S., et al. (2008). H2S as a Physiologic Vasorelaxant: Hypertension in Mice with Deletion of Cystathionine -Lyase. Science *322*, 587–590.

204. Yosipovitch, G., Goon, A., Wee, J., Chan, Y.H., and Goh, C.L. (2000). The prevalence and clinical characteristics of pruritus among patients with extensive psoriasis. Br. J. Dermatol. *143*, 969–973.

205. Yosipovitch, G., and Bernhard, J.D. (2013). Clinical practice. Chronic pruritus. N. Engl. J. Med. *368*, 1625–1634.

206. Yuan, G., Peng, Y.-J., Reddy, V.D., Makarenko, V.V., Nanduri, J., Khan, S.A., Garcia, J.A., Kumar, G.K., Semenza, G.L., and Prabhakar, N.R. (2013). Mutual antagonism between hypoxia-inducible factors 1α and 2α regulates oxygen sensing and cardio-respiratory homeostasis. Proc. Natl. Acad. Sci. U.S.a. *110*, E1788–E1796.

207. Yung-Chi, C., and Prusoff, W.H. (1973). Relationship between the inhibition constant (K i) and the concentration of inhibitor which causes 50 per cent inhibition (I 50) of an enzymatic reaction. Biochem. Pharmacol. *22*, 3099–3108.

208. Zakhary, R., Gaine, S.P., Dinerman, J.L., Ruat, M., Flavahan, N.A., and Snyder, S.H. (1996). Heme oxygenase 2: endothelial and neuronal localization and role in endothelium-dependent relaxation. Proc. Natl. Acad. Sci. U.S.a. *93*, 795–798.

209. Zhang, L., Taylor, N., Xie, Y., Ford, R., Johnson, J., Paulsen, J.E., and Bates, B. (2005). Cloning and expression of MRG receptors in macaque, mouse, and human. Brain Res. Mol. Brain Res. *133*, 187–197.

210. Zhao, H.T., Joseph, J., Fales, H.M., Sokoloski, E.A., Levine, R.L., Vasquez-Vivar, J., and Kalyanaraman, B. (2005). Detection and characterization of the product of hydroethidine and intracellular superoxide by HPLC and limitations of fluorescence. Proc. Natl. Acad. Sci. U.S.a. *102*, 5727–5732.

211. Zhao, H.T., Kalivendi, S., Zhang, H., Joseph, J., Nithipatikom, K., Vasquez-Vivar, J., and Kalyanaraman, B. (2003). Superoxide reacts with hydroethidine but forms a fluorescent product that is distinctly different from ethidium: Potential implications in intracellular fluorescence detection of superoxide. Free Radic. Biol. Med. *34*, 1359–1368.

212. Zielonka, J., Vásquez-Vivar, J., and Kalyanaraman, B. (2006). The confounding effects of light, sonication, and Mn(III)TBAP on quantitation of superoxide using hydroethidine. Free Radic. Biol. Med. *41*, 1050–1057.

213. Zylka, M.J., Dong, X., Southwell, A.L., and Anderson, D.J. (2003). Atypical expansion in mice of the sensory neuron-specific Mrg G protein-coupled receptor family. Proc. Natl. Acad. Sci. U.S.a. *100*, 10043–10048.

Curriculum vitae

CHIRAG S. VASAVDA July 2019

Education & Training

2014-present	M.D./Ph.D candidate Johns Hopkins University School of Medicine Baltimore, MD Mentor: Solomon Snyder, M.D.
2009-2013	B.S. in Chemistry and Biology, minor in Chinese Duke University Durham, NC Conferred May 2013

Research Experience

08/2014-present	Laboratory of Solomon Snyder, M.D. The Solomon H. Snyder Department of Neuroscience Johns Hopkins University Baltimore, MD
08/2013-08/2014	Laboratory of Nanduri Prabhakar, D.Sc., Ph.D. Department of Emergency Medicine University of Chicago Chicago, IL
10/2010-05/2013	Laboratory of Vann Bennett, M.D., Ph.D. Department of Biochemistry Duke University and Howard Hughes Medical Institute Durham, NC

Grant & Fellowship Awards

Current funding

2019	Sponsor: GENEWIZ, Inc Title: Oxidative stress contributes to trigeminal neuralgia Support: GENEWIZ Genomics Prize Runner-Up Total Direct Costs: $1,000
2018	Sponsor: Neurosurgery Pain Research Institute (Johns Hopkins Medicine) Title: Reactive oxygen species activate TRPA1 to trigger trigeminal neuralgia Support: Research Fellow Support Period: 08/2018-08/2019

Total Direct Costs: $60,000

Previously Funded

2012 Sponsor: Trinity College Biology Research Fellowship (Duke University)
Title: Role of giant ankyrin-G in organizing the axon initial segment
Support: Trinity College Research Fellow
Support Period: 08/2012-12/2012
Total Direct Costs: $400

2012 Sponsor: Dean's Summer Research Fellowship (Duke University)
Title: Mechanisms of neuronal axo-dendritic polarity
Support: Undergraduate Research Fellow
Support Period: 05/2012-8/2012
Total Direct Costs: $3,500

2011 Sponsor: Dean's Summer Research Fellowship (Duke University)
Title: Mechanisms of ciliary biogenesis and polarity
Support: Undergraduate Research Fellow
Support Period: 05/2011-8/2011
Total Direct Costs: $3,500

Patents

1. PCT/US18/37870: Compositions and methods for treating G-protein coupled receptor mediated conditions. Dong X, **Vasavda C**, Snyder SH, Meixiong J, Cheng Y, Limjunyawong N, Dong X. *Patent application filed.*

Honors & Awards

September 2012	Trinity College Biology Research Fellowship
Spring 2011-Fall 2013	Dean's List

Scientific & Leadership Service

Welch Library Advisory Council, Johns Hopkins University
Student Advisor 2018-present

Proceedings of the National Academy of Science
Journal Club Panel Member 2018-present

Journal of Young Investigators
Peer Reviewer 2012-2014

Teaching & Mentoring

Lectures and Courses

05/2012-08/2012 Instructor
Zhuhai No.9 Middle School

Zhuhai, Guangdong, China
Intermediate English

05/2012-08/2012 Instructor
Zhuhai No.9 Middle School
Zhuhai, Guangdong, China
Beginner Hip Hop

01/2012-05/2012 Teaching Assistant
Department of Chemistry, Duke University
Durham, NC, USA
Chemistry 101L9: Core Concepts in Chemistry Lab

08/2011-12/2011 Head Teaching Assistant
Department of Chemistry, Duke University
Durham, NC, USA
Chemistry 110DL: Honors Chemistry

Trainees

10/2015-05/2019 Ruchita Kothari (Johns Hopkins University)
10/2015-05/2019 Cristina Ricco (Johns Hopkins University)
12/201205/2013 David Shou, Uniformed Services University of the Health Sciences (Duke University)

Other activities

09/2014-05/2016 Dancer, SLAM Hip Hop Dance Team
09/2009-05/2013 Dancer, Defining Movement Dance Team

Languages & skills

LANGUAGES:
French, Gujarati (conversational fluency); Chinese, Hindi (intermediate)
PROGRAMMING:
MATLAB (intermediate), LaTeX (intermediate)

Bibliography

Peer-Reviewed Publications

1. **Vasavda C**, Kothari R, Malla AP*, Tokhunts R*, Lin A, Ji M, Ricco C, Xu R, Saavedra H, Sbodio JI, Snowman AM, Albacarys L, Hester L, Sedlak TW, Paul PD, and Snyder SH. Bilirubin links heme metabolism to neuroprotection by scavenging superoxide. *Cell Chem. Biol. in press. (*contributed equally to this work)*

2. Pundir P, Liu R, Zhan Y, **Vasavda C**, Serhan N, Yee R, Limjunyawong N, Dong X, Chen M, Wu X, Lane A, Zhang Y, Gaudenzio N, Snyder SH, He L, Vidal JE, Dong X. (2019) Identification of Mammalian Receptors for Quorum Sensing Molecules and Their Role in Antibacterial Immunity. *Cell Host Microbe. in press*.

3. Meixiong J, **Vasavda C**, Snyder SH, Dong X. (2019) MRGPRX4 is a G-protein coupled receptor activated by bile acids that may contribute to cholestatic pruritus. *Proc. Natl. Acad. Sci. in press*.

4. Patel S, **Vasavda C**, Ho B, Meixiong J, Dong X, Kwatra S. (2019) Cholestatic pruritus: emerging mechanisms and therapeutics. *J. Am. Acad. Dermatol. in press*.

5. Meixiong J*, **Vasavda C***, Green D, Zheng Q, Qi L, Kwatra SG, Hamilton JP, Snyder SH, Dong X. (2019) Identification of a bilirubin receptor that may mediate a component of cholestatic itch. *eLIFE. 2019;8:e44116*.
*(*contributed equally to this work)*

6. Scherer PC*, Zaccor NW*, Neumann NM, **Vasavda C**, Barrow R, Ewald AJ, Rao F, Sumner CJ, Snyder SH. (2017) TRPV1 is a physiologic regulator of μ-opioid receptors. *Proc. Natl. Acad. Sci.* 114 (51), 13561-13566. *(*contributed equally to this work)*

7. **Vasavda C***, Zaccor NW*, Scherer PC, Sumner CJ, Snyder SH. (2017) Measuring G-protein coupled receptor signaling via radiolabeled GTP binding. *J. Vis. Exp.* 9 (124). *(*contributed equally to this work)*

8. Peng Y-J, Zhang X, Gridina A, Chupikova I, McCormick DL, Thomas RJ, Scammell TE, Kim G, **Vasavda C**, Nanduri J, Kumar GK, Semenza GL, Snyder SH, Prabhakar NR. (2016) Gasotransmitters in Sleep Apnea: Complementary Roles of CO and H_2S. *Proc. Natl. Acad. Sci.* 114 (6), 1413-1418.

9. Yuan G, Peng Y-J, Khan SA, Nanduri J, Singh A, **Vasavda C**, Semenza GL, Kumar GK, Snyder SH, Prabhakar NR. (2016) H_2S Production by Reactive Oxygen Species in the Carotid Body Triggers Hypertension in a Rodent Model of Sleep Apnea. *Sci. Signal.* 9 (441), ra80-80.

10. Yuan G*, **Vasavda C***, Peng Y-J*, Makarenko VV, Raghuraman G, Nanduri J, Gadalla MM, Semenza GL, Kumar GK, Snyder SH, Prabhakar NR. (2015) Protein Kinase G-Regulated Production of H_2S Governs Oxygen Sensing. *Sci. Signal.* 8 (373), ra37. *(*contributed equally to this work)*

11. Peng Y-J, Yuan G, Khan S, Nanduri J, Makarenko VV, Reddy VD, **Vasavda C**, Kumar GK, Semenza GL, Prabhakar NR. (2014) Regulation of Hypoxia Inducible Factor-α Isoforms and Redox State By Carotid Body Neural Activity in Rats. *J. Phys.* 592, 3841–3858.

12. Peng Y-J, Makarenko VV, Nanduri J, **Vasavda C**, Raghuraman G, Yuan G, Gadalla MM, Kumar GK, Snyder SH, Prabhakar NR. (2014) Inherent Variations in CO-H_2S Mediated Carotid Body O_2 Sensing Mediate Hypertension and Pulmonary Edema. *Proc. Natl. Acad. Sci.* 111 (3), 1174-1179.

13. Jenkins P, **Vasavda C**, Hostettler J, Davis JQ, Abdi, K, Bennett V. (2013) E-cadherin Polarity is Determined by a Multi-function Motif Mediating Lateral Membrane Retention Through Ankyrin-G and Apical-lateral Transcytosis Through Clathrin. *J. Biol. Chem.* 288, 14018-14031.

Abstracts

1. **Vasavda C**, Kwatra MM, Kwatra SG. Phospho-Proteomic Profiling Reveals Distinct Signaling Pathways By First and Third Generation EGFR Inhibitors In Human Keratinocytes: Implications For Adverse Dermatologic Reactions. *International Investigative Dermatology Annual Meeting.* May 2018, Orlando, FL.

2. Kumar GK, Yuan G, Peng Y-J, Makarenko VV, Raghuraman G, Nanduri J, **Vasavda C**, Gadalla MM, Snyder SH, Prabhakar NR. Protein Kinase G Regulated H_2S Governs O_2 Sensing by the Carotid Body. *Federation of American Societies for Experimental Biology Annual Meeting.* April 2015, Boston, MA.

3. Peng Y-J, Makarenko VV, Nanduri J, **Vasavda C**, Raghuraman G, Yuan G, Gadalla MM, Kumar GK, Snyder SH, Prabhakar NR. Strain-Dependent Variations in Carotid Body O_2 Sensing: Role of CO-H_2S Signaling. *Federation of American Societies for Experimental Biology Annual Meeting.* April 2015, Boston, MA.

4. Jenkins PM, Nilsson KR, **Vasavda C**, Davis JQ, Abdi K, Bennett V. Micropatterning of Plasma Membranes of Differentiated Vertebrate Cells. *American Society for Cell Biology Annual Meeting.* December 2012, San Francisco, CA.

5. Jenkins PM, Nilsson KR, **Vasavda C**, Davis JQ, Bennett V. Ankyrin-G Mediates a Conserved yet Versatile Pathway for Assembly of Specialized Membrane Domains in Epithelial Cells and Neurons. *American Society for Cell Biology Annual Meeting.* December 2011, Denver, CO.

Presentations

1. **Vasavda C**, Tokhunts T, Sbodio JI, Sedlak TW, Snowman AM, Paul BD, Snyder SH. Neuroprotective roles of Biliverdin Reductase in the Brain. *9th International Conference on Heme Oxygenase.* September 2016, Prague, Czech Republic.